

# The Calculation of Flow and Heat Transfer Over Surface Mounted Ribs using a Domain Decomposition Method

by

Trevor George Zapach  
B.Sc., University of Alberta, 1991

ACCEPTED


FACULTY OF GRADUATE STUDIES


A Thesis Submitted in Partial Fulfillment of the  
Requirements for the Degree of


MASTERS OF APPLIED SCIENCE


in the Department of Mechanical Engineering

We accept this thesis as conforming  
to the required standard

  
\_\_\_\_\_  
Dr. N. Dijlali, Supervisor (Dept. of Mechanical Engineering)

  
\_\_\_\_\_  
Dr. S. Dost, Departmental Member (Dept. of Mechanical Engineering)

  
\_\_\_\_\_  
Dr. R. Lueck, Outside Member (School of Earth and Ocean Sciences)

  
\_\_\_\_\_  
Dr. D.D. Olesky, External Examiner (Dept. of Computer Science)

© TREVOR GEORGE ZAPACH, 1993  
University of Victoria

All rights reserved. Thesis may not be reproduced in whole or part, by photocopy or other  
means, without the permission of the author.

Supervisor: Dr. Ned Djilali

## **Abstract**

A numerical study of the accuracy and simulated parallel efficiency of domain decomposition applied to a finite volume fluid flow solver is presented. Two test cases were studied, developing flow in a channel and flow over a surface mounted rib, each with several subdomain configurations. Three methods to improve accuracy and convergence rates were investigated. An over relaxation scheme was applied at the subdomain interfaces, a subdomain continuity modification was implemented, and the subdomain calculation sequence was modified. All three methods improved the convergence rate. The subdomain continuity modification was necessary for high aspect ratio subdomain configurations to converge. It was found that solutions calculated with low aspect ratio subdomains produced dimensionless velocity differences from identical single domain solutions on the order of  $10^{-4}$ . Parallel efficiencies ranged from 46% to 154%, with efficiency dropping as more domains are added.

The domain decomposition method was applied to simulate forced convection cooling of an electronic device. The device was modeled as a rib mounted in a channel. Reynold's number, channel blockage ratio and Prandtl number are varied. Thermal conductivities are varied over a range covering most of the commonly use encapsulents. Conjugate heat transfer is used to model the thermal field produced from the heat generating rib. The flowfield produced at a blockage ratio of 0.50 and a Reynold's number of 150 produced two secondary recirculation zones, one on top of the rib and the other on the upper wall after the rib. The other flowfields only produced recirculation zones in front and behind the rib. The maximum temperature, which is the parameter of interest in design applications, was found to be weakly linked to Reynold's number, blockage ratio and

Prandtl number, but for dimensionless thermal conductivity less than 50 the maximum rib temperature is strongly dependent on thermal conductivity. For dimensionless thermal conductivities in excess of approximately 100, this dependency becomes weak.

**Examiners:**

---

Dr. N. Djilali, Supervisor (Dept. of Mechanical Engineering)



---

Dr. S. Dost, Departmental Member (Dept. of Mechanical Engineering)



---

Dr. R. Lueck, Outside Member (School of Earth and Ocean Sciences)



---

Dr. D.D. Olesky, External Examiner (Dept. of Computer Science)

## Contents

Abstract.....	ii
Table of Contents .....	iv
List of Figures .....	vii
List of Tables.....	xi
Nomenclature .....	xii
Acknowledgments .....	xvi
Dedication .....	xvii
<b>Chapter 1: Introduction</b> .....	<b>1</b>
1.0 Purpose and Scope.....	1
1.1 Description of Flowfields .....	3
1.1.1 Parallel Plates .....	3
1.1.2 Surface Mounted Ribs .....	4
1.2 Literature Review.....	5
1.2.1 Domain Decomposition .....	5
1.2.2 Parallel Plates .....	8
1.2.3 Low Blockage Ratio Rib.....	9
1.2.4 High Blockage Ratio Rib .....	11
1.3 Outline of Thesis .....	13
<b>Chapter 2: Computational Method</b> .....	<b>15</b>
2.0 Background .....	15
2.1 Finite Volume Formulation.....	17
2.1.1 Computational Cells .....	20
2.1.2 Solution Procedure .....	22
2.2 Application .....	23
2.2.1 Flow Boundary Conditions .....	23
2.2.2 Thermal Boundary Conditions .....	29
2.2.3 Grid Generation.....	31
2.2.4 Convergence Criterion.....	32

<b>Chapter 3: Domain Decomposition</b>	<b>33</b>
3.0 Background .....	33
3.1 Computational Method.....	36
3.2 Optimization of Relaxation Factors .....	40
3.3 Parallel Processing .....	41
3.4 Testing Accuracy .....	44
3.5 Memory Requirements .....	44
<b>Chapter 4: Numerical Verification</b>	<b>48</b>
4.0 Procedure .....	48
4.1 Developing Flow Between Parallel Plates .....	48
4.1.1 Grid Refinement Study .....	49
4.1.2 Flow Features .....	51
4.1.3 Domain Decomposition .....	53
4.1.4 Domain Decomposition Evaluation.....	63
4.2 Low Blockage Ratio Surface Mounted Rib.....	65
4.2.1 Grid Refinement Study .....	65
4.2.2 Flow Features .....	69
4.2.3 Domain Decomposition .....	74
4.2.4 Domain Decomposition Evaluation.....	79
<b>Chapter 5: High Blockage Ratio Rib Analysis</b>	<b>82</b>
5.0 Background .....	82
5.1 High Blockage Ratio Rib.....	82
5.2 Grid Refinement Study .....	84
5.3 Domain Decomposition.....	85
5.4 Flow Features .....	86
5.5 Thermal Features .....	91
<b>Chapter 6: Conclusions</b>	<b>98</b>
6.1 Domain Decomposition Findings.....	98
6.2 High Blockage Ratio Rib Findings.....	99
6.3 Areas of Future Study .....	100
<b>References</b>	<b>102</b>

**Appendices****105**

A	Source Term Modifications .....	105
B	Example of Spread Sheet Grid Generation.....	106
C	Program Variable Descriptions and Sizes.....	108
D	Fully Developed Parabolic Profile.....	112

## List of Figures

1.1	Schematic of parallel plate flowfield .....	3
1.2	Common recirculation configuration associated with flow over a surface mounted rib.....	4
2.1	Finite volume cell at node P with cell face fluxes and dimensions indicated. ....	19
2.2	Backward staggered grid showing the location of u and v-velocity cells relative to the pressure cell .....	21
2.3	North wall solid boundary treatment.....	24
2.4	South wall solid boundary treatment.....	25
2.5	Facing wall solid boundary treatment.....	25
2.6	Trailing wall solid boundary treatment.....	26
2.7	South symmetry boundary treatment .....	26
2.8	Leading corner boundary treatment .....	28
2.9	Trailing corner boundary treatment.....	29
3.1	Examples of a structured non-uniform grid and local refinement implemented with domain decomposition .....	34
3.2	Double elbow domain gridded with a single domain and with three domains .....	35
3.3	Flowchart of TEACH code with domain decomposition .....	37
3.4	Location of overlapping grids at a horizontal interface.....	39

3.5	Example Gantt charts for a parallel computer, a serial computer and a parallel simulation .....	42
3.6	Contour plot of memory usage with a DD implementation of a 80x50 node domain .....	47
4.1	Schematic of flow domain .....	49
4.2	Flow development process showing boundary layer core interaction .....	51
4.3	Velocity overshoot predicted in the development region of parallel plate flow .....	53
4.4	Domain layout for vertical interface of parallel plate case.....	53
4.5	Wall shear stress for three parallel plate test cases .....	54
4.6	U-velocity non-dimensional difference contours for the vertical interface parallel plate test case. Velocity made dimensionless with $\Delta U = \frac{U_{DD} - U_{\text{Benchmark}}}{U_{\infty}}$ .....	56
4.7	V-velocity non-dimensional difference contours for the vertical interface parallel plate test case. Velocity made dimensionless with $\Delta V = \frac{V_{DD} - V_{\text{Benchmark}}}{U_{\infty}}$ .....	57
4.8	Non-dimensional pressure difference contours for the vertical interface parallel plate test case. Pressure made dimensionless with $\Delta P = \frac{P_{DD} - P_{\text{Benchmark}}}{\frac{1}{2}\rho U_{\infty}^2}$ .....	58
4.9	Subdomain layout for horizontal interface of parallel plate case .....	59
4.10	U-velocity non-dimensional difference contours for the horizontal interface parallel plate test case. Velocity made dimensionless with $\Delta U = \frac{U_{DD} - U_{\text{Benchmark}}}{U_{\infty}}$ .....	60

4.11	V-velocity non-dimensional difference contours for the horizontal interface parallel plate test case. Velocity made dimensionless with	
	$\Delta V = \frac{V_{DD} - V_{\text{Benchmark}}}{U_{\infty}}$	61
4.12	Non-dimensional pressure difference contours for the vertical interface parallel plate test case. Pressure made dimensionless with	
	$\Delta P = \frac{P_{DD} - P_{\text{Benchmark}}}{\frac{1}{2} \rho U_{\infty}^2}$	62
4.13	Schematic of surface mounted rib domain.....	65
4.14	Wall shear stress in upstream recirculation region of rib flow. Origin of dimensionless wall coordinates is located at the downstream bottom corner of the rib. ....	66
4.15	Wall shear stress at trailing upper rib corner .....	67
4.16	Refined grid used for rib flows with a magnified insert of grid near the rib .....	68
4.17	Common recirculation zone configurations for surface mounted rib flows.....	70
4.18	Plot of South wall shear stress across entire domain .....	71
4.19	Lower leading edge rib corner wall shear stress .....	72
4.20	Wall shear stress over rib surface.....	72
4.21	Plot of velocity and streamlines for flow over a rib with an insert of flow near the rib.....	73
4.22	Subdomain layout for three domain surface mounted rib.....	74
4.23	Contour plots of velocity and pressure difference for the three domain rib test case. Dashed lines correspond to domain interfaces. Values made dimensionless with functions mentioned preciously .....	75
4.24	Domain layout for four domain rib case.....	76
4.25	Contour plots of velocity and pressure difference for the four domain rib test case. Dashed lines correspond to domain interfaces.....	78

5.1	Schematic of flow domain with a blockage ratio of 0.50 .....	83
5.2	Size and location of heat producing strip in surface mounted rib .....	83
5.3	Domain layout for four domain surface mounted rib .....	85
5.4	Velocity vector and streamline plots of flowfields produced with a blockage ratio of 0.25 and Reynold's numbers of 50, 100 and 150.....	87
5.5	Location and size of separation zones around low blockage ratio and high blockage ratio, BR = 0.25, ribs for a Reynold's number of 100.....	88
5.6	Close-up of secondary flow separation zones produced for a Re = 150 and a blockage ratio of 0.50.....	90
5.7	Plot of reattachment length for the nine flowfields .....	91
5.8	Plot of thermal field produced from a heated rib with BR=0.50, Re=100, and Pr=0.7 .....	94
5.9	Local Nusselt number along rib surface for three blockage ratios at a Reynold's number of 100 .....	95
5.10	Plot of maximum temperature for various thermal conductivities .....	97

## List of Tables

2.1	Generalized transport equation coefficients and source terms.....	17
3.1	Spread sheet memory model of 80x50 node domain .....	46
4.1	Grid refinement study results .....	50
4.2	Optimum relaxation factors and convergence times for parallel plate test cases .....	55
4.3	Optimum relaxation factors and convergence times for rib test cases .....	77
4.4	Shape of stored cells, number of stored cells and number of calculated cells for each test case.....	81
5.1	Thermal conductivity of encapsulents .....	95

## Nomenclature

AR	Aspect ratio $\left( = \frac{\text{Height}}{\text{Length}} \right)$
BR	Blockage Ratio $\left( = \frac{\text{Rib Height}}{\text{Channel Height}} \right)$
$C_f$	Wall shear stress coefficient $\left( = \frac{\tau_{\text{wall}}}{\frac{1}{2}\rho U_{\infty}^2} \right)$
$c_p$	Specific heat
$\frac{D}{Dt}$	Material derivative
$E_x, E_y$	Grid expansion factors $\left( = \frac{\Delta x_{i+1}}{\Delta x_i}, = \frac{\Delta y_{j+1}}{\Delta y_j} \right)$
$g$	Gravity vector
$h$	Length scale, channel width or rib height
$k$	Thermal conductivity
$k'$	Dimensionless thermal conductivity $\left( = \frac{k_{\text{solid}}}{k_{\text{fluid}}} \right)$
$n_d$	Number of parallel processors
Nu	Nusselt number $\left( = \frac{\frac{\partial T}{\partial y} _{\text{wall}} \cdot h}{T_w - T_{\infty}} \right)$
$P, p$	Pressure

P, N, S, E, W	Grid points
Pr	Prandtl number $\left( = \frac{\mu \cdot c_p}{k} \right)$
Q	Cell face flux
$Q_{rib}$	Total heat produced inside rib
Re, $Re_h$	Reynold's number $\left( = \frac{U_\infty h}{\nu} \right)$
$S_\phi$	Generalized source term
S	Linearized source term
t	Time
T	Temperature
U, u	X-component direction velocity
V, v	Y-component direction velocity
$\vec{V}$	Velocity vector
x, y	Cartesian coordinates
$X_L$	Entrance length
$X_r$	Reattachment length
$\Delta x, \Delta y$	Scalar cell dimensions
$\delta x, \delta y$	Grid spacing
$\delta_{ij}$	Kronecker delta
$\delta$	Boundary layer thickness
$\epsilon_{su}$	Simulated parallel speed-up
$\epsilon_e$	Simulated parallel efficiency

$\Gamma$	Generalized diffusivity coefficient
$\phi$	Transport quantity
$\lambda$	Second viscosity coefficient
$\nu$	Kinematic viscosity
$\mu$	Viscosity
$\theta$	Dimensionless temperature $\left( = \frac{T - T_{\infty}}{Q_{rib} \cdot h / k_{fluid}} \right)$
$\rho$	Density
$\tau$	Shear stress

### Sub/Superscripts

n, s, e, w	Direction and cell wall indication
wall	Calculated at a wall
$\infty$	Free stream quantity or entrance quantity
*	Guessed or initial values
i,j	Tensor indices; grid points
' , "	Marked velocity components
max	Maximum value
c	Constant value
p	Proportional value

### Abbreviations

DD	Domain Decomposition
----	----------------------

FV	Finite Volume
FEA	Finite Element Analysis
CFD	Computational Fluid Dynamics
SAM	Schwarz Alternating Method

## **Acknowledgments**

I wish to thank Dr. Ned Djilali for his guidance over the past two years. I appreciate his careful and thorough approach to the study of fluid dynamic and I have learned a great deal under his guidance.

I wish to express my gratitude to my family, who have encouraged and supported me throughout my studies. I also thank my friends who have made the last two years go by very quickly.

Finally, I would like to acknowledge the financial support of the University of Victoria.

to my parents

# Chapter 1

## Introduction

### 1.0 Purpose and Scope

The field of computational fluid dynamics (CFD) has seen considerable growth recently due to the availability of low cost, high speed computers. One of its major applications is the modeling of convective heat transfer. The trend in new designs of mechanical and electrical systems involving heat generation or transfer is size reduction. Reducing the size of heat producing components limits the area available to dissipate heat, thereby raising component temperatures and reducing component life span. Techniques used to remove heat from such equipment has traditionally been designed using empirical heat transfer functions correlated from experimental data. Unfortunately, empirical functions stipulate specific flow and boundary configurations. CFD offers the ability to predict flow through unique flowfield configurations without the expense of time consuming experimental modeling. In addition, parametric studies are readily performed giving the designer a better overall understanding of the flow.

CFD simulates the fluid flow, its associated heat transfer and their interaction with solids through the numerical modeling of differential equations expressing conservation of mass, momentum, and energy. These coupled equations are non-linear and numerical modeling is the only feasible solution method for complex flowfields.

Most CFD methods are based on the calculation of a single computational block or domain. Although these methods are robust, there are situations where the ability to break the flowfield into smaller blocks, or subdomains, would be advantageous. This “divide and conquer” strategy can be particularly effective in parallel computing applications. Each subdomain could be assigned to one of the processors with the potential of greatly reducing computation time. Another case is the simplification of grid refinement. Efficient spacing in the computational grid increases the speed of solution, but adjacent grid cells share faces so localized size refinement propagates across the entire domain and is inefficient. Adjacent subdomains do not have this constraint allowing refinement to be placed locally. Additional advantages can be gained through the simplification of gridding, for some complex domains, and by a reduction in memory requirements. Subdividing a computational domain into subdomains is called domain decomposition (DD).

The purpose of this study is to implement domain decomposition in a numerical fluid flow and heat transfer solver and to evaluate its performance. A second goal is to use domain decomposition to solve simultaneously solid and fluid, or conjugate, heat transfer problems for a practical engineering application. The test case chosen to demonstrate the practical application of domain decomposition and conjugate heat transfer is the high blockage ratio rib, which is a generic model of an electronic component cooled by forced convection.

## 1.1 Description of Flowfield Characteristics

Three test cases will be used to study the accuracy and simulated parallel efficiency of the domain decomposition method. These are, developing flow between parallel plates, flow over a low blockage ratio surface mounted rib, and flow over a high blockage ratio surface mounted rib.

### 1.1.1 Parallel Plates

A half domain is used to represent developing flow between parallel plates. For this study the upper or North boundary is a solid wall, and the lower or South boundary is a symmetry line. The domain is illustrated in figure 1.1.



Figure 1.1: Schematic of parallel plate flowfield.

Parallel plate flow is a good first test case of DD because it is a relatively simple flow for which an exact solution of the fully developed velocity profile is known. Convective flow at the entrance tests the accuracy and stability of DD, while the calculated entrance development length is a good measure of solution accuracy. This type of flow is thoroughly documented providing a large base of comparative material.

### 1.1.2 Surface Mounted Ribs

Surface mounted ribs produce a class of flows called separated flows. These flows are characterized by a recirculating flow region commonly referred to as a “separation bubble”. Flow separation is created by either an abrupt change in geometry or a strong adverse pressure gradient. Figure 1.2 shows the relative extent and position of recirculation zones commonly found with rib flows. This type of flow is found in a wide range of engineering applications as well as in nature. In the context of heat transfer applications, it has been observed that an improvement in heat transfer occurs at the reattachment point of recirculation zones. This property and the complexity of the recirculating flow have lead to the wide spread study of separated flows.



Figure 1.2: Common recirculation configuration associated with flow over a surface mounted rib.

Surface mounted rib flows provide a more severe test of the DD method because strong gradients are formed around the rib and because of the elliptical nature of the recirculating flow region. Also, accurate numerical representation of rib flows require a higher grid node density and closer attention to node spacing than for the parallel plate case. These stricter requirements, along with the possibility of exploiting simpler grid arrangements afforded by DD, make rib flows attractive test cases.

Two types of surface mounted rib configurations were studied, low blockage ratio ribs and high blockage ratio ribs. Blockage ratio, BR, is defined as the ratio of channel height to rib

height. Low blockage ratio ribs are a class of flows where the mean flow through a channel is not significantly affected by the blockage of the rib. With high blockage ratio ribs the upper wall significantly affects the flowfield. Variations of rib aspect ratio, AR, defined as the ratio of rib length to rib height, were also incorporated.

## 1.2 Literature Review

This work draws on several disciplines and an exhaustive review is not possible, rather an attempt was made to review representative articles in all areas of study that this work touches: domain decomposition, fluid dynamics of separated flows, channel flows, convective heat transfer and cooling of electronic components.

### 1.2.1 Domain Decomposition

The literature related to domain decomposition is diverse because it has analytical as well as numerical applications. A paper published in 1869 by Schwarz, cited in Olinger *et al* [1], first described a method for linking several subdomains, referred to as the Schwarz Alternating Method (SAM). At the time, it was used to obtain analytic solutions to elliptical partial differential equations.

More recently, Olinger *et al* [1] have analyzed the convergence rates of a SAM solution to the Poisson equation using a block Gauss-Seidel iteration procedure. The subdomain grids were overlapped so that boundary information could be passed. They introduced over relaxation at the subdomain overlaps. Their conclusions were:

- Convergence is independent of grid spacing.
- The convergence rate is accelerated by overlap over relaxation.
- Smaller grid overlaps result in faster convergence.
- As the grid overlap is decreased, the optimum over relaxation value increases and over relaxation sensitivity increases.
- Changing the sequence of subdomain iterations has only a small effect on convergence.

Although their calculations were based on the solution of the Poisson equation, the trends are thought to apply to most elliptical partial differential equations.

Ewing [2, 3] has published several surveys of FEA domain decomposition techniques and their applicability to parallel processing and local grid refinement.

Atta [4, 5] and Rai [6] have implemented domain decomposition for the transonic flow regime. Atta and Vadyak [4] describe the application of domain decomposition for modeling potential flow around a three-dimensional wing/pylon/nacelle aircraft configuration. Their model links O-type body fitted grids with an outer Cartesian grid. An interpolation scheme was developed to transfer boundary information across overlapping subdomains. They concluded that the DD method was accurate and stable.

Rai [6] examined the relative merits of zonal and overlap subdomain interfaces for solutions of the Euler equations. The zonal method passes subdomain information by calculating fluxes at subdomain boundaries instead of through an overlap region. He also developed methods to preserve subdomain and domain continuity with a conservative

interface scheme. The use of domain decomposition was demonstrated for the modeling of flow past a rotor stator configuration. Two subdomains linked with a conservative zonal interface were used in the model. The two subdomains were allowed to move relative to each other in time. It was concluded that DD is a powerful method for computing flows around complex geometries and that conservative interfaces improve solution accuracy and stability. Overlapped interfaces were not used because it is more difficult to ensure continuity, although it was conceded that overlapping grids allow greater grid generation flexibility.

A full laminar Navier-Stokes solution with domain decomposition was implemented by Suga *et al* [7]. Their work used non-aligned Cartesian grids to model louvered heat exchanger fins. Interface information was passed with overlapped grids and linear interpolation. There was no mention of any attempt to ensure mass conservation. Both velocity and thermal fields were solved. The numerical solutions compared well with experimental data.

Perng and Street [8, 9] outline the use of domain decomposition for adaptive local grid refinement with the incorporation of a multigrid strategy to improve convergence. Their implementation relies on grid overlaps to pass subdomain information. Recently, they described an implementation of DD where velocity fields are solved on the subdomains while pressure is calculated for the entire flowfield [9]. Many of the important issues associated with overlapping grids were also discussed. It was pointed out that the minimum overlap distance should allow for at least one calculated node over the boundary of an adjacent domain. This distance will vary with the discretization method used. Central differencing and first order upwind discretization, such as the Hybrid method, require

minimum overlaps of two nodes while higher order discretization schemes such as QUICK<sup>1</sup> requires a minimum overlap of three nodes.

Braaten [10, 11] and Gropp & Keyes [12] describe the implementation of DD on parallel computers. Their studies applied the hypercube parallel architecture. Issues such as parallel efficiency, convergence behavior, and memory architecture were addressed. The most significant finding was that parallel efficiency dropped as the number of subdomains and processors was increased. Also, an optimum number of subdomains exists for each specific problem. Braaten [11] found that the pressure calculation limits the speed of convergence. He increased the number of pressure sweeps per iteration to palliate this.

## 1.2.2 Parallel Plates

Investigation of developing flow between parallel plates has been approached using a variety of methods. A classical theoretical solution, which gives a reasonable estimation of development length, was published by Schlichting in 1934 [13]. It combines the Blasius boundary layer solution with continuity to produce this relation for development length,

$$X_L = 0.04h \cdot Re_h. \quad (1.1)$$

Shah and London [14] reviewed laminar convection in ducts where they summarize much of the experimental and numerical work concerning parallel plate flow. Empirical relations correlated from experiments and tabulated numerical data for the entrance development length are given. In the development region, a small velocity overshoot was found where

---

<sup>1</sup> QUICK: Quadratic Upstream Interpolation for Convective Kinematics

the boundary layer and the inviscid core meet. This phenomenon was quantified and explained.

A number of useful numerical results which correlate entrance development length with a non-dimensional pressure drop parameter are reviewed by White [15].

### 1.2.3 Low Blockage Ratio Rib

The rib is used as a generic model for heat transfer enhancement devices or for cooling of electronic components. The low blockage ratio rib has often been used as a test case for turbulent flow calculations. A number of numerical studies for laminar flow have been reported in the literature, however, there has been little experimental work done on laminar rib flow.

Hong *et al* [16] conducted a numerical study of laminar rib flow. The domain configuration differed from the present study in that the rib was mounted in a free flow rather than a channel. The location and extent of all recirculation bubbles were documented for a range of Reynold's numbers, rib aspect ratios and upstream boundary layer thicknesses. The computations were performed using a stream function-vorticity formulation with a power law discretization scheme. Several trends can be observed from their data:

- The trailing recirculation zone length increases with Reynolds number and increasing boundary layer thickness,  $\delta$ .

- Trailing recirculation zone length decreases with decreasing rib aspect ratio (longer rib).
- A recirculation zone on the top of the rib appears only for low rib aspect ratios and thin upstream boundary layers. ( $\delta < 0.5 h$ )
- For upstream boundary layers of  $\delta < 0.5 h$  and a rib aspect ratio of 1.0 the trailing recirculation zone starts on the top of the rib.
- The dimensions of the stagnation recirculation zone increase with increased Reynolds number and boundary layer thickness, but are independent of rib aspect ratio.
- The small counter recirculation zone expands with increasing Reynolds number and shrinks with decreasing rib aspect ratio and boundary layer thickness.

An attempt was made to correlate the trailing recirculation zone length with Reynold's number, rib aspect ratio and boundary layer thickness. An accuracy of  $\pm 20\%$  is observed with the correlation. The discrepancy stems from the boundary layer thickness parameter which seems to have a discontinuous effect on reattachment length in the region of  $\delta \approx 0.5h$ .

Convective heat transfer from low blockage ratio ribs has been computed by Hsieh and Huang [17] to correlate mean Nusselt number with Reynold's number and aspect ratio. The resulting function has an uncertainty of  $\pm 25\%$ . Their study assumes a constant rib temperature which tends to over predict local Nusselt numbers at the rib corners skewing the average Nusselt number. In practice, the rib corners would have the lowest wall temperature which would be reflected by lower local and average Nusselt numbers.

### 1.2.4 High Blockage Ratio Rib

The literature published concerning high blockage ratio ribs is concentrated on its application to the modeling of cooling of electronic components. This configuration is a good model of densely populated electronic circuit boards.

Some of the first findings in this area were reported by Kennedy and Zebib [18]. Their numerical and physical experiments measured the thermal effects induced by local heat sources imbedded in the walls of parallel plates. Both forced and natural laminar convection were investigated. It was found that there is a strong axial conduction effect in the channel wall which is difficult to replicate numerically. Also, when natural convection is significant, devices that are being cooled should be placed on the lower wall of a horizontal channel for best effect.

Ramadhani *et al* [19] conducted a numerical analysis of imbedded local heat sources with the addition of a conjugate heat transfer analysis of the wall. To address the concerns of axial heat transfer noted in [18], wall thermal conductivity was varied and the resulting heat transfer was tabulated. It was found that wall conduction had a significant influence on heat transfer from the heat sources.

Heat transfer from a series or array of high blockage ratio ribs has been studied by many workers including Braaten & Patankar [20], Sparrow & Chukaev [21], Davalath & Bayazitoglu [22], Zebib & Wo [23] and Kim *et al* [24]. In most cases, both forced and natural convection from ribs mounted in a channel were investigated. The typical configuration consists of a series of three ribs with aspect ratios of 0.5 and blockage ratios

of 0.50. Factors such as rib spacing, Reynold's number and Prandtl number are varied. There is a significant difference between the various studies in the thermal boundary condition treatment at the rib, however. Treatments range from constant wall temperature to conjugate heat transfer with micro heat transfer inside the rib. Many workers also incorporate cyclic boundary conditions on the upper and lower walls to simulate an array of stacked components. In this configuration, the wall conductivity is also calculated. Some of the common conclusions were:

- Wall conductivity and cyclic boundaries influence thermal results.
- For low Reynold's number flow, natural convection has a significant positive effect on heat transfer.
- Conjugate heat transfer results in more realistic thermal models than the traditional constant wall temperature method.

Davalath & Bayazitoglu [22] used conjugate heat transfer and specified the heat generated inside the rib. The generation was spread evenly through the constant conductivity rib. Kim *et al* [24] concentrated the thermal generation along a strip inside the rib. This model is a more realistic simulation of an electronic component. Both workers used the maximum internal rib temperature to quantify their results. Maximum temperature is a more appropriate measure of overall thermal performance than average Nusselt number in this case. Maximum temperature is also one of the criteria used to estimate component reliability by electronic designer. It is worth noting that in both papers the discontinuous conductivity of the fluid solid interface is not accounted for using Pantankar's [25] harmonic mean method of thermal conductivity matching. This would result in an over

prediction of the convective heat transfer and an under prediction of maximum rib temperature.

### 1.3 Outline of Thesis

In this thesis, a domain decomposition method is developed to compute laminar flow and convective heat transfer. The computations are based on the solution of the two-dimensional Navier-Stokes equations and energy equation using primitive variables, and a finite volume discretization method. The method is applied to the developing flow between parallel plates and to low and high blockage ratio rib flows.

Chapter 2 describes the numerical methods used to solve the flowfield. The Navier-Stokes equations are presented and recast into a general transport equation. The finite volume method is applied to the general transport equation and a solution procedure is presented. Thermal and flow boundary conditions are described along with the methods of grid generation and convergence measurement.

Chapter 3 introduces the domain decomposition method. Numerical issues such as program structure, subdomain interface treatment, memory management and parallel computer implementation are addressed.

Chapter 4 presents the results of two test cases where domain decomposition was applied. Several subdomain configurations of parallel plate flow and low blockage ratio rib flow are evaluated. Accuracy of the multi-domain configurations is compared to single domain solutions and a parallel efficiency is calculated for each case.

Chapter 5 presents the results of domain decomposition applied to the calculation of flow over and heat transfer from a high blockage ratio surface mounted rib. Flowfield and thermal characteristics are evaluated. The maximum temperature inside the rib is monitored and compared with various flow and boundary configurations.

Chapter 6 concludes the thesis with a summary of the significant findings and provides a few suggestions for further work.

# Chapter 2

## Computational Method

### 2.0 Background

CFD is based on the numerical solution of the Navier-Stokes equations. These equations can describe both laminar and turbulent flows over a wide range of flow conditions. The most general formulation of these equations are indicated by equations 2.1 and 2.2, which describe conservation of mass and momentum, respectively. Exact solutions to these equations are limited to a few highly idealized situations. Numerical solutions, however, have been presented for many complex engineering applications.

$$\frac{D\rho}{Dt} + \rho \cdot \text{div} \vec{V} = 0 \quad (2.1)$$

$$\rho \frac{D\vec{V}}{Dt} = \rho \vec{g} - \vec{\nabla}P + \frac{\partial}{\partial x_j} \left[ \mu \left( \frac{\partial v_i}{\partial x_j} + \frac{\partial v_j}{\partial x_i} \right) + \delta_{ij} \lambda \cdot \text{div} \vec{V} \right] \quad (2.2)$$

Equations 2.1 and 2.2 are too general for most engineering requirements, but the application of a few strategic simplifying assumptions reduces them to a usable form while retaining accurate results. The flows under consideration in this study are assumed to be steady, laminar, incompressible, two-dimensional, absent of body forces, and have constant properties. Applying these assumptions, the Navier-Stokes equations reduce to,

$$\frac{\partial u}{\partial x} + \frac{\partial v}{\partial y} = 0 \quad (2.3)$$

$$\rho \left( u \frac{\partial u}{\partial x} + v \frac{\partial u}{\partial y} \right) = -\frac{\partial P}{\partial x} + \mu \left( \frac{\partial^2 u}{\partial x^2} + \frac{\partial^2 u}{\partial y^2} \right) \quad (2.4)$$

$$\rho \left( u \frac{\partial v}{\partial x} + v \frac{\partial v}{\partial y} \right) = -\frac{\partial P}{\partial y} + \mu \left( \frac{\partial^2 v}{\partial x^2} + \frac{\partial^2 v}{\partial y^2} \right). \quad (2.5)$$

The energy equation, which is required for problems involving heat transfer, takes the following form,

$$\rho \left( u \frac{\partial T}{\partial x} + v \frac{\partial T}{\partial y} \right) = \frac{k}{c_p} \left( \frac{\partial^2 T}{\partial x^2} + \frac{\partial^2 T}{\partial y^2} \right). \quad (2.6)$$

It is useful, for the purpose of the numerical method formulation, to recast the simplified equations in the form of the generalized transport equation

$$\rho \frac{\partial}{\partial x} (u\phi) + \rho \frac{\partial}{\partial y} (v\phi) = \frac{\partial}{\partial x} \left( \Gamma \frac{\partial \phi}{\partial x} \right) + \frac{\partial}{\partial y} \left( \Gamma \frac{\partial \phi}{\partial y} \right) + S_\phi. \quad (2.7)$$

In this formulation,  $\phi$  is the transport quantity,  $\Gamma$  is the generalized diffusivity coefficient, and  $S_\phi$  is the generalized source term. Any transport quantity can be represented by the

manipulation of these variables. Table 2.1 lists the modifications necessary to represent all transport quantities used.

These equations, although simplified, form a system of coupled nonlinear partial differential equations. Numerical methods are the only techniques available to solve them over a complex domain.

Table 2.1: Generalized transport equation coefficients and source terms

Equation	$\phi$	$\Gamma$	$S_\phi$
Continuity	1	0	0
$x$ -Momentum	$u$	$\mu$	$-\frac{\partial P}{\partial x} + \frac{\partial}{\partial x} \left( \mu \frac{\partial u}{\partial x} \right) + \frac{\partial}{\partial y} \left( \mu \frac{\partial v}{\partial x} \right)$
$y$ -Momentum	$v$	$\mu$	$-\frac{\partial P}{\partial y} + \frac{\partial}{\partial x} \left( \mu \frac{\partial u}{\partial y} \right) + \frac{\partial}{\partial y} \left( \mu \frac{\partial v}{\partial y} \right)$
Temperature (fluid)	$T$	$\mu/Pr$	0
Temperature (solid)	$T$	$k/c_p$	0

## 2.1 Finite Volume Formulation

Numerical solution methods for the Navier-Stokes equations fall into two major groups, finite element analysis (FEA) and the finite difference method. In this study, a subset of the finite difference method, the finite volume (FV) method, was used. This method is implemented in the TEACH code which was used as a basis for this work. The finite volume method applies a finite difference discretization with continuity conservation enforced at each computational node. Continuity is applied through an integration of

fluxes around each control volume. The following description of the finite volume formulation is paraphrased from the work of Pantankar [25].

As with all finite difference methods, the continuous generalized transport equation must be rewritten in a discrete form. The flowfield is divided into a structured grid of finite volumes to which the discretized equations are applied.

The general transport equation 2.7 is integrated over the control volume, yielding

$$\iint_{cv} \left[ \frac{\partial}{\partial x}(\rho u \phi) + \frac{\partial}{\partial y}(\rho v \phi) - \frac{\partial}{\partial x} \left( \Gamma \frac{\partial \phi}{\partial x} \right) - \frac{\partial}{\partial y} \left( \Gamma \frac{\partial \phi}{\partial y} \right) \right] dx \cdot dy = \iint_{cv} S_\phi dx \cdot dy \quad (2.8)$$

The generalized diffusivity coefficient,  $\Gamma$ , and density,  $\rho$ , are assumed to remain constant with respect to  $x$  and  $y$ . The source term and  $u$  and  $v$ -velocities are assumed to be constant across each control volume. Figure 2.1 shows a control volume with grid dimensions and cell face fluxes. Invoking Gauss' divergence theorem, the volume integral can be transformed into surface integrals; therefore, equation 2.8 becomes,

$$\begin{aligned} \int_s^n \left[ \left( \rho u \phi - \Gamma \frac{\partial \phi}{\partial x} \right)_e - \left( \rho u \phi - \Gamma \frac{\partial \phi}{\partial x} \right)_w \right] \cdot dy + \int_w^e \left[ \left( \rho v \phi - \Gamma \frac{\partial \phi}{\partial y} \right)_n - \left( \rho v \phi - \Gamma \frac{\partial \phi}{\partial y} \right)_s \right] \cdot dx \\ = \iint_{cv} S_\phi dx \cdot dy \end{aligned} \quad (2.9)$$

where the subscripts  $n$ ,  $s$ ,  $e$  and  $w$  indicate the North, South, East and West faces of the control volume. Equation 2.9 is exact. To complete the discretization, equation 2.9 is expanded to an algebraic form where the diffusive and convective terms are combined to

form cell face flux terms. A second order accurate and relatively straight forward representation of these terms can be obtained using a central difference approximation. An unfortunate property of this discretization procedure is that it tends to become numerically unstable when used to solve highly convective flows (high Reynold's numbers). The instabilities stem from the occurrence of negative flux coefficients. The mechanism by which the negative fluxes initiate numerical instabilities has been omitted, but the method used to alleviate the problem is presented.

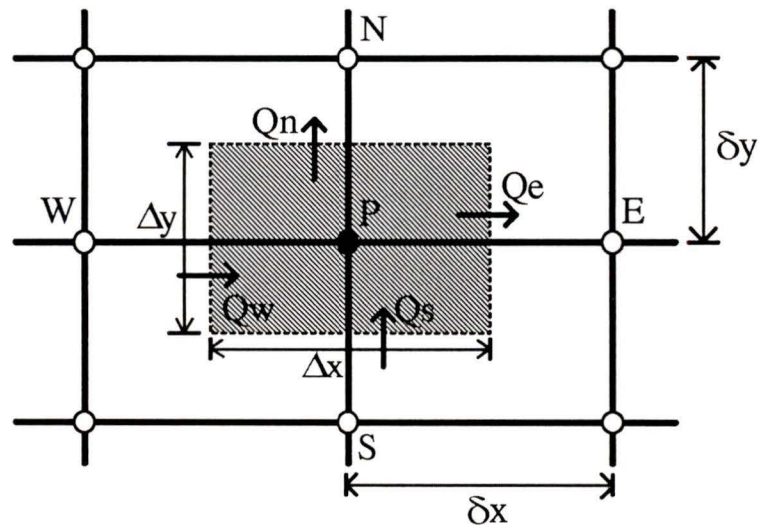


Figure 2.1: Finite volume cell at node P with cell face fluxes and dimensions indicated.

The numerical instability is removed by replacing, in the evaluation of the convective terms, the linear variation of  $\phi$ , assumed in central differencing, by a stepwise variation. This leads to a formulation which is unconditionally stable, but only first order accurate, and, for some flows, it tends to result in an over estimation of the diffusive fluxes. This problem is referred to as false or numerical diffusion. An improvement on this, the

Upwinding method, based on the exact solution of the one-dimensional general transport equation, is known as the Hybrid method. This method takes advantage of the superior accuracy of the central differencing scheme at low Peclet numbers,

$$Pe = \frac{u_i \Delta x_i}{\Gamma/\rho}, \quad (2.10)$$

corresponding to low Reynolds number flows. At high Peclet numbers, corresponding to convection dominated flow regions, upwinding is applied to evaluate the convective fluxes. The switch-over from central to upwind differencing takes place where  $|Pe| \geq 2$ . A detailed discussion of numerical instabilities, the Upwinding method and the Hybrid method can be found in Pantankar [25].

Finally, to complete the discretization of equation 2.8, the source term  $S_\phi$ , is linearized in the form,

$$S = S_c + S_p \phi_p. \quad (2.11)$$

### 2.1.1 Computational Cells

Cell boundaries are defined over the flow domain by a continuous structured grid. A structured grid requires each cell to share its faces with the adjacent cells. This ensures continuity between the cells but limits the ability to locally refine the cell size. The size of a cell is important as the value being computed is assumed to be constant inside each cell. If cells are too large the accuracy of the resulting solution is reduced. Cell size can be

adjusted, or refined, in areas known or presumed to have high gradients by varying grid spacing.

Attempts to calculate both velocity components and scalar pressure values at the same location results in the so called checkerboard pressure field described in [25]. In a checkerboard pressure field, pressure values oscillate from node to node in both the  $x$  and  $y$  directions. This numerical obstacle is eliminated by the process of staggering the velocity cells. Three grids are used to calculate a flowfield. Scalar values are calculated with a cell centered at each grid intersection while velocity is calculated in cells offset by half a grid space. Figure 2.2 shows the location of  $u$  and  $v$ -velocity cells relative to the pressure cell. This configuration is called backward staggering.

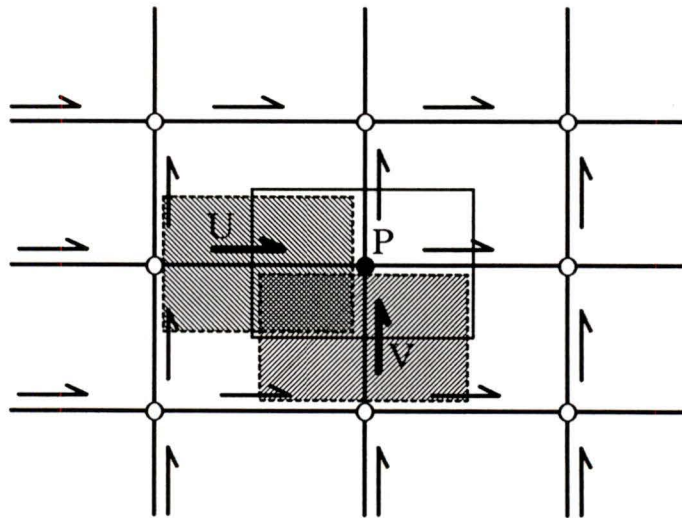


Figure 2.2: Backward staggered grid showing the location of  $u$  and  $v$ -velocity cells relative to the pressure cell.

Staggering the velocity nodes conveniently places velocity values directly on each of the scalar cell faces eliminating the need for an interpolation step. An additional advantage is

that velocity nodes are ideally located for velocity gradient calculation used to solve for the pressure field.

### 2.1.2 Solution Procedure

Each of the component equations presented to this point must be linked by a numerical solution procedure. The procedure used to accomplish this was developed by Pantankar [25] and consists of an iterative solver procedure coupled with the SIMPLE<sup>2</sup> pressure correction algorithm. The solver algorithm is based on an implicit line by line solution strategy where a line of nodes, extending from the North to the South of the domain, is solved explicitly, while the explicit solution is swept from West to East across the domain. In this manner, boundary conditions from the domain walls are passed to the center of the domain. The explicit calculation requires the inversion of a tridiagonal matrix. The Thomas algorithm is used for this task as it is very efficient.

The SIMPLE pressure correction procedure used to obtain a full linked solution, is as follows:

- Guess a pressure field,  $p^*$ .
- Solve momentum equations,  $u^*$ ,  $v^*$ .
- Solve pressure correction equation.
- Implement pressure correction to obtain a new pressure field,  $p$ .
- Correct the velocity values with the pressure field,  $p$ .

---

<sup>2</sup> SIMPLE: Semi Implicit Method for Pressure Linked Equations.

- Solve the general transport equation for any additional  $\phi$  (temperature for example)
- Substitute  $p$  as  $p^*$  and repeat until convergence is achieved.

Residuals are calculated from the two momentum equations, the pressure equation and any additional transport equations. Due to the non-linearity of the transport equation, an under relaxation scheme is implemented for each transport quantity to assist convergence.

## 2.2 Application

### 2.2.1 Flow Boundary Conditions

The discretized equations described can, with the addition of appropriate boundary conditions, model any fluid flow governed by equations 2.3, 2.4 and 2.5. Four types of boundary condition are necessary, in general: solid wall, symmetry, inlet and outlet conditions. The implementation of these boundary conditions is discussed in this section for the general case of a straight boundary as well as for the special case of corner boundaries.

The boundary condition for a solid North wall requires the no slip condition at the wall and zero mass flux through the wall. Figure 2.3 shows the boundary cells at the North wall. Zero mass flux is accomplished by setting convective and diffusive flux for the North face of the  $V''$  cell and the North face of the  $U$  cell to zero. In addition, the  $v$ -velocity in the  $V'$  cell is set to zero. The  $U$  velocity cell source term is modified to take wall shear

stress into account. Appendix A outlines the source term modifications used in the boundary conditions.

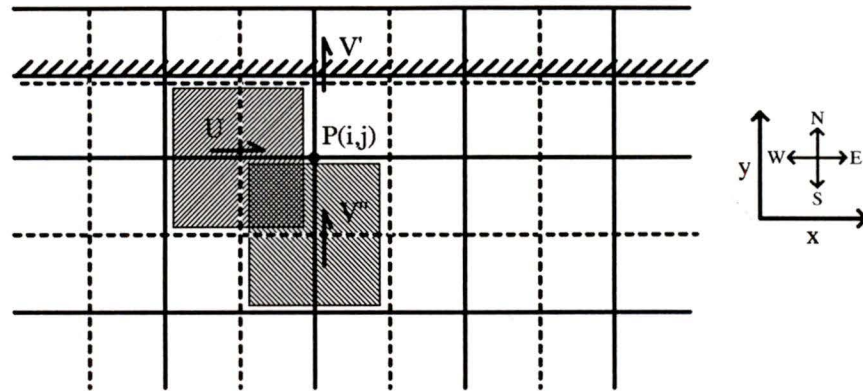


Figure 2.3: North wall solid boundary treatment.

This formulation is inaccurate because the  $V''$  velocity cell does not extend to the wall, but North cell fluxes are set to zero. Staggered grids make this inaccuracy unavoidable; however, highly refined near wall grids, and the nature of the flow in a near wall region, minimize the error.

The South wall boundary condition is similar to the North, as shown in figure 2.4. The zero flux condition is imposed by setting South U velocity and V velocity cell fluxes to zero. V-velocity is set to zero and the U velocity cell source term is modified to account for wall shear stress.

Facing walls or upstream walls are illustrated in figure 2.5. Zero flux through the wall is implemented by setting the East fluxes for  $U'$  and V velocity cells to zero. Also,  $U''$  velocity is set to zero and the V velocity cell source term is modified to account for wall

shear stress. As with the North boundary condition, setting the East cell flux for  $U'$  to zero is not rigorously correct.

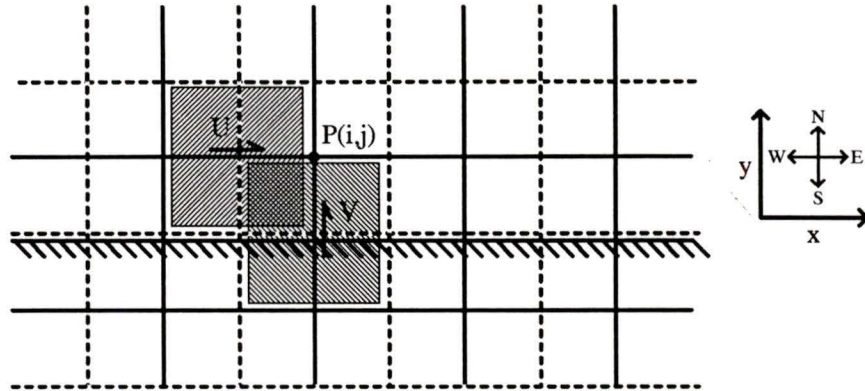


Figure 2.4: South wall solid boundary treatment.

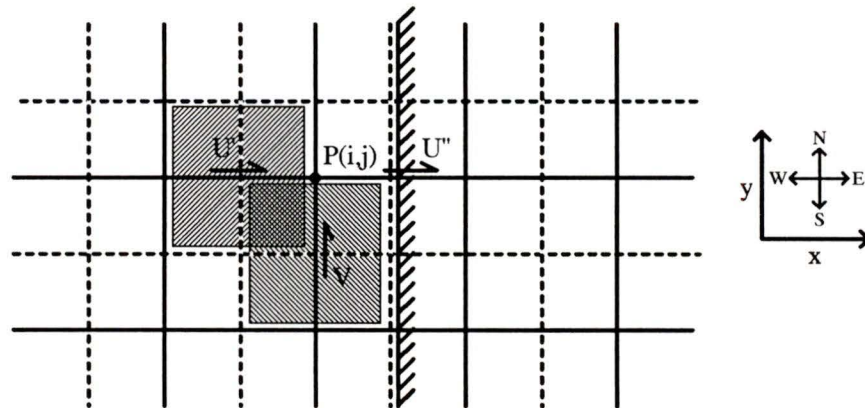


Figure 2.5: Facing wall solid boundary treatment.

The trailing wall boundary condition is illustrated in figure 2.6. West cell fluxes for the  $U$  and  $V$  velocity cells are set to zero and the  $V$  velocity cell source term is modified to take wall shear stress into account.  $U$ -velocity at the wall is set to zero.

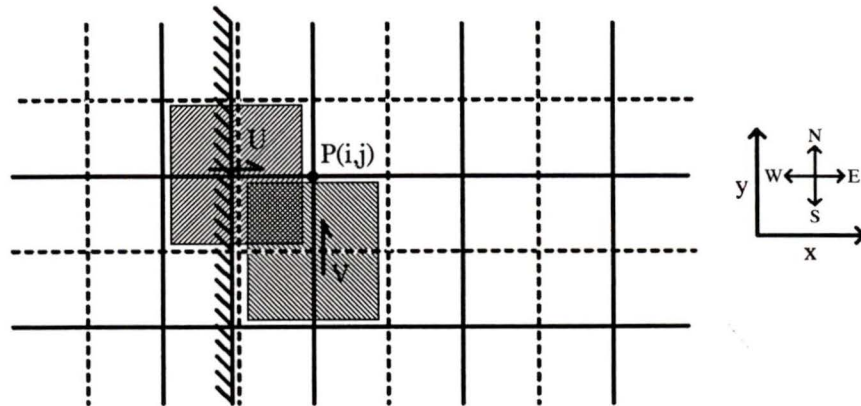


Figure 2.6: Trailing wall solid boundary treatment.

A South symmetry boundary condition is shown in figure 2.7. To achieve symmetry, convective and diffusive fluxes across the boundary are set to zero and the  $U''$  velocity is set equal to the  $U'$  velocity. In addition, South velocity cell flux is set to zero for the  $U'$  and  $V$  velocity cells, and the  $V$  velocity is set to zero.

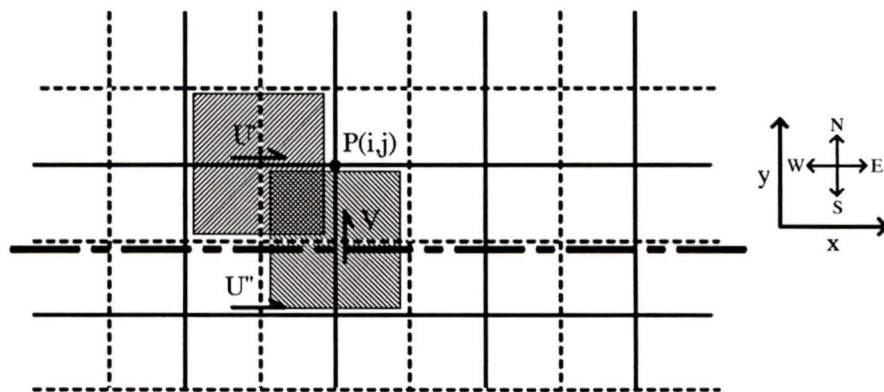


Figure 2.7: South symmetry boundary treatment.

The entrance boundary condition consists of either a uniform or a parabolic u-velocity profile specified by modifying the first column of velocity cells. V-velocity is set to zero at the entrance in the same manor.

An exit boundary condition is calculated to ensure domain continuity. To achieve this, mass flux is calculated at the entrance and at the second last column of u-velocity cells. The difference between the two mass fluxes is used to correct the second last column of u-velocity cells which are imposed as the exit boundary condition. V-velocity cells are set to zero at the exit. This exit treatment requires a fully developed exit flow. If the flow is not fully developed, flow features such as recirculation zones tend to be exaggerated.

Implementing wall boundary conditions in areas other than at the domain boundaries will create blocked cells. These cells must be calculated, but their velocity and pressure values are irrelevant. There are two methods that allow these cells to exist in isolation from the flowfield. One method imposes very large values of viscosity in the blocked cells. The preferred method modifies the blocked cell momentum source terms to ensure zero velocity [25]. The source term blockage method is used because it is more numerically direct.

These boundary conditions are sufficient to reproduce most of the possible rectangular physical scenarios. However, two additional boundary conditions will be needed to model sharp corners accurately. Figure 2.8 shows the leading corner boundary condition. This boundary condition is imposed along with the solid wall boundary conditions. A portion of each corner velocity cell is blocked, effectively blocking a portion of that cell face's flux. The original flux calculation would use, for example, the average velocity of  $U'$  and  $U''$  to

determine the East flux for the  $V'$  velocity cell. This calculation method tends to under-predict the velocity at the corner. Corner velocity is corrected by using only the  $U'$  velocity and unblocked cell area to calculate the East flux for the  $V'$  velocity cell. Durst and Rastogi [26] found a substantial improvement in reattachment length prediction for the case of flow past a rib when this method was implemented. The same procedure is used to correct the South fluxes of the  $U'$  velocity cell.

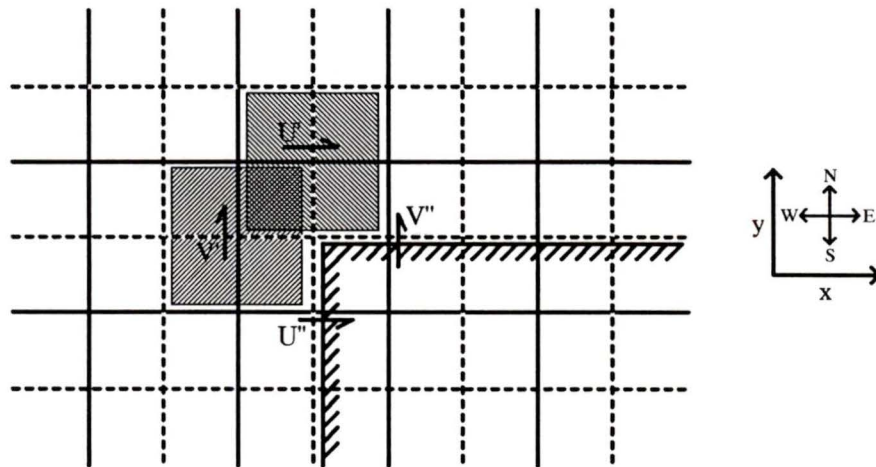


Figure 2.8: Leading corner boundary treatment.

Figure 2.9 shows the trailing corner boundary condition. Procedures similar to those implemented for the leading corner are used to correct trailing corner fluxes.

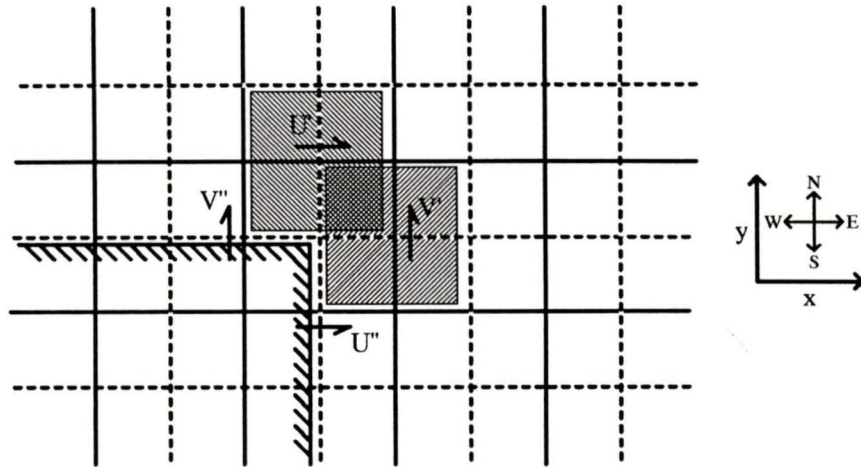


Figure 2.9: Trailing corner boundary treatment.

## 2.2.2 Thermal Boundary Conditions

The solution of secondary scalar quantities, such as temperature, requires the addition of scalar boundary condition. These boundary conditions are specific to the quantity being modeled. In this instance, boundary conditions necessary to model a thermal field are presented.

Adiabatic boundaries are treated in a fashion similar to symmetrical flow boundaries. Figure 2.7 can be used to visualize the implementation, noting that the temperature calculations are done in non-staggered scalar cells. Unlike velocity cells, the faces of temperature cells always correspond to physical boundaries. The implementation for a South wall requires South convective and diffusive thermal fluxes to be set to zero and the temperature in the  $T''$  location to be set equal to  $T'$ . This description applies, with the appropriate fluxes and temperatures, to any wall orientation.

Constant temperature boundaries are described using figure 2.4, which offers an appropriate template. The temperature inside the wall is known and is applied as a computational boundary condition. For the cell next to the wall, the temperature source term is modified to take convective heat transfer into account and the facing flux term is set to zero.

Conjugate heat transfer is a method that links the solution of convective thermal fields to solid thermal fields. Traditional approaches to heat transfer analysis assume thermal boundary conditions, such as isothermal or adiabatic walls. These boundaries provide poor models of actual thermal boundaries found in engineering applications. Conjugate heat transfer removes the need to make boundary assumptions by incorporating the heat transfer of solids.

The thermal transport equation requires minor changes to the general diffusivity coefficient and the source terms to model heat transfer in solids. Since fluid velocities inside solids are set to zero by the momentum source term modification, the convective terms of the thermal transport equation are eliminated. This reduces the thermal transport equation to Fourier's heat transfer equation.

The interface between a fluid and solid requires a special treatment because of the discontinuous change in conductivity. On the inside of a conducting wall, the cell wall flux is recalculated using a harmonic mean of the fluid and solid thermal conductivity after Pantankar [25]. This procedure is only appropriate when the cell wall is midway between grid points. The fluid side boundary condition is treated as an isothermal boundary condition with the wall temperature being updated from the solid thermal calculation after

each iteration. Thermal energy is introduced into the system by means of heat generating cells as opposed to artificially fixing a wall temperature. A specified amount of thermal energy is divided evenly, with respect to cell area, over a range of cells. During the iteration process the temperature of the system fluctuates until a thermal equilibrium is reached. At this point, the same amount of thermal energy is convected out as is generated in the system.

### 2.2.3 Grid Generation

Optimum grid spacing is found through trial and error. The process by which the optimum grid is found begins with the generation of a uniformly spaced grid covering the entire domain. The solution produced will identify areas of high gradient. A non-uniform spacing is then designed to place a large number of cells in these areas. The flowfield is recalculated and significant flow features such as wall shear stress or recirculation zone length are monitored. The overall grid density is increased in steps until the flow features are independent of grid density.

To speed-up the time consuming grid refinement process, a spreadsheet was used to calculate grid spacing. Spreadsheets allow a graphical visualization of the grid before it is implemented. Also, some spreadsheets incorporate multi-variable solvers which allow three or four areas of contraction and expansion to be manipulated within domain boundary constraints. Appendix B shows a spreadsheet implemented grid and its graphical representation. Expansion factors, defined as  $E_x = \frac{\Delta x_{i+1}}{\Delta x_i}$  and  $E_y = \frac{\Delta y_{j+1}}{\Delta y_j}$ , were used to ensure smooth grid spacing transitions.

### **2.2.4 Convergence Criterion**

In any iterative procedure, a criterion of convergence must be defined. In this instance, where several equations are solved simultaneously, the convergence of each equation is monitored by calculating the mass, momentum and energy residuals for each computational cell. The absolute value of the residuals are summed over the entire domain and normalized with the appropriate inlet or source values. Convergence is declared when all equations achieve a minimum required normalized residual.

# Chapter 3

## Domain Decomposition

### 3.0 Background

Two of the major goals of many current efforts in CFD solution methodologies are improved flexibility and computational speed. One approach to achieve this is domain decomposition (DD), whereby a computational domain is divided into a number of subdomains which are linked at their boundaries. DD facilitates local grid refinement, custom solution placement and parallel implementation, in combination or independently. In a parallel implementation, each subdomain is solved by an independent processor, or group of processors. In a serial implementation, the subdomains are solved consecutively.

In addition to parallel processing, DD accommodates local grid refinement. A major limitation of structured grid methods is that adjoining computational cells are required to share faces. This makes it impossible to refine a mesh in areas of high gradients without

unnecessarily refining it in other areas. DD solves this problem by allowing neighbouring subdomains to have non-adjoining grids. Figure 3.1 illustrates this concept.

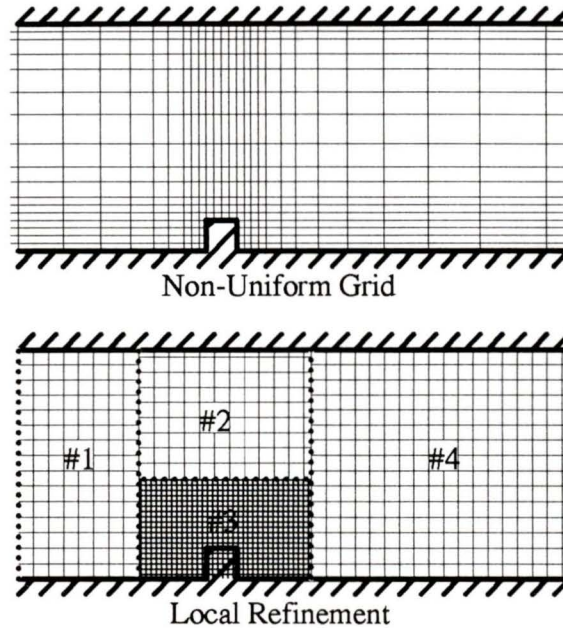


Figure 3.1: Examples of a structured non-uniform grid and local refinement implemented with domain decomposition.

Another difficulty in implementing structured grid methods is the process of efficiently gridding complex domains. In complex rectangular domains DD allows the piece-wise placement of subdomains. Creation and calculation of fluid cells inside solids are thereby avoided. Figure 3.2 shows an example of a double elbow domain implemented with a standard single domain and with domain decomposition. In more complicated problems, subdomains can be made to join at an angle or to move relative to each other.

Custom solution placement involves modification of the solution method over portions of the flowfield. It is possible to implement this in a single domain, but DD simplifies the

process. Custom solution placement is commonly used to implement higher order solution methods in areas of high gradients.

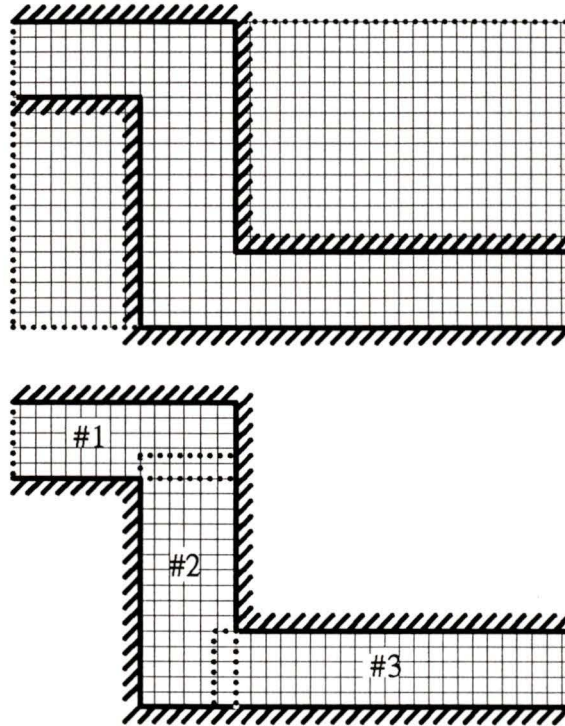


Figure 3.2: Double elbow domain gridded with a single domain and with three domains.

Finally, a serial benefit of DD is a potential saving of computational resources. The algorithms used to calculate flowfield and scalar quantities inevitably require temporary array storage. Memory savings can be obtained by the reduction of these temporary arrays to the size of the largest subdomain. The amount of memory saved is dependent on the number of temporary arrays and the size of the subdomains. Memory requirements for the TEACH code were found to be reduced by as much as 50% of the single domain case.

### 3.1 Computational Method

DD was implemented by modifying the single domain TEACH code. The implementation of DD involved the modification of the data structure in TEACH and the linking and transfer of data between adjacent subdomains.

A serial implementation of DD was added by modifying the arrays of each variable. The size of the arrays containing subdomain data was increased by one dimension to provide a subdomain pointer. This modification allows the original solution procedures to be retained with only minor modifications. Physical boundary conditions are applied in the standard fashion, taking subdomains into account.

The procedure used to link the system of subdomains is the Schwarz Alternating Method (SAM). The original SIMPLE algorithm is used to calculate subdomain velocity and scalar terms. After each subdomain is calculated sequentially, velocity and scalar values near the subdomain boundaries are used to update adjacent subdomain boundary conditions. The subdomain calculations proceed consecutively in a serial implementation and concurrently in a parallel implementation. Subdomains may be calculated more than once per system iteration and the order of calculation can be changed. Figure 3.3 is a flow diagram showing the TEACH solution procedure with domain decomposition. Additional functions required by DD are shaded.

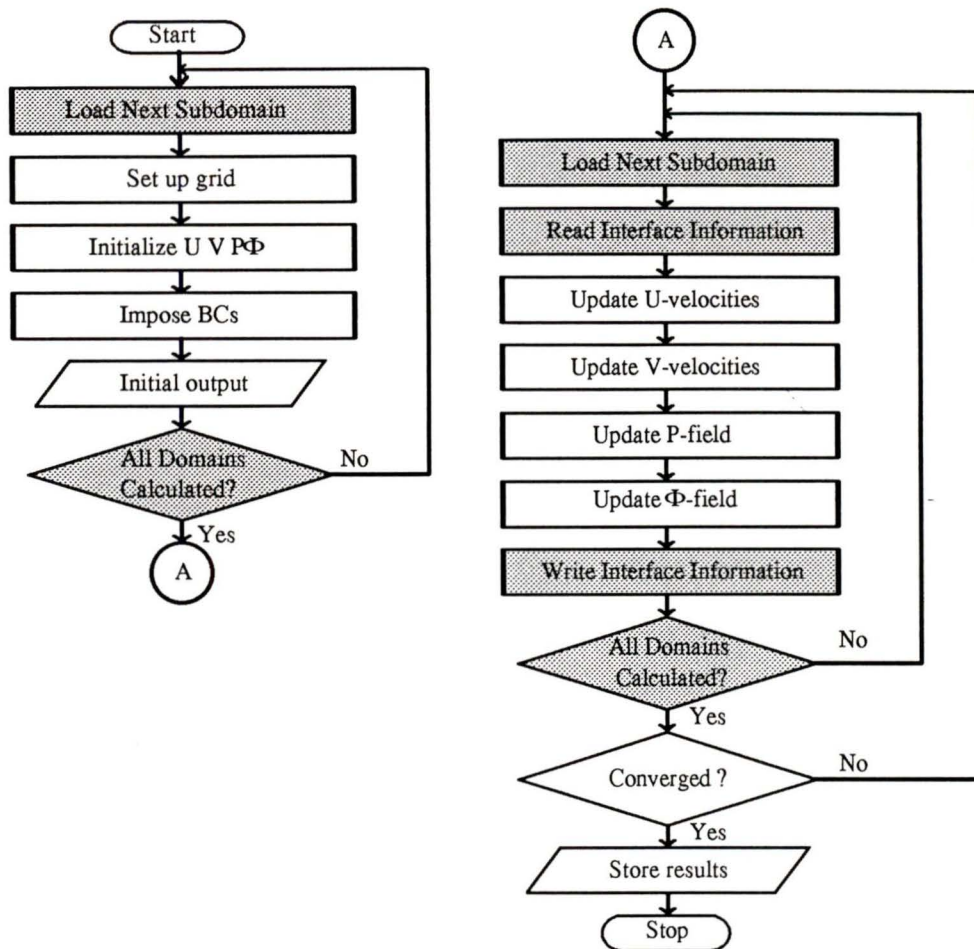


Figure 3.3: Flowchart of TEACH code with domain decomposition

Pressure is not passed across subdomain interfaces, but is calculated independently in each subdomain. After the entire flowfield converges, pressure values from each subdomain are normalized to produce a continuous pressure field.

Subdomain boundary conditions are updated by a grid overlap method which passes information across common overlapping subdomain nodes. The simplest variant of this method links identical subdomain grids. Other variants link body fitted grids to Cartesian

grids or grids of different spacing. A yet more complicated interface allows subdomain grids to move relative to one another. If linked subdomain grids are not identical, interpolation must be used to pass information and preservation of continuity at the interface becomes an issue. Identical subdomain grids will be used for the test cases. The more complicated interface configurations are beyond the scope of this study.

Backward staggering of the velocity nodes, which was discussed earlier, complicates the subdomain interface by requiring the linking of three overlapping grids. Figure 3.4 illustrates a horizontal interface with u-velocity, v-velocity, and scalar grids. The grids are shown with a small offset for clarity. The unused velocity cells shown in figure 3.4 are a consequence of backward staggering. Their occurrence in the interface region necessitates an extra overlap cell. Hybrid differencing, which uses a stencil that incorporates one node on each side of the calculated node, requires a minimum two node overlap to ensure that it is applied across the interface. Higher order differencing methods with larger stencils, such as QUICK, require more overlap. A three node overlap was used to accommodate the unused cell (v-velocity in this case) and hybrid differencing. Backward staggering requires the upper grid boundary cells to read u and v-velocity boundary conditions from different lower grid cells. The lower grid receives boundary information from the same upper grid cell.

Over relaxation factors (ORF) were applied to the interpolated interface values after Olinger *et al* [1]. Separate ORF values were used for the u and v-velocity and scalar fields. In some cases these values were further divided into horizontal and vertical interface values. Separate values could be given to each wall, to each direction of interpolation, and

to each quantity, but the time required to find the optimum values would outweigh any benefits to convergence rate.

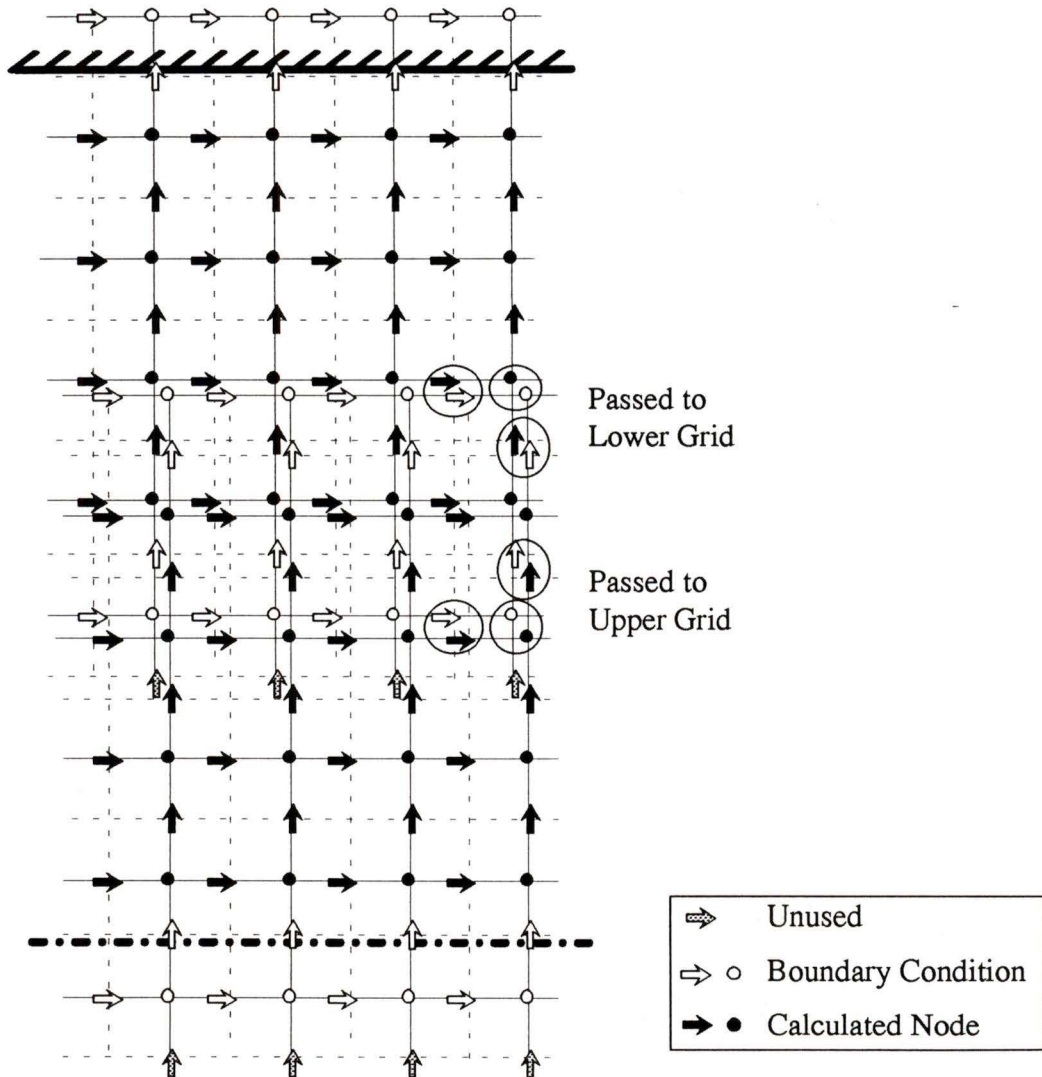


Figure 3.4: Location of overlapping grids at a horizontal interface.

To improve the convergence rate, a subdomain continuity boundary condition was designed. Total flux was calculated at the subdomain walls, then continuity was imposed

by modifying the velocity at an arbitrary subdomain boundary. Although this method seems drastic, at convergence, the correction is essentially nil. Most of the configurations investigated would not converge without a subdomain continuity correction.

Separation of the flowfield into subdomains requires that the convergence criterion be re-addressed. With a single domain, convergence is monitored with the sum of cell residuals over the entire computational domain. With DD, the sum of residuals of each subdomain must be combined to find a system residual. This system residual is not equivalent to a single domain residual because of differences in subdomain convergence rates. A stricter convergence criterion must be used with DD to account for this effect.

### **3.2 Optimization of Relaxation Factors**

Optimization of the under and over relaxation factors is important when convergence rates are being compared. The number of relaxation factors increases exponentially with the number of subdomains. The effort required to optimize the many possible factors is clearly greater than the potential return in faster convergence rates. Several reducing assumptions are made to simplify the optimization task. All subdomains were assigned the same solution under relaxation factors and all interfaces were assigned the same over relaxation factors. In one case, an exception was made where interface relaxation factors were further divided into horizontal and vertical values. These assumptions limit the maximum number of factors to seven. Also, it was found that interface and solution relaxation factors are only weakly linked, and therefore, can be optimized independently.

A consistent strategy must be employed to find the optimum values for each of these factors. A study of pressure correction algorithms by McGuirk and Palma [27] describes the sensitivity of the SIMPLE algorithm to under relaxation factors. Their test case is identical to the low blockage ratio rib test case used in this study. It is suggested that the optimization process be approached by setting the pressure factor to a relatively large value, approximately 0.5, and then consecutively optimizing u and v-velocity factors by a trial and error search. The interface over relaxation factors were optimized with a similar trial and error search.

### 3.3 Parallel Processing

Parallel computers are commonly classified into MIMD (multiple instruction multiple data) machines, typically composed of 2 to 256 processors, or SIMD (single instruction multiple data) machines consisting of up to several thousand processors. For MIMD machines, problems are divided into independent blocks solved on separate processors. For SIMD machines, computations are executed by assigning one processor to each datum or computational node. The chief attribute of DD is its ability to divide a given solution domain into a form that can exploit the MIMD parallel architecture. A speed-up directly proportional to the number of processors is theoretically possible.

Unfortunately, a MIMD type parallel computer was not available for this study. It is possible, however, to simulate a parallel calculation on a serial computer. Internal parallel computer workings such as propagation delays and memory structure cannot be evaluated. However, a simulation allows a clear view of the parallel algorithm independent of a

specific parallel architecture. The disadvantage of the parallel simulation is that subdomain calculation overlap is not accurately modeled.

Computation load is not always even, but there might be situations where an uneven load distribution would assist convergence. Figure 3.5 shows Gantt charts of a hypothetical four domain configuration. It points out the differences between parallel computer, serial computer and parallel simulation calculation timings.

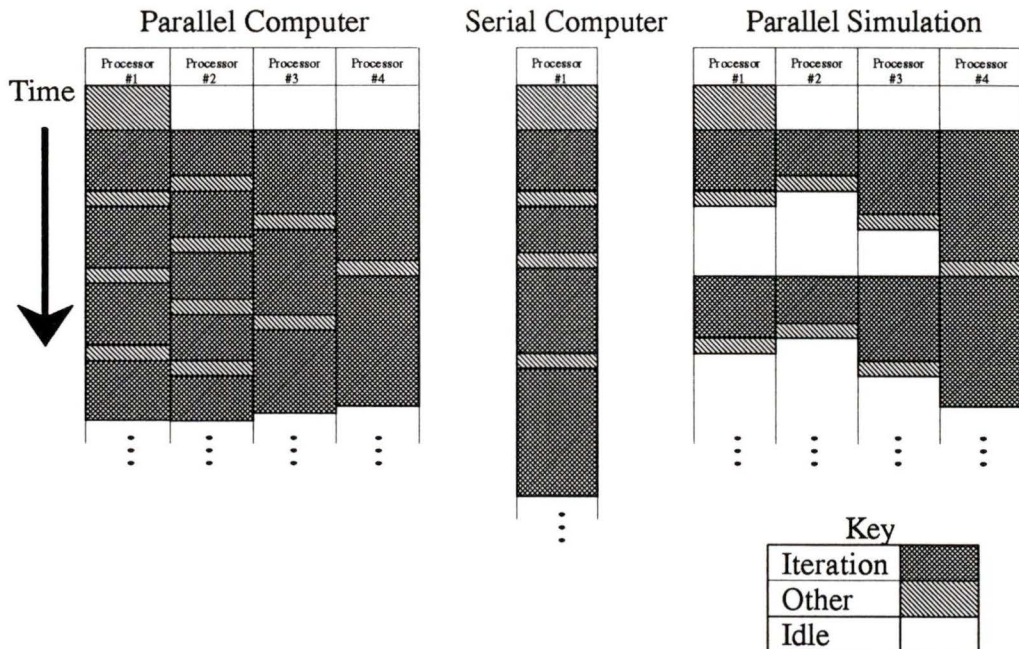


Figure 3.5: Example Gantt charts for a parallel computer, a serial computer and a parallel simulation.

The parallel simulation adds idle time to the faster subdomains resulting in conservative parallel efficiency estimations. The calculation of idle time for individual subdomains is facilitated through the assumption that the processing time of a domain is proportional to

the square of the number of nodes in that domain. The proportional constant is derived from the test case run and used to estimate the CPU time of the largest subdomain.

Iteration cycle modifications add an additional level of complexity to the parallel efficiency calculation. The repeated subdomain calculation must take place after the other subdomains have completed an iteration. To account for this, the CPU time of the largest subdomain and the time taken by the repeated subdomain are added. In an actual parallel computer implementation the repeated processes can be made to overlap, thus eliminating idle time. This is described graphically in figure 3.5. If the subdomain on processor 2 is critical to the calculation, its repeated calculation could speed convergence. This effect cannot be simulated in serial. Timing of subdomain calculations becomes less important for even subdomain load distributions.

Assuming no parallel overhead, parallel speedup and parallel efficiency are defined as

$$\epsilon_{su} = \frac{\text{Single Domain CPU Time} \cdot (n_d)}{\text{Multi - Domain CPU Time}}, \quad (3.1)$$

$$\epsilon_e = \frac{\text{Single Domain CPU Time}}{\text{Multi - Domain CPU Time}} \cdot 100\%. \quad (3.2)$$

The same computer was used for all test runs so that CPU timings as well as number of iterations could be compared. All timings are based on CPU time taken for residuals to converge to  $1.0 \times 10^{-3}$ .

### 3.4 Testing Accuracy

Accuracy of the DD solutions is evaluated by a direct comparison with a single domain solution. The single domain solution, or benchmark, and the DD test cases use identical grid spacing so that velocity and pressure values can be compared at each node without interpolation.

### 3.5 Memory Requirements

Applying DD with a serial computer affords a saving of memory requirements. Memory savings are gained by the reduction of temporary matrices from the size of a full domain to the size of a subdomain. A memory model was constructed for the DD solution procedure outlined in section 3.1. In the model it is assumed that the temporary array size will be equivalent to the size of the largest subdomain. The amount of memory required is calculated by categorizing all program variables into eight groups, based on their size dependencies. For example, all  $x$  direction vectors that are the same length as the  $x$ -axis of a subdomain are grouped together. In this manner the size of each group can be calculated for given domain and subdomain sizes. Appendix C lists the variables used and their size. The number of subdomains needed for a given domain is calculated from the subdomain size. A three node overlap is assumed. The total memory requirements for each subdomain configuration is compared to the memory used for a single domain implementation. The task for the user is to find the subdomain size that minimizes memory requirements. Table 3.1 shows a memory analysis of an 80x50 node domain. Several subdomain configurations are applied with varying degrees of memory savings. The optimum configuration, eight subdomains, results in a memory saving of 30% over the single domain solution.

Figure 3.6 shows a contour plot of memory usage for all possible subdomain sizes. The plot shows that the optimum subdomain sizes are located in a relatively small region. Larger domains were found to produce larger reduction in memory requirements.

It should be pointed out that an optimum domain decomposition pattern from the point of view of memory savings is not necessarily optimum for the point of view of convergence rate. This issue is explained in the next chapter.

Table 3.1: Spread sheet memory model of 80x50 node domain.

<b>Memory Model for Domain Decomposition</b>									
<b>Domain Description</b>	Original	Case #1	Case #2	Case #3	Case #4	Case #5	Case #6	Case #7	Optimum
X direction cells	80	80	42	80	42	29	42	29	22
Y direction cells	50	50	50	27	27	27	18	18	27
Number of domains	1	1	2	2	4	6	8	12	8
<b>Memory Allocation</b>									
Solution Matrices	32000	32000	33600	34560	36288	37584	48384	50112	38016
Permanent X vectors	800	800	840	1600	1680	1740	3360	3480	1760
Permanent Y vectors	600	600	1200	648	1296	1944	1728	2592	2592
Grid description	4	4	8	8	16	24	32	48	32
Local matrices	40000	40000	21000	21600	11340	7830	7560	5220	5940
X-direction vectors	160	160	84	160	84	58	84	58	44
Y-direction vectors	100	100	100	54	54	54	36	36	54
Fixed length variables	390	2960	2960	2960	2960	2960	2960	2960	2960
Memory ( Megabytes)	0.58	0.60	0.47	0.48	0.42	0.41	0.50	0.50	0.40
Percent of 1 domain mem.	<b>100.00</b>	<b>103.47</b>	<b>80.74</b>	<b>83.17</b>	<b>72.54</b>	<b>70.48</b>	<b>86.62</b>	<b>87.11</b>	<b>69.41</b>

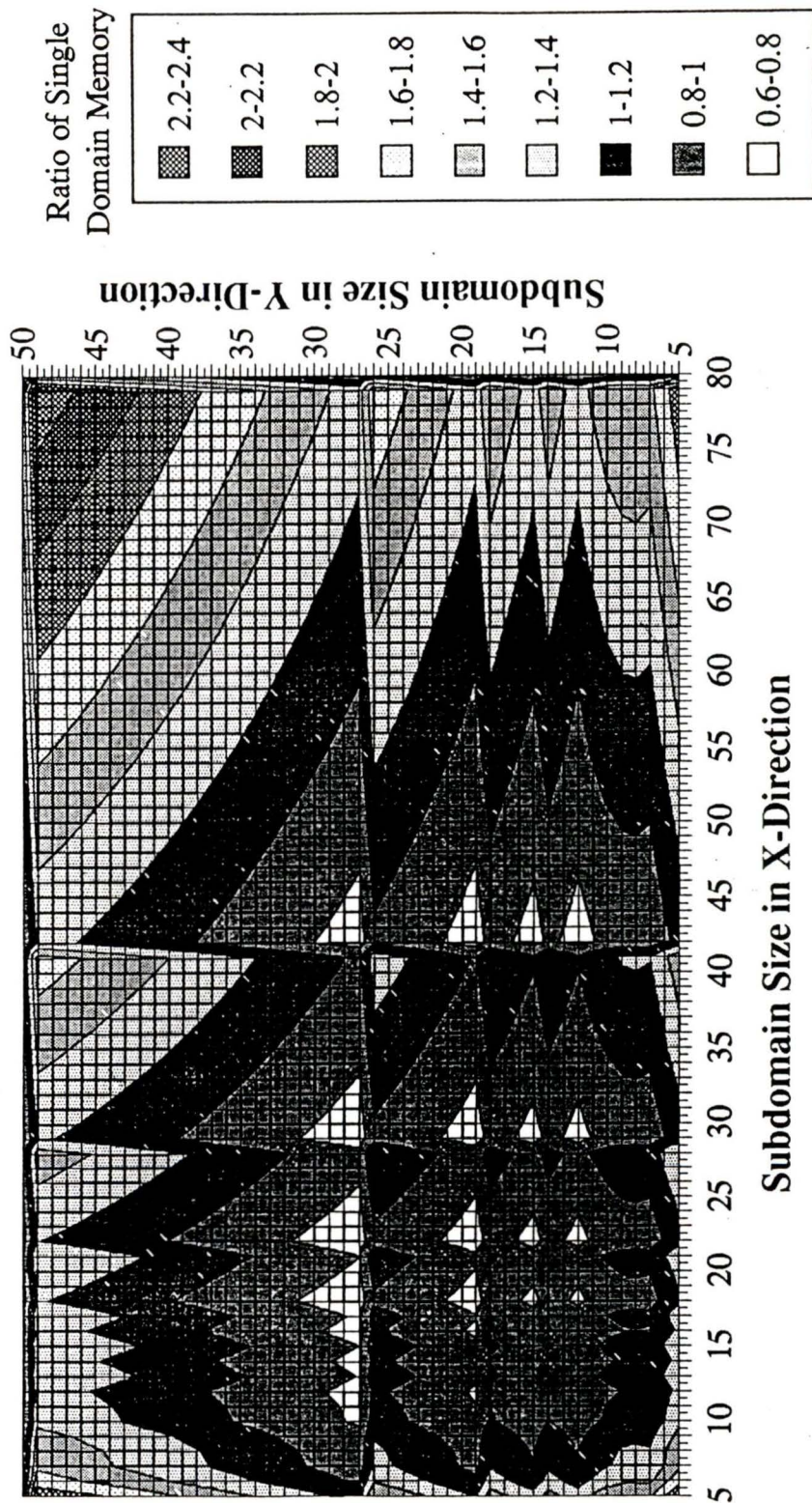


Figure 3.6: Contour plot of memory usage with a DD implementation of a 80x50 node domain.

# Chapter 4

## Numerical Verification

### 4.0 Procedure

Accuracy and parallel efficiency of the domain decomposition method were evaluated by the comparison to single domain solutions. Two test cases were used, developing flow between parallel plates and flow over a low blockage ratio rib. The parallel plate case is a well documented problem with relatively uniform gradients throughout the domain, and, therefore, well suited for initial testing and evaluation. The surface mounted low blockage ratio rib, with its complex flowfield, is a more stringent test of DD accuracy and performance. Several subdomain configurations were investigated on each test case to allow a comprehensive evaluation of the DD method.

### 4.1 Developing Flow Between Parallel Plates

A two-dimensional domain was used to model flow between a pair of semi-infinite parallel plates. See figure 4.1. The distance between the plates,  $h$ , was used as the characteristic

length scale. The channel width is  $h$  and its length is  $12.5h$ . Data was compiled for a benchmark single domain case, a two domain case with a vertical interface, and a two domain case with a horizontal interface. The validity of the benchmark solution was evaluated by comparing its results to published data. The DD cases were evaluated by comparing their solutions to the benchmark.

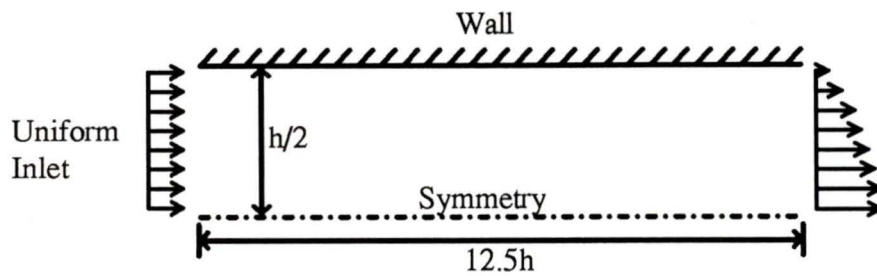


Figure 4.1: Schematic of flow domain.

### 4.1.1 Grid Refinement Study

To assess grid independence, a grid refinement study was conducted using development length, defined here as the distance from the entrance to the location where the center line velocity reaches 99% of the fully developed analytic solution. The dimensionless development length is normalized with channel width. The study was conducted at a Reynolds number,  $Re = \frac{U_\infty \cdot h}{\nu}$ , of 100. A uniform inlet velocity profile was used. Table 4.1 lists the various grid refinements examined and their corresponding development length. In the refinement study, both the number of nodes and the grid expansion factors,

$E_x = \frac{\Delta x_{i+1}}{\Delta x_i}$  and  $E_y = \frac{\Delta y_{j+1}}{\Delta y_j}$ , were varied on each axis. An expansion factor equal to 1.0

corresponds to a uniform grid and values greater and less than 1.0 correspond to expansion and contraction, respectively.

Table 4.1: Grid refinement study results.

X Nodes	Expansion Factor	Y Nodes	Expansion Factor	Development Length
50	1.02	40	.999	4.925
60	1.02	40	.999	4.884
70	1.02	40	.999	4.877
80	1.02	40	.999	4.878
80	1.001	40	.999	4.901
80	1.03	40	.999	4.880
80	1.05	40	.999	4.877
80	1.05	40	.98	4.884
80	1.05	40	.95	4.911
80	1.05	50	.999	4.873
80	1.05	50	.98	4.870
80	1.05	50	.95	4.905
80	1.05	60	.999	4.861
80	1.05	60	.98	4.863

Grid independence was assessed by monitoring the relative change in development length between successive grid refinements. An essentially grid independent solution was obtained with a grid of 60x40 nodes with an  $x$ -expansion factor  $E_x=1.02$  and a uniform  $y$  grid. The overall trend indicated that as the grid was refined, development length was reduced. It is thought that a uniform  $y$  grid was best because the entrance development zone extends across the full width of the entrance. In most boundary layer dominated flows,  $y$ -direction refinement is concentrated at the wall.

The convergence criterion was defined as a maximum normalized residual less than  $1.0 \times 10^{-4}$ . This value was determined by monitoring the development length during

convergence; changes in dimensionless development length between iterations were on the order of  $1.0 \times 10^{-4}$ .

### 4.1.2 Flow Features

The flow development process is shown schematically in figure 4.2. Fluid velocity at the entrance is uniform, but as the flow progresses, boundary layers are formed at the walls. Growth of the boundary layers results, effectively, in a displacement of the streamlines away from the walls and an acceleration of the core flow. When opposite wall's boundary layers meet, the flow is considered fully developed, and the velocity gradients in the streamwise direction vanish.

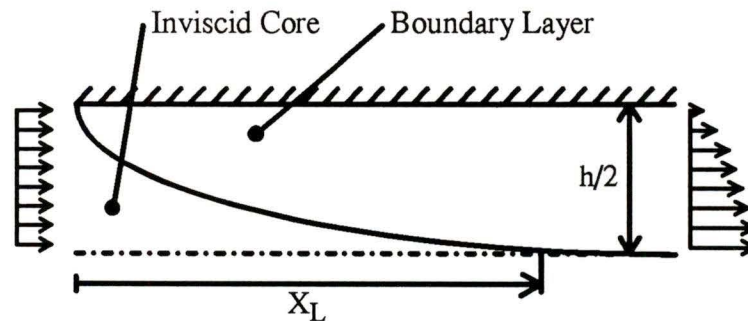


Figure 4.2: Flow development process showing boundary layer core interaction.

The development region is characterized by large values of wall shear stress which decrease exponentially to a constant value of 0.120, attained when the flow becomes fully developed. The computed value is identical to the theoretical value. The theoretical fully developed velocity profile and wall shear calculations can be found in Appendix D.

Although an exact theoretical value for the development length is not available, a numerical study by Schmidt and Zeldin presented by White [15] indicates that the development length for parallel plates at  $Re_h=100$  is approximately  $4.8h$ . Atkinson *et al* [14] produced a correlation based on a linear combination of creeping flow and boundary layer type solutions.

$$X_L = 0.3125 + 0.044 \cdot Re_h \quad (4.1)$$

A development length of  $4.71h$  is obtained using this correlation for  $Re_h=100$ . The development length produced with the refined grid single domain solution was  $4.89h$ ;  $3.65\%$  longer than the value suggested by Atkinson *et al* [14] and  $1.88\%$  longer than the value suggested in White [15].

A velocity overshoot was found in the developing flow region. See figure 4.3. It occurs at the interface between the boundary layer and the core and extends from the entrance to  $1.2h$ . The overshoot has a maximum magnitude of  $107.4\%$  of the core velocity occurring at  $0.18h$  from the entrance and  $0.34h$  from the walls. The overshoot phenomenon was interpreted by Shah and London [14]: In the entrance region, large pressure gradients are immediately formed at the wall to meet the no slip boundary condition. However, the effects of these pressure gradients do not reach the uniform core immediately. The result is that the core does not accelerate fast enough to meet continuity so an overshoot is formed to compensate. It is worth noting that solutions obtained using the boundary layer equations fail to reproduce this overshoot phenomenon.

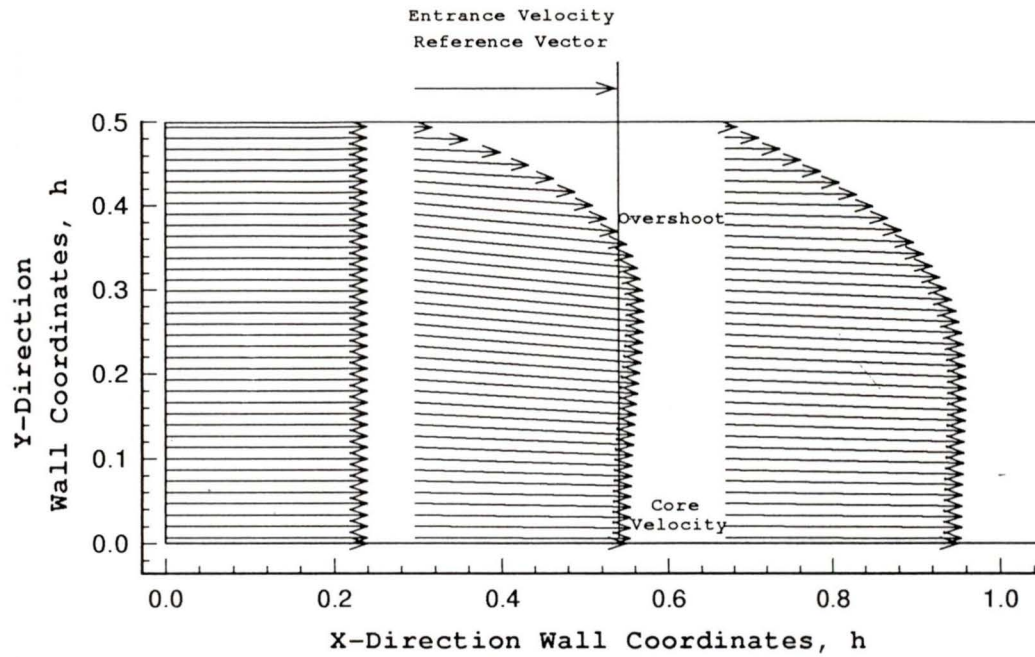


Figure 4.3: Velocity overshoot predicted in the development region of parallel plate flow.

### 4.1.3 Domain Decomposition

A domain decomposition implementation of the parallel plate problem was set-up with a vertical interface as illustrated in figure 4.4. The interface is located at the middle grid line. Note that since non-uniform grid spacing is used, this does not correspond to the midpoint of the domain. The interface has a physical location of approximately  $4.5h$ .

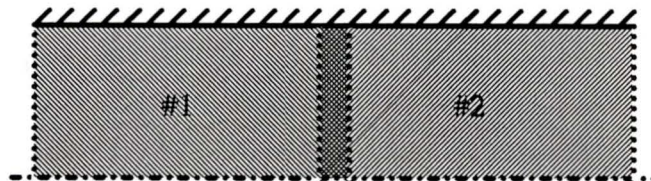


Figure 4.4: Domain layout for vertical interface of parallel plate case.

The development length predicted was  $4.76h$ , 2.5% shorter than the single domain solution, but only 1.0% longer than the value of Atkinson *et al* [14]. The calculated wall shear stress distribution is nearly identical to the benchmark values. The fully developed shear stress coefficient predicted was 0.120, identical to the theoretical value. Figure 4.5 shows a plot of wall shear stress coefficient for the parallel plate flow test case predicted using the single domain and the DD solutions.

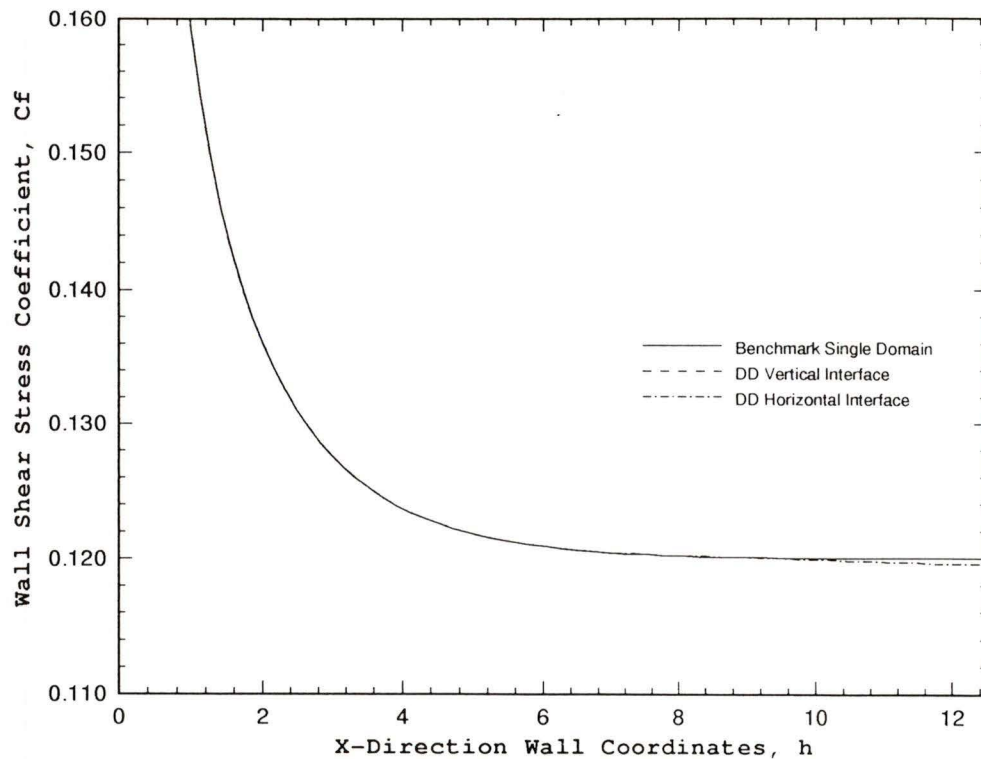


Figure 4.5: Wall shear stress distribution for the parallel plate test cases.

Table 4.2 itemizes the optimum relaxation factors and convergence time for the vertical interface solution. Adding interface over relaxation greatly improves the speed of convergence. In this case, the two subdomain solution converges faster than the single domain solution.

Table 4.2: Optimum relaxation factors and convergence times for parallel plate test cases.

	Interface ORFs		Solution URFs			Convergence	
	u	v	u	v	p	Iterations	CPU Time
Single domain (benchmark)	na	na	0.74	0.48	0.50	509	200 s
2 Domain Vertical Interface	1.65	1.45	0.75	0.48	0.50	331	130 s
2 Domain Horizontal Interface	1.20	1.87	0.76	0.48	0.49	1114	422 s

Figure 4.6, 4.7 and 4.8 show contour plots of the u-velocity, v-velocity, and pressure differences between the single domain and two subdomain vertical interface solutions. Differences are normalized with the appropriate parameters. The maximum difference is of the order  $1.0 \times 10^{-4}$ .

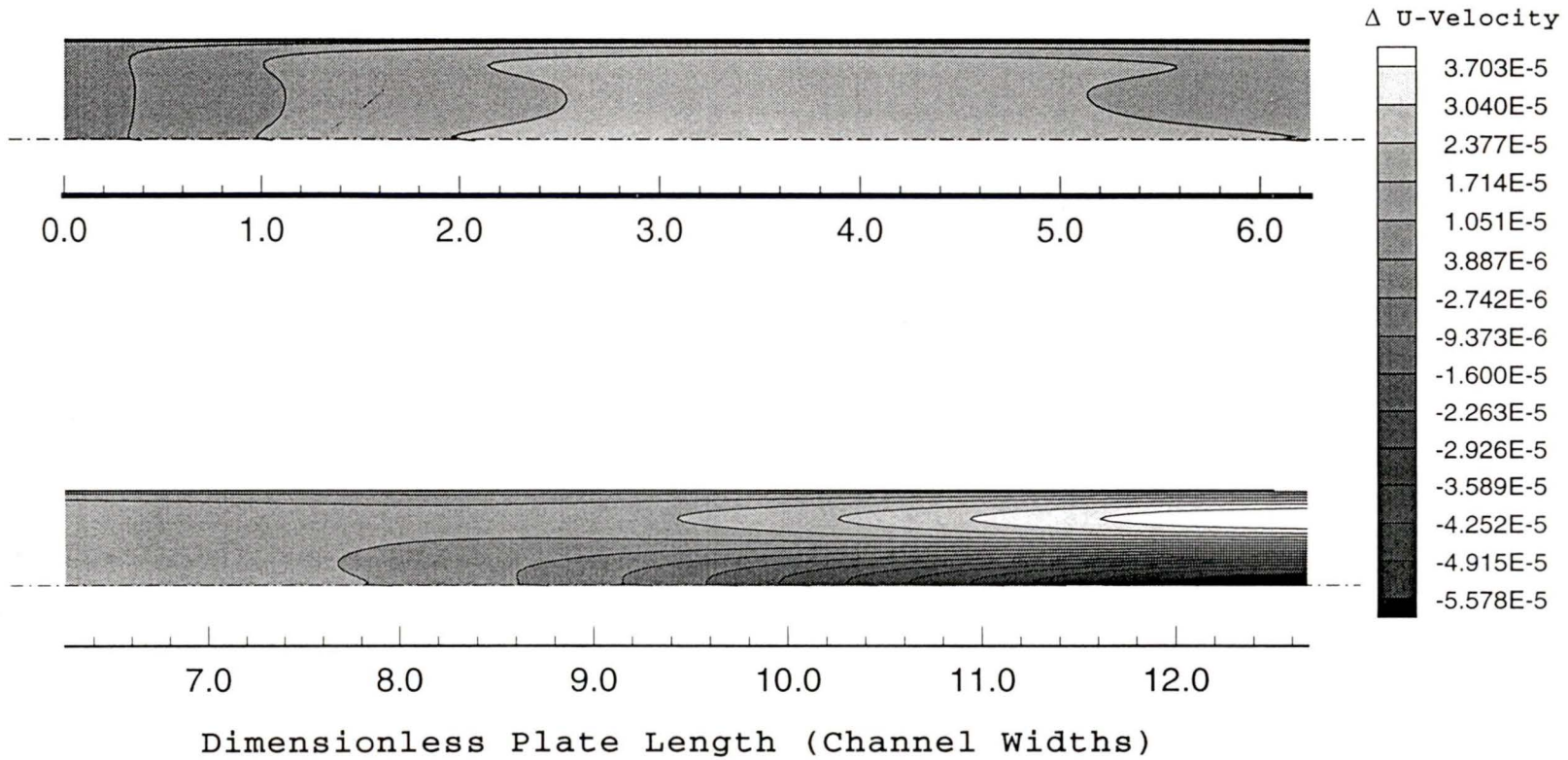


Figure 4.6: U-velocity non-dimensional difference contours for the vertical interface parallel

plate test case. Velocity made dimensionless with  $\Delta U = \frac{U_{DD} - U_{\text{Benchmark}}}{U_{\infty}}$

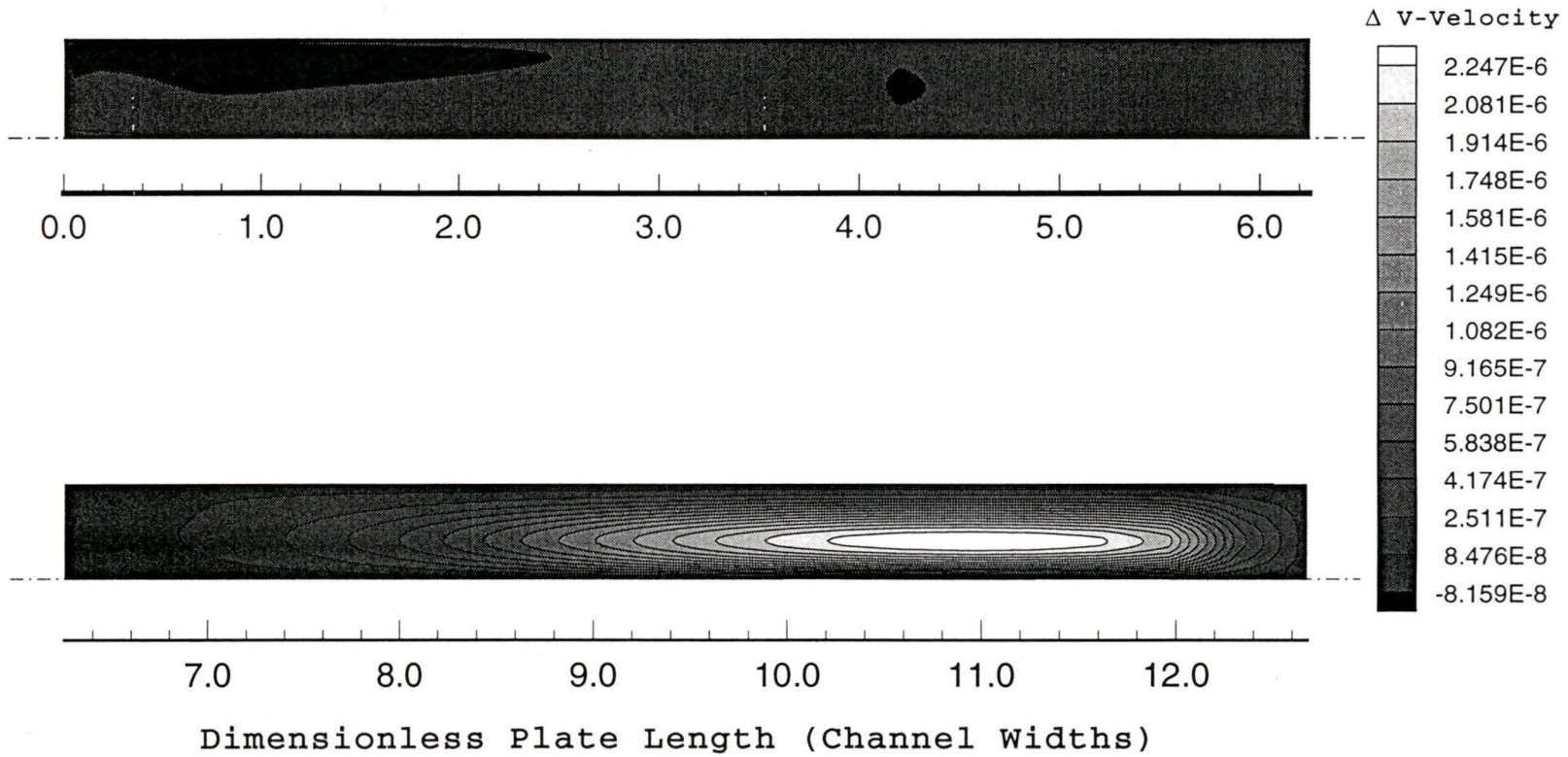


Figure 4.7: V-velocity non-dimensional difference contours for the vertical interface parallel

plate test case. Velocity made dimensionless with  $\Delta V = \frac{V_{DD} - V_{\text{Benchmark}}}{U_{\infty}}$

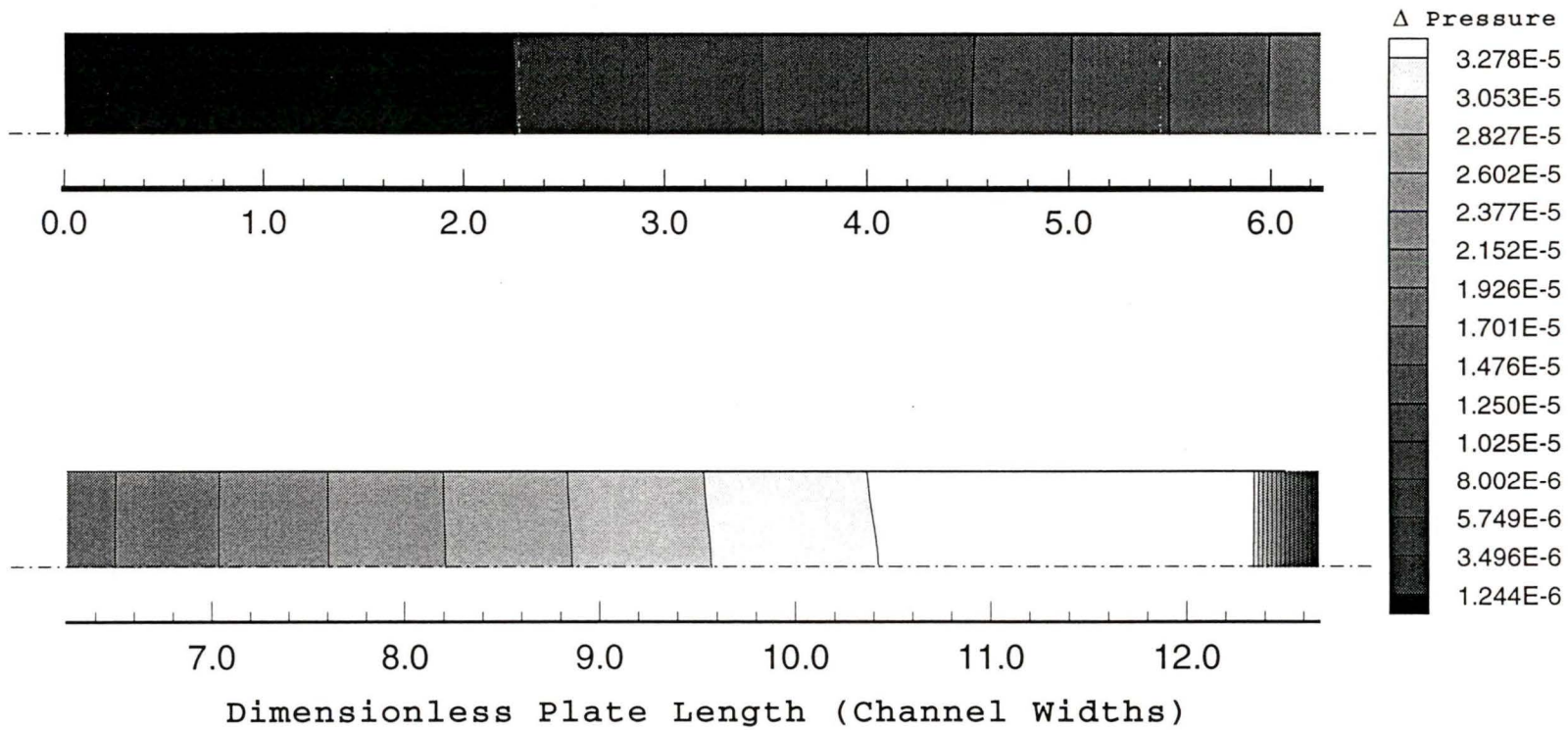


Figure 4.8: Non-dimensional pressure difference contours for the vertical interface parallel

plate test case. Pressure made dimensionless with  $\Delta P = \frac{P_{DD} - P_{Benchmark}}{\frac{1}{2} \rho U_{\infty}^2}$

A second two domain test case was constructed employing a horizontal interface. The domain was divided into two subdomains along the grid mid-point which is also the physical midpoint, as shown in figure 4.9.

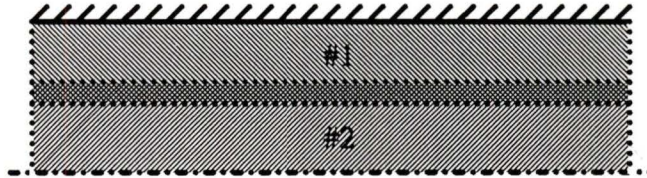


Figure 4.9: Subdomain layout for horizontal interface of parallel plate case.

The development length predicted was  $4.89h$ , identical to the single domain value. The wall shear stress distributions followed the benchmark values, except near the exit. The fully developed wall shear stress coefficient predicted was  $0.1196$ ,  $0.33\%$  lower than the theoretical value, as shown in figure 4.5.

Table 4.2 itemizes the optimum relaxation factors and convergence time for the horizontal interface solution. In this case, the two domain solution converges significantly more slowly than the single domain solution.

Figures 4.10, 4.11, and 4.12 show contour plots of the  $u$ -velocity,  $v$ -velocity, and pressure differences between the benchmark and two subdomain horizontal interface solutions. The maximum difference is of the order  $1.0 \times 10^{-3}$ .

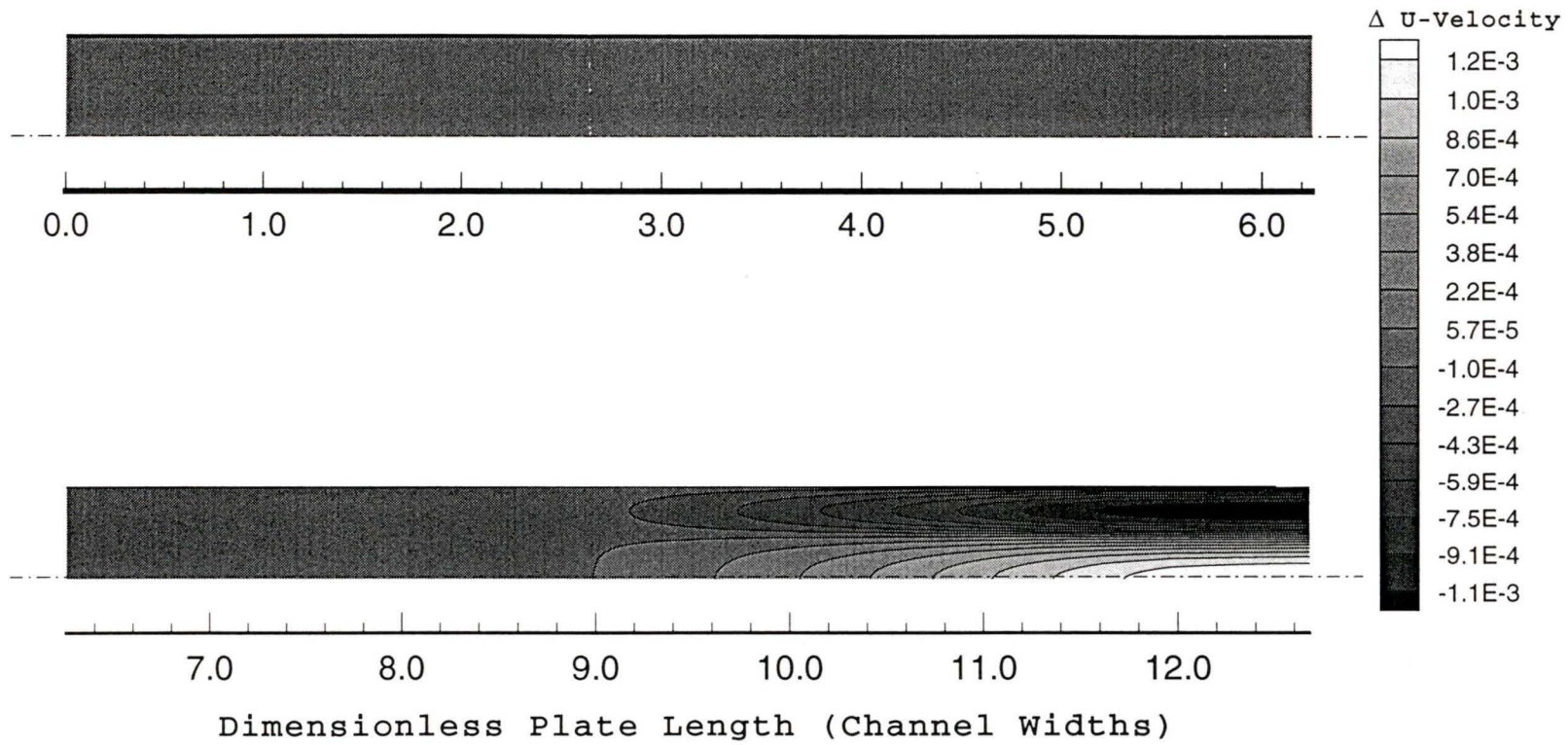


Figure 4.10: U-velocity non-dimensional difference contours for the horizontal interface parallel plate test case. Velocity made dimensionless with  $\Delta U = \frac{U_{DD} - U_{Benchmark}}{U_{\infty}}$

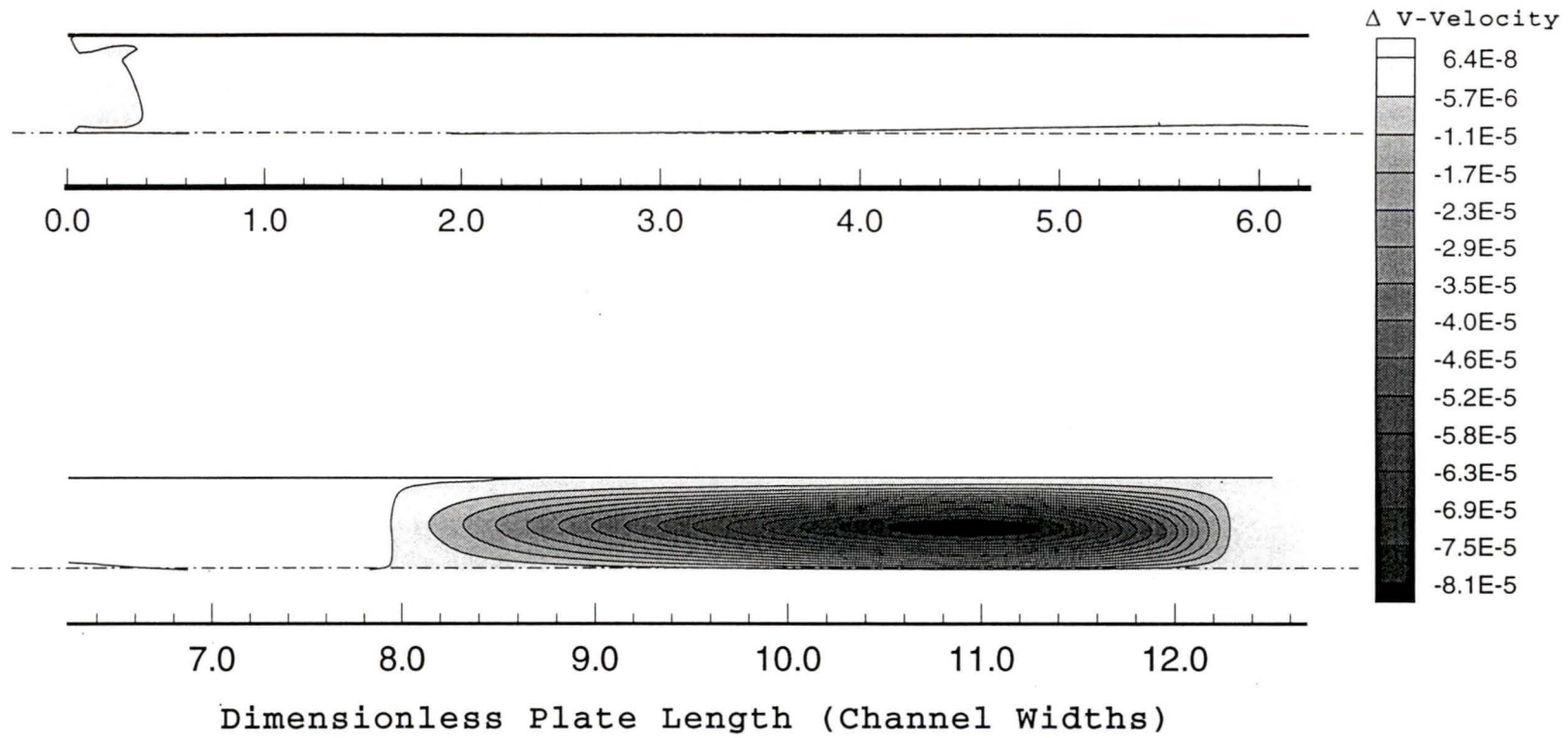


Figure 4.11: V-velocity non-dimensional difference contours for the horizontal interface parallel plate test case. Velocity made dimensionless with  $\Delta V = \frac{V_{DD} - V_{\text{Benchmark}}}{U_{\infty}}$

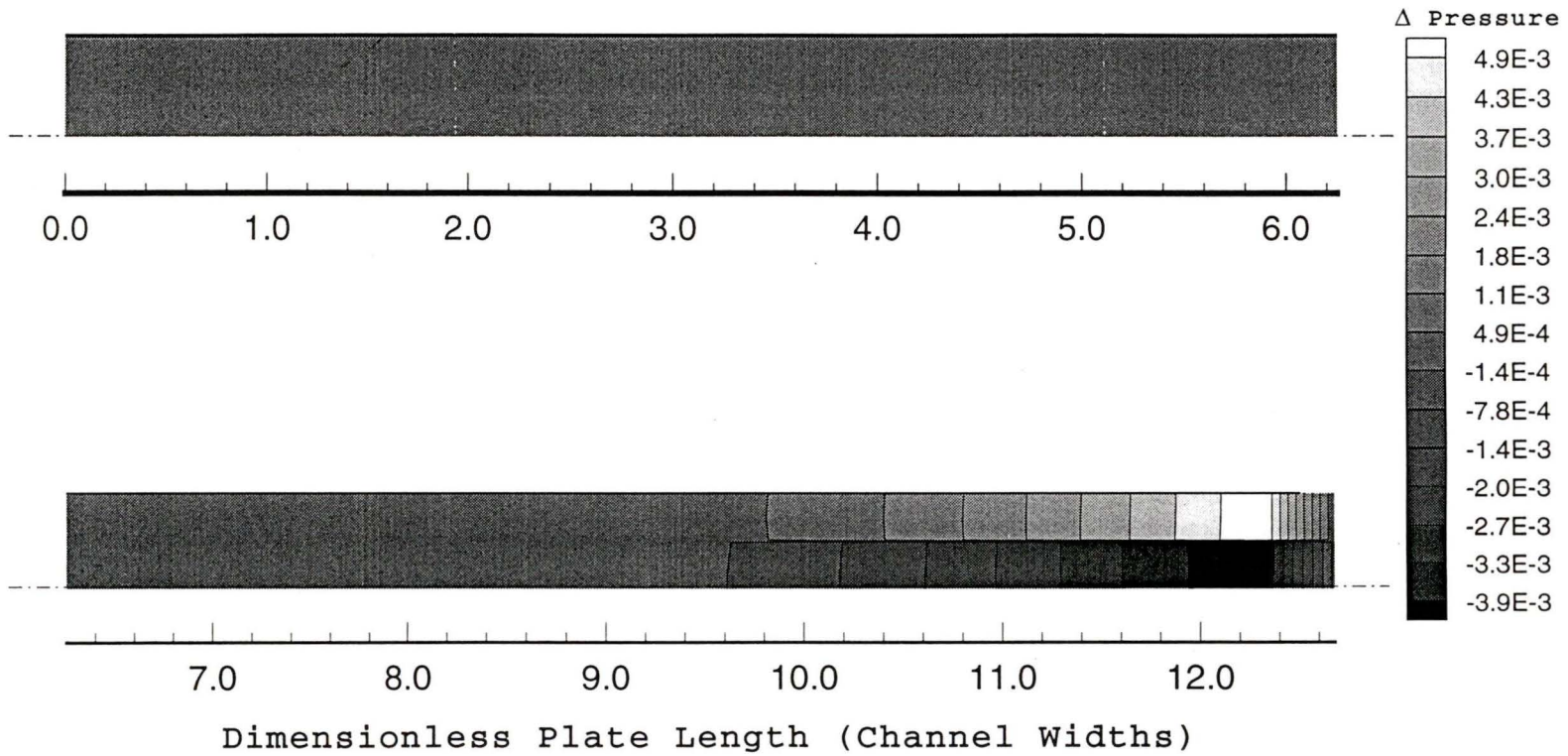


Figure 4.12: Non-dimensional pressure difference contours for the horizontal interface parallel

plate test case. Pressure made dimensionless with  $\Delta P = \frac{P_{DD} - P_{\text{Benchmark}}}{\frac{1}{2}\rho U_{\infty}^2}$

#### 4.1.4 Domain Decomposition Evaluation

In both DD parallel plate test cases the largest differences in  $u$  and  $v$ -velocity occur in the region of fully developed flow. The entrance region has smaller differences although it is an area of large gradients. The interface region is not an area of significant difference. Subdomain continuity enforcement was not required to achieve convergence for the vertical interface case but it improved convergence speed. For the horizontal case, continuity enforcement was necessary to attain a converged solution. The continuity enforcement procedure consists of correcting the velocities along an arbitrary subdomain interface after each iteration by adding or subtracting a constant value in such a way that the net mass flux out of a given subdomain remains zero.

In the horizontal interface test case, the maximum difference was an order of magnitude larger than in the vertical case indicating a lower flowfield convergence rate. The  $u$  and  $v$ -velocity difference contours show that the largest differences occur in a fully developed flow region between  $8h$  and  $12.5h$ . Intuitively, it is surprising that the largest differences occur in this region rather than in the entrance length region where gradients are higher. A possible reason for the lower convergence of the exit region is the reduced effectiveness of the iterative solution procedure. When a horizontal interface is introduced, the unidirectional sweep method does not transmit the exit boundary conditions as rapidly across the domain. A second possible cause is the high cell aspect ratios, as high as 27.5 to 1, located near the exit of the domain.

To evaluate the convergence performance of each of the configurations, the under relaxation factors (URFs) of all three cases were optimized. It was found that the URFs of

the three test cases were nearly identical. This finding is useful in that the time consuming optimization process can be shortened or avoided entirely. The interface ORFs were also optimized. The convergence rate was found to be most sensitive to the velocity over relaxation factor perpendicular to the interface, while the other ORFs had a minimal influence.

The vertical interface case produced a speedup of 3.08 and a parallel efficiency of 154%. In this case, domain decomposition appears to exceed the maximum theoretically possible efficiency implied by Amdahl's Law<sup>3</sup>. However, it should be noted that the unidirectional sweep solution method, applied to a domain elongated in the  $x$ -direction, results in poor solver efficiency. By dividing the domain across the  $x$ -axis the aspect ratio is reduced, the exit boundary conditions can be passed more efficiently, and the efficiency of the iterative solution procedure is improved.

The horizontal interface test case had poorer performance. It produced a speedup of 0.95, and a parallel efficiency of 47%. This poor performance is a direct consequence of elongated solution subdomains.

Although the unidirectional solution method is inefficient for high aspect ratio domains it performs well for low aspect ratio domains. Most high aspect ratio flowfields can be divided into a number of low aspect ratio subdomains and solved efficiently. This fact highlights the usefulness of domain decomposition.

---

<sup>3</sup> Amdahl's Law implies that parallel efficiencies greater than 100% are not possible, if the serial benchmark is fully optimized.

## 4.2 Low Blockage Ratio Surface Mounted Rib

A two-dimensional domain was used to model flow over a surface mounted rib. See figure 4.13. All dimensions are normalized with respect to rib height,  $h$ . The domain length is  $50h$ , and its height is  $12h$ . The rib is located  $13.2h$  from the entrance. Computations were performed for the benchmark single domain case, a three domain case, and a four domain case. The validity of the benchmark solution was evaluated by comparing the results to published data; specifically, by comparing the length of the trailing recirculation bubble.

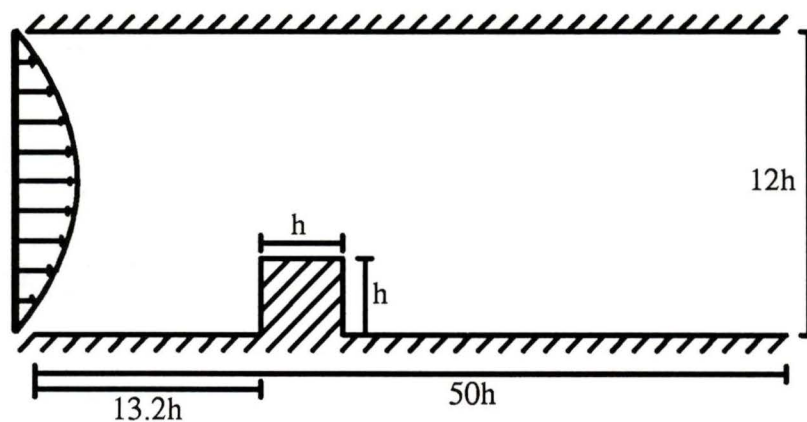


Figure 4.13: Schematic of surface mounted rib domain.

### 4.2.1 Grid Refinement Study

Since the length of the separation bubble,  $X_r$ , behind the rib is the most significant characteristic length scale for this type of flow; this reattachment length is often used as a measure of grid independence. In this case, refining the grid resulted in very little change in the reattachment length. Instead, wall shear stresses at the lower leading and upper

trailing rib corners were monitored at each level of grid refinement to measure grid sensitivity. The grid refinement study was conducted at a Reynolds number of 100 based on rib height with a fully developed channel flow inlet velocity profile. Figures 4.14 and 4.15 show the south wall shear stress for the various grid refinements. 50x70, 50x80 and 60x80 node grids produced differences in wall shear stress of less than 1% compared to the previous refinement level. On the basis of these findings, the 50x70 node grid was deemed to produce grid independent results; this grid is shown in figure 4.16.

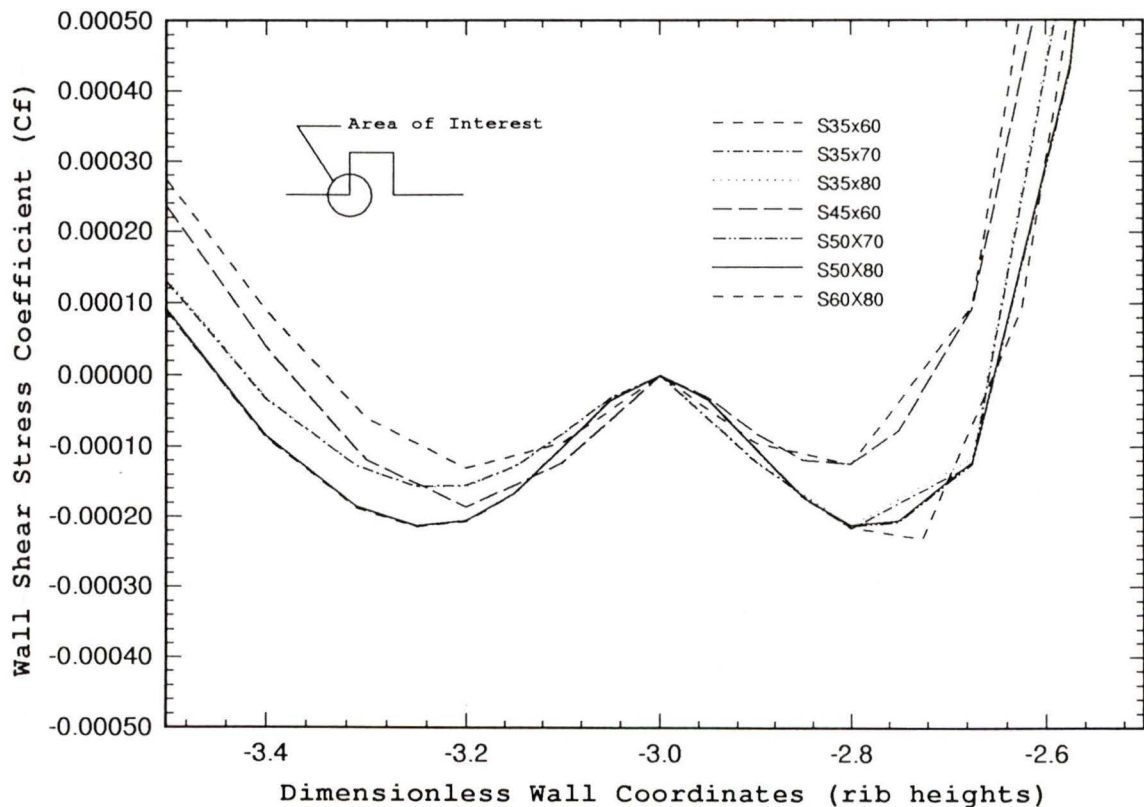


Figure 4.14: Wall shear stress in upstream recirculation region of rib flow. Origin of dimensionless wall coordinates is located at the downstream bottom corner of the rib.

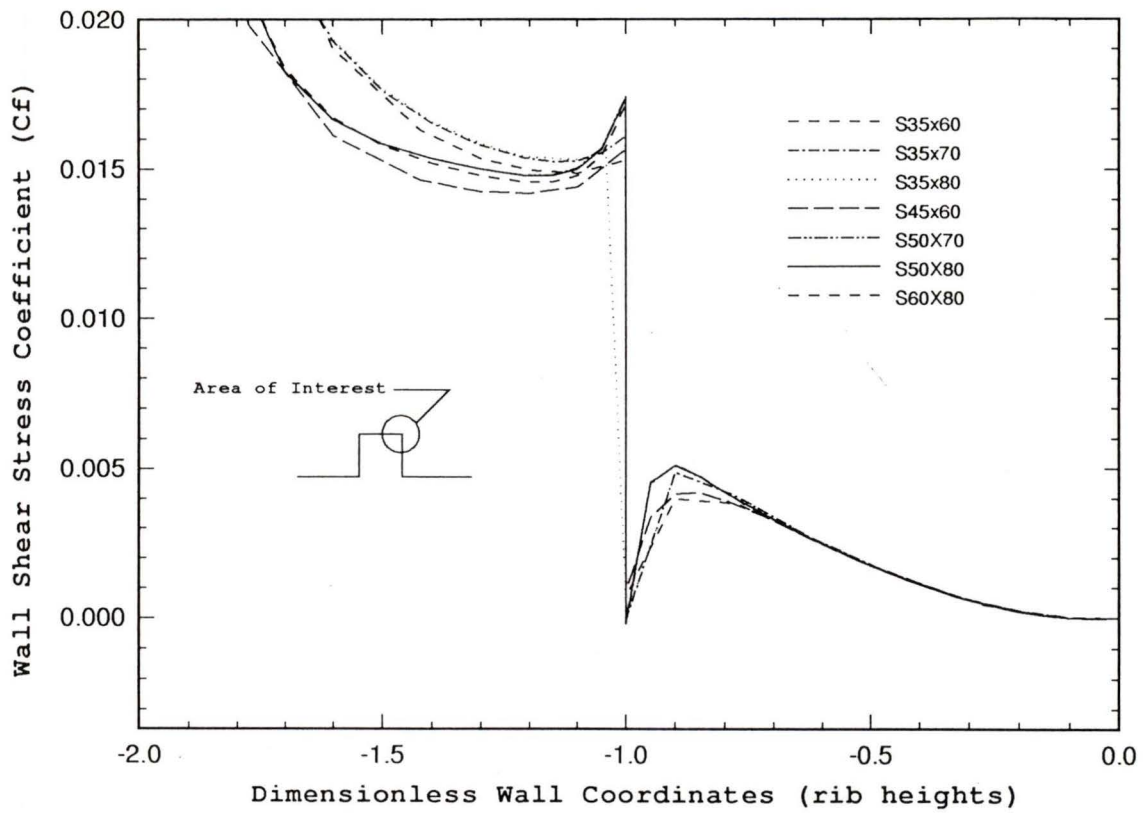


Figure 4.15: Wall shear stress at trailing upper rib corner.

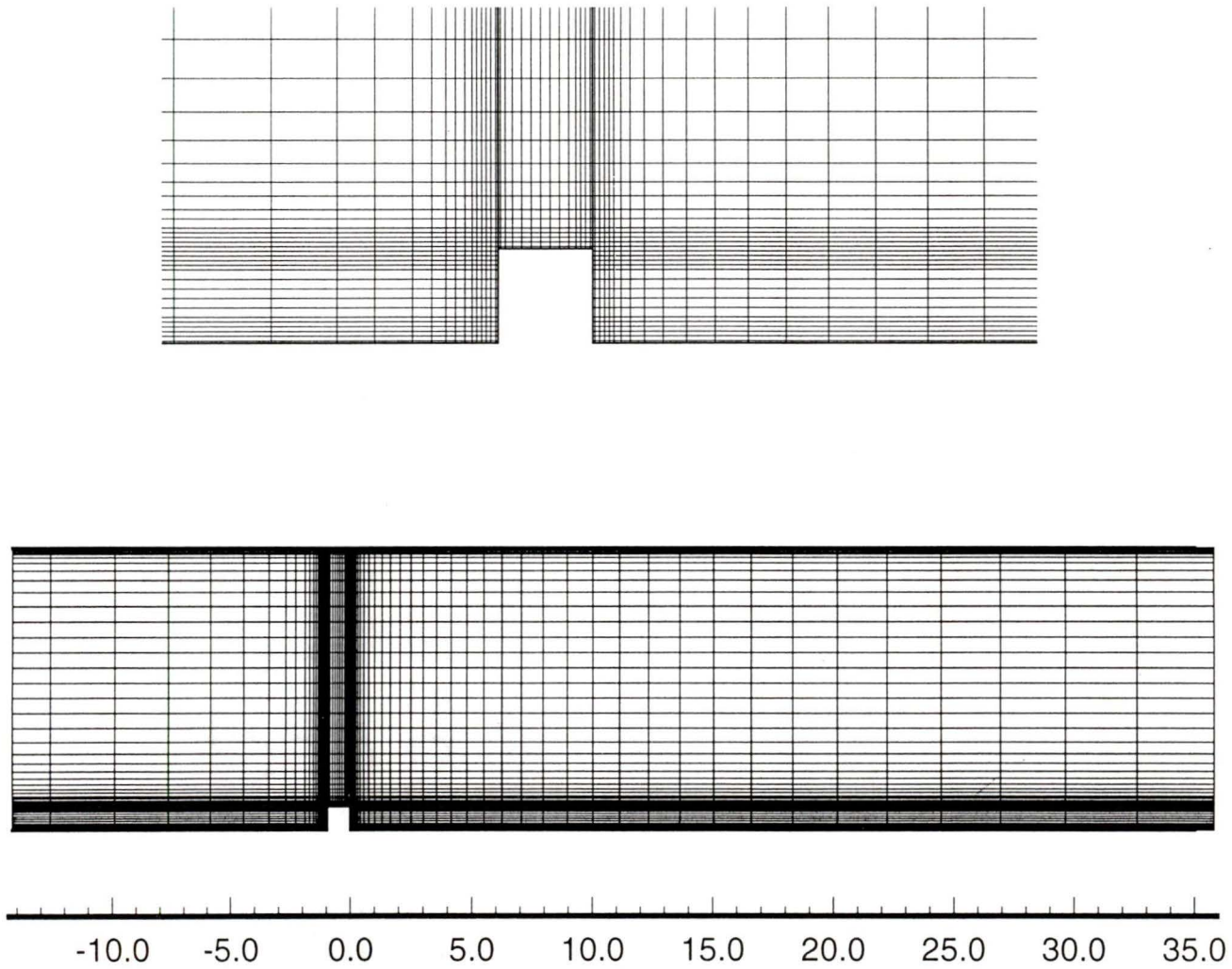


Figure 4.16: Refined grid used for rib flows with a magnified insert of grid near the rib.

The solution was also tested for entrance and exit boundary location independence by monitoring recirculation zone length for various boundary locations. An entrance length of  $13.2h$  and an overall length of  $50h$  were found to be sufficient for flow of  $Re=100$ .

The convergence criterion was defined as a maximum residual less than  $1.0 \times 10^{-4}$ . This value was determined by monitoring reattachment length during convergence. For this criterion, changes in dimensionless reattachment length,  $X_r/h$ , between iterations were on the order of  $1.0 \times 10^{-4}$ .

### 4.2.2 Flow Features

The flow features produced by the rib geometry are complex. Sharp rib corners result in strong local velocity and pressure gradients, and several recirculation zones are formed due to abrupt changes in geometry. Separation zones are measured by monitoring wall shear stress. The point of reattachment is defined as the location where wall shear stress vanishes. Three recirculation zone configurations that are common to surface mounted rib flow are shown in figure 4.17.

The type of pattern which develops depends on boundary layer thickness,  $\delta$ , of the upstream flow, channel blockage ratio and rib aspect ratio. Hong *et al* [16] conducted a numerical study that predicted type 1 flow occurring when the upstream boundary layer thickness is less than  $0.4h$  on the leading edge of the rib, while type 2 flows occur for  $\delta > 0.4h$ . Type 3 flows occur when  $\delta < 0.4h$  and the rib aspect ratio is less than 1. In the case being studied, type 2 flow was found because the rib aspect ratio is 1 and the boundary layer extends across the channel width.

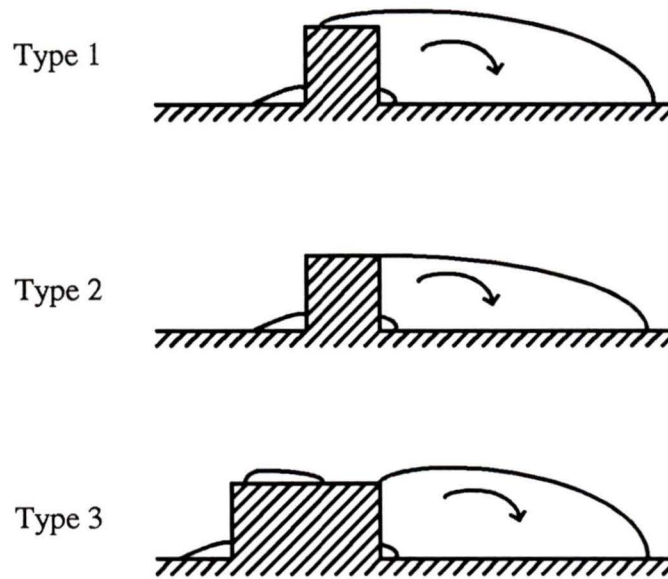


Figure 4.17: Common recirculation zone configurations for surface mounted rib flows.

Figure 4.18 is a plot of wall shear stress along the south surfaces. The wall shear stress takes the fully developed channel flow value of 0.005 at the entrance and returns to this value at the exit. The trailing recirculation zone is indicated by the area of negative shear stress extending behind the rib. Figure 4.19 is a close-up of the wall shear stress at the lower leading edge corner of the rib. Two negative shear stress zones indicate a small stagnation recirculation zone in front of the rib. This zone extends  $0.448h$  along the wall and  $0.347h$  up the rib. Figure 4.20 is a plot of wall shear stress on the three sides of the rib. Shear stress peaks at the leading edge corner of the rib and relaxes as a boundary layer is formed on top of the rib. The wall shear stress is discontinuous at the trailing edge rib corner as seen in figure 4.20. The discontinuity in shear stress is created by the boundary layer, formed on top of the rib, meeting the separation streamline of the trailing recirculation zone. Figure 4.21 shows a combination of streamlines and velocity vectors

around the rib. It also shows a close-up of the streamlines and velocity vectors near the rib. The stagnation recirculation zone in front of the rib and the small counter recirculation zone in the lower trailing edge corner can be seen. The most significant feature is the trailing recirculation zone with a length of  $8.58h$ . Experimental data for this test case are not available, but the reattachment length value observed here is within 14% of the experimental value given by Durst *et al* [28] for tandem ribs with a blockage ratio 3 times greater than the present case and a rib aspect ratio of 0.67. The effect of blockage and aspect ratio are examined in the next chapter.

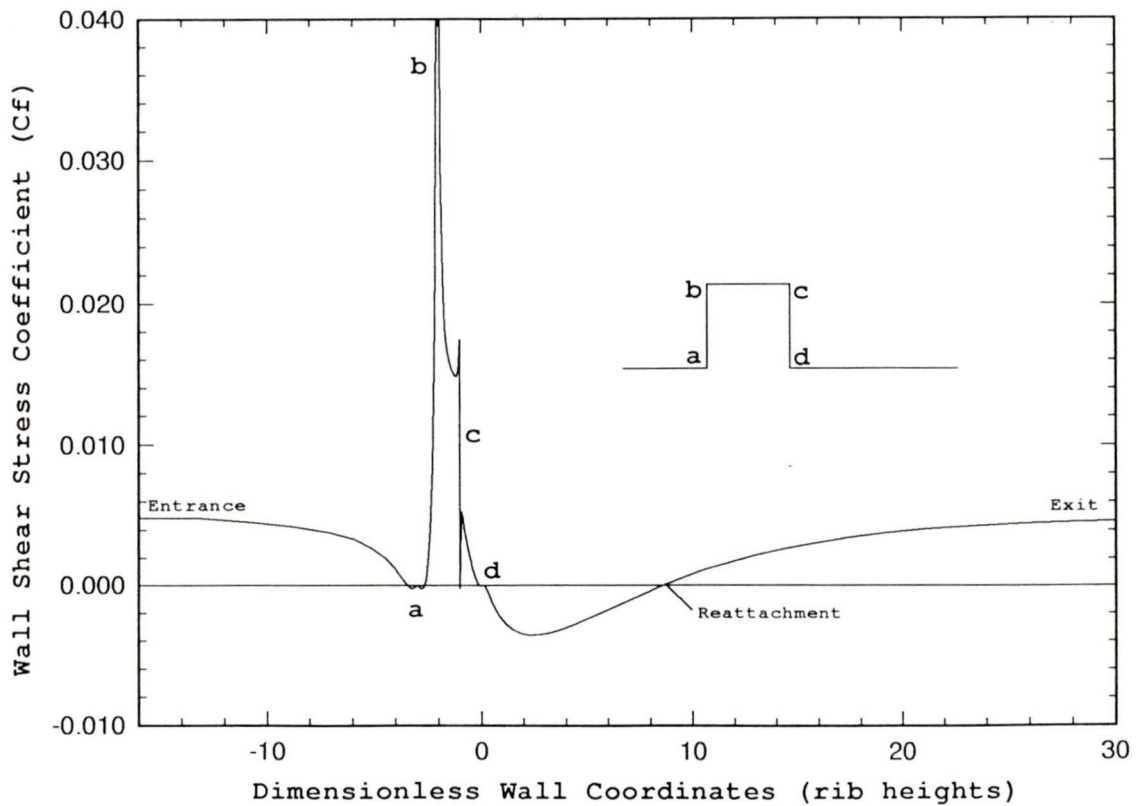


Figure 4.18: Plot of South wall shear stress across entire domain.

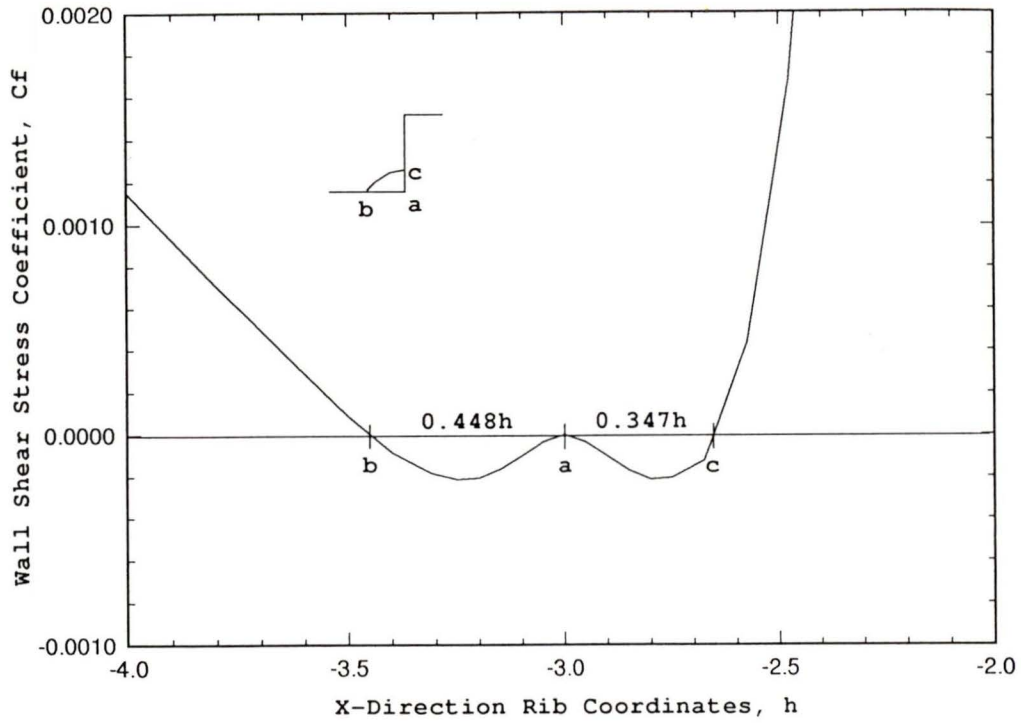


Figure 4.19: Lower leading edge rib corner wall shear stress.

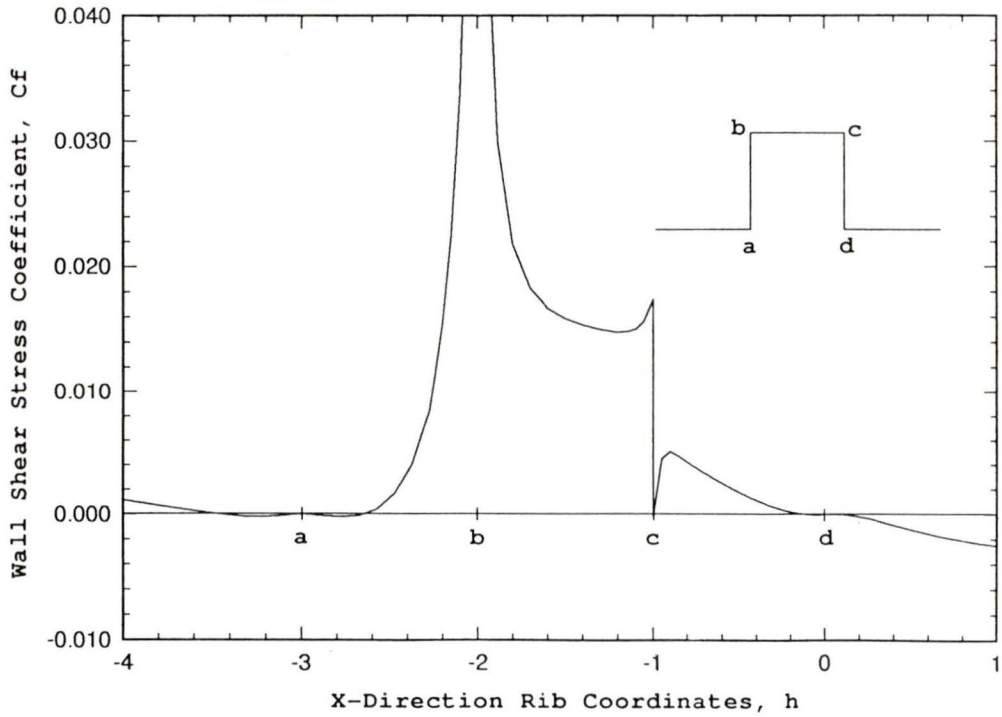


Figure 4.20: Wall shear stress over rib surface.

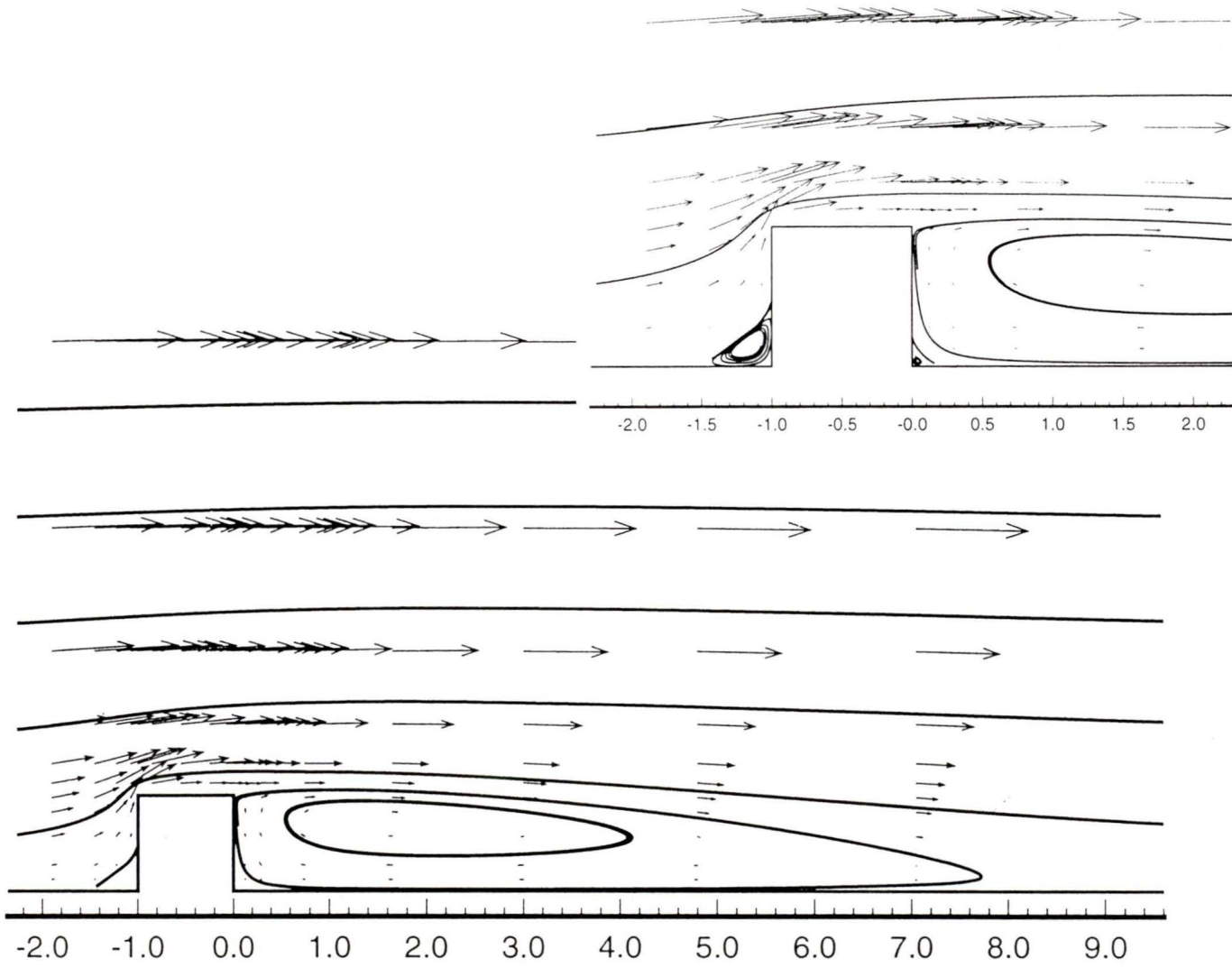


Figure 4.21: Plot of velocity vectors and streamlines for flow over a rib with an insert of flow near the rib

### 4.2.3 Domain Decomposition

The original single domain grid was divided into three subdomains to evaluate the domain decomposition process. A three node overlap, and a subdomain continuity boundary condition were implemented. Figure 4.22 shows the domain configuration and approximate interface locations.

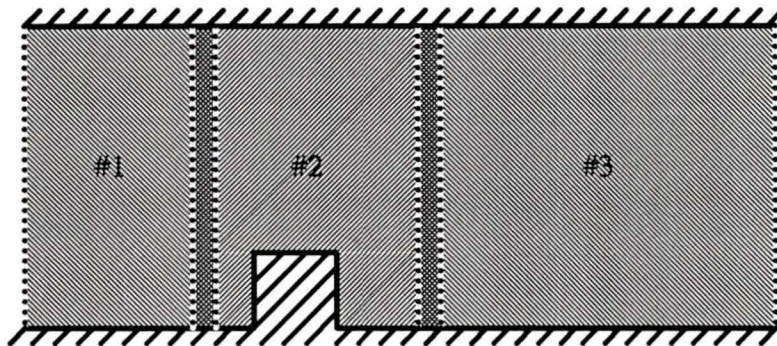


Figure 4.22: Subdomain layout for three domain surface mounted rib.

The reattachment length predicted was  $8.55h$ ; within 0.4% of the fully converged single domain solution. Optimum relaxation factors and convergence times are listed in Table 4.3. Figure 4.23 shows contour plots of the  $u$ -velocity,  $v$ -velocity, and pressure differences between the single domain and three subdomain solutions.

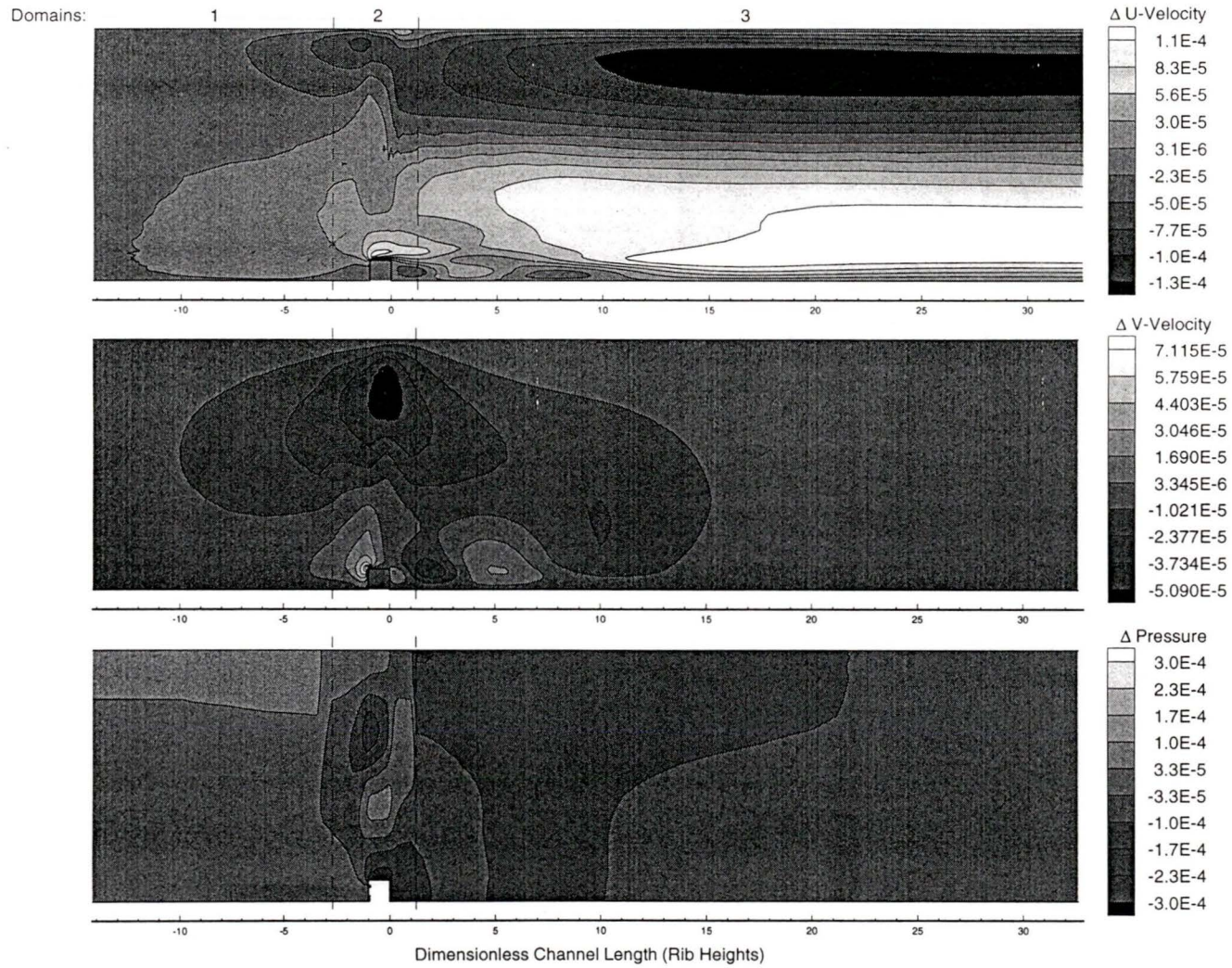


Figure 4.23: Contour plots of velocity and pressure difference for the three domain rib test case. Dashed lines correspond to domain interfaces. Values made dimensionless with functions mentioned previously

The location of the interfaces are shown with dashed lines. All differences are normalized with the appropriate values. The maximum difference is of the order  $1.0 \times 10^{-4}$ . The difference between the three and one domain solution is on the same order of magnitude as the maximum residual; therefore, for this test case, the domain decomposition method produces a converged flowfield.

A four domain test case was studied employing an additional horizontal interface above the rib. The rib domain was divided into four domains as shown in figure 4.24. A three node overlap and a subdomain continuity boundary condition were implemented. In addition, the domain containing the rib was calculated twice during each domain calculation cycle for the first 450 iterations.

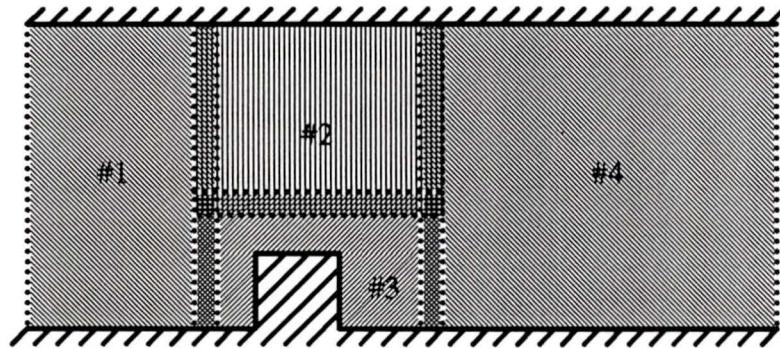


Figure 4.24: Domain layout for four domain rib case.

The development length predicted was  $8.02h$ , 6.6% shorter than the single domain value. It was found that this difference dropped to 0.3% if the residual was allowed to converge to  $1.0 \times 10^{-4}$ . Optimum relaxation factors and convergence times are listed in Table 4.3.

Two values of optimum interface over relaxation factors are noted for horizontal and vertical factors.

Table 4.3: Optimum relaxation factors and convergence times for rib test cases.

	Interface ORFs		Solution URFs			Convergence	
	u (h/v)	v (h/v)	u	v	p	Iterations	CPU Time
Single Domain	na	na	0.78	0.77	0.41	410	197 s
3 Domain Test Case	1.60	1.80	0.77	0.79	0.23	441	238 s
4 Domain Test Case	1.65/1.27	1.79/1.36	0.69	0.45	0.27	557	353 s

An iteration cycle modification was implemented on this case because the largest gradients are concentrated around the rib; the rib domain was calculated twice per iteration cycle. The pattern used was 1-2-3-3-4, but 1-2-3-4-3, 1-2-3-3-4-3, and 1-2-3-3-3-4 were tested. It was also found that the benefits of this procedure were maximized if, after a few hundred iterations, the pattern was returned to 1-2-3-4. The disadvantage of this procedure is that it tended to bias the solution of the doubled domain, resulting in the need for a stricter convergence criterion.

Figure 4.25 shows contour plots of the u-velocity, v-velocity, and pressure differences between the benchmark and four domain solutions. The maximum difference is of the order  $1.0 \times 10^{-4}$ .

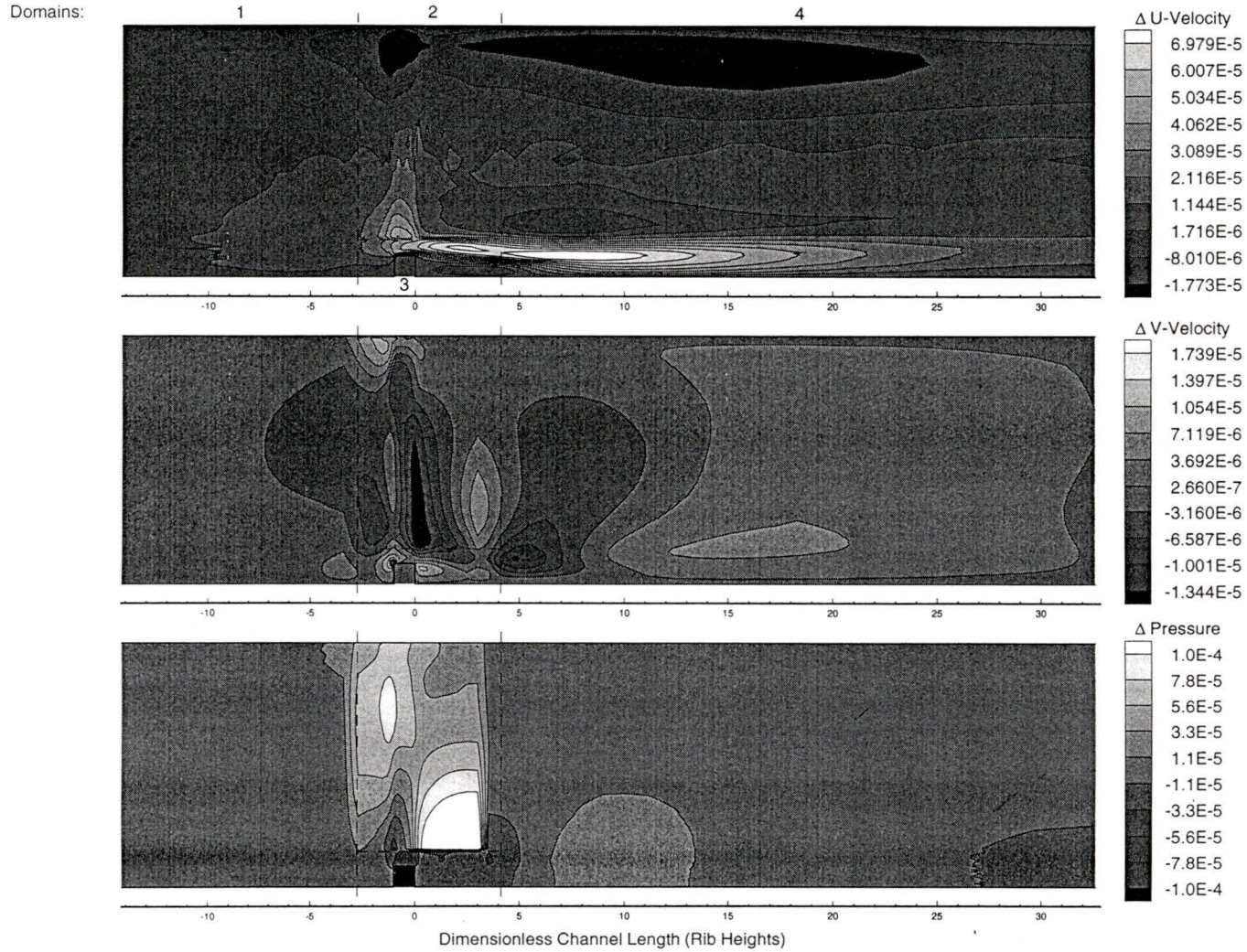


Figure 4.25: Contour plots of velocity and pressure differences for the four domain rib test case. Dashed lines correspond to domain interfaces

#### 4.2.4 Domain Decomposition Evaluation

In both the three and four domain cases an interface boundary cuts through the trailing recirculation zone. The solution difference contour plots show that this area does not have significant differences. Correct reproduction of flow in this area is a critical test of the interface, over relaxation and subdomain continuity procedures. The magnitude of the normalized differences for all three parameters is insignificant, and the results from both test cases indicate that domain decomposition can predict flowfields with the same accuracy as the original single domain solution procedure.

The contour plots show that, for velocity values produced with the three domain system, the largest differences occur in the region after 10h and in a small region above the rib. It is somewhat surprising that the largest differences occur near the exit. A similar observation was made for the parallel plate test case, which suggests that this error pattern is independent of the domain configuration. The other area of difference, above the rib, was expected since it is in the area of highest velocity and pressure gradients. It should be noted that a configuration was attempted with the subdomain interfaces located closer to the rib. This system did not converge.

The velocity difference contour plots for the four domain system show less significant errors occurring near the channel exit. In this case, errors are concentrated in the region above the rib. From this result, and the three domain test case experience with placing interfaces too close to the rib, it is suggested that convergence will be improved and errors reduced if subdomain boundaries are distanced from regions of high gradients.

Differences in pressure for both systems are less localized but have higher magnitude than the velocity differences. The pressure field shows some indication of difference along interface boundaries, but this is an indication of poor normalization between subdomains. This arises because the solution procedure requires the proper evaluation of pressure gradients rather than pressure. If different reference pressures are used in different domains, the pressure jumps by a constant value from one domain to the other, without affecting the accuracy of the solution. This problem can be eliminated with closer attention to the pressure normalization.

URFs were optimized for all cases so that parallel performance could be evaluated. It was found that they were less consistent between domain configurations than in the parallel plate cases. ORFs were optimized in a similar fashion, and it was found that ORFs perpendicular to the interface were dominant.

The three domain test case was estimated to run at 52% parallel efficiency. This is equivalent to a speedup of 1.56. Unfortunately, the domain load balance is poor due to interface placement restriction. Table 4.4 itemizes the subdomain sizes and load balances for the rib flow test cases. The iteration cycle modification was not applied to the three domain test case as it did not improve the convergence rate.

The performance evaluation of the four domain case takes into account the implementation of an iteration cycle modification. It was found that the optimum configuration was to implement the 1-2-3-3-4 patterns for the first 450 iterations and then switch to 1-2-3-4 for the remaining iterations. The domain load balance was improved over the three domain solution resulting in a parallel efficiency of 46.4 % and a speed-up

of 1.86. Without the iteration cycle modification the four domain case took over 2000 iterations to converge.

Table 4.4: Shape of stored cells, number of stored cells and number of calculated cells for each test case.

Domain	Benchmark			3 Domain Case			4 Domain Case		
	Shape	Stored	Calc.	Shape	Stored	Calc.	Shape	Stored	Calc.
1	70x50	3500	3264	9x50	450	336	9x50	450	336
2	-	-	-	39x50	1950	1776	44x27	1188	1050
3	-	-	-	28x50	1400	1248	44x26	1144	1008
4	-	-	-	-	-	-	23x50	1150	1008
Total	-	3500	3264	-	3800	3360	-	3932	3402
% Diff.	-	-	-	-	8.6	2.9	-	12.3	4.2

When the domains were created, an attempt was made to balance the work load evenly between all domains. Table 4.4 lists the number of nodes per domain and compares the difference in total number of cells between test cases. The number of nodes needed to store the flowfield variables increases by 8.6% for the three domain case and by 12.3% for the four domain case. The memory requirements of domain decomposition have been discussed previously, and this effect has been taken into account. The three domain case calculates 2.9% more cells and the four domain case calculates 4.2% more cells than a single domain solution. This reduces the optimum theoretical parallel speed-up, but will not be factored into the parallel efficiency calculations.

# Chapter 5

## High Blockage Ratio Rib Analysis

### 5.0 Background

Having established the accuracy of the DD method, a test case was developed which applies DD to a practical engineering problem. This case is designed to model the convective cooling of an integrated circuit package. Thermal properties were modeled using conjugate heat transfer, which allows the thermal properties of both the fluid and the solid to be solved at once. The physical dimensions of this case differ from the low blockage ratio case in that the rib now blocks from 25% to 50% of the channel. Also, rib aspect ratio (AR), is reduced to 0.5 from 1.0.

### 5.1 High Blockage Ratio Rib

A two-dimensional domain was used to model flow over a surface mounted rib. Figure 5.1 depicts a domain with a blockage ratio (BR), of 0.50. All dimensions are normalized with respect to the rib height,  $h$ . The domain length is  $38h$ , and its height is  $2h$ . The domain

height was changed to  $3h$  and  $4h$  for the 33% and 25% blockage ratio cases. The rib is located  $12h$  from the entrance.

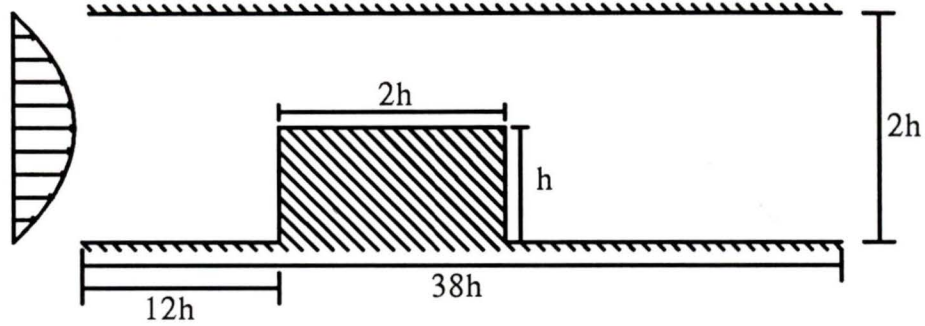


Figure 5.1: Schematic of flow domain with a blockage ratio of 0.50.

Blockage ratios of 0.25, 0.33 and 0.50 and Reynolds’s numbers of 50, 100 and 150 were applied, resulting in nine different combinations to investigate. Thermal boundary conditions consisted of adiabatic upper and lower walls and an isothermal entrance profile. A strip of heat producing cells was placed inside the heat conducting rib, as shown in figure 5.2, to simulate heat generation inside an electronic chip.

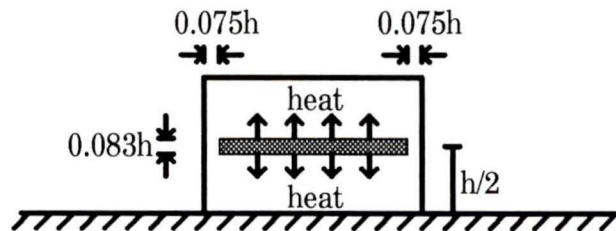


Figure 5.2: Size and location of heat producing strip in surface mounted rib.

## 5.2 Grid Refinement Study

A grid refinement study was conducted using the reattachment length of the trailing recirculation zone as a measure of grid independence. A blockage ratio of 0.25 and a Reynolds number of 100 were used. Three grids were tested: 55x40, 66x50, and 75x60. The 66x50 grid was chosen because it produced a recirculation zone length within 0.2% of the 75x60 grid. Flow sensitivity to entrance and exit locations was also tested. An entrance length of 12h and an overall length of 38h was found to be sufficient. These values were rechecked at each blockage ratio.

The blockage ratio was modified by lowering the North wall. For the blockage ratio of 0.33, the nodes above the rib were modified to lower the wall. For the blockage ratio of 0.5 the nodes were further modified and the number of y component nodes reduced to 45 from 50. A fully developed inlet velocity profile was used in all cases. The dimensions used for this study were based on the work of Davalath *et al* [22] and Kim *et al* [24]. Davalath *et al* [22] simulated flow over a series of three surface mounted ribs arranged in an array of stacked channels. Heat generation was distributed evenly through the volume of each rib. Kim *et al* [24] used an identical physical layout but distributed heat generation in a strip, as in this study.

The convergence criterion was defined as a maximum residual less than  $1.0 \times 10^{-4}$ . This value was determined by monitoring the reattachment length during convergence. For this criterion, changes in dimensionless reattachment length between iterations were on the order of  $1.0 \times 10^{-4}$ .

### 5.3 Domain Decomposition

The domain was divided into four subdomains to take advantage of the domain decomposition process. A three cell overlap is employed for all the interfaces except between domains 2 and 4. The interface between domains 2 and 4 was two nodes wide because only scalar temperature information was passed across it. Also, a subdomain continuity boundary condition was implemented on the exit of domains 1, 2 and 3. The fourth domain consisted of the rib so that flow calculations were required for three domains only. This step takes advantage of the simplified gridding afforded by DD. For the temperature field calculation, all four domains were used. Figure 5.3 shows the subdomain configuration.

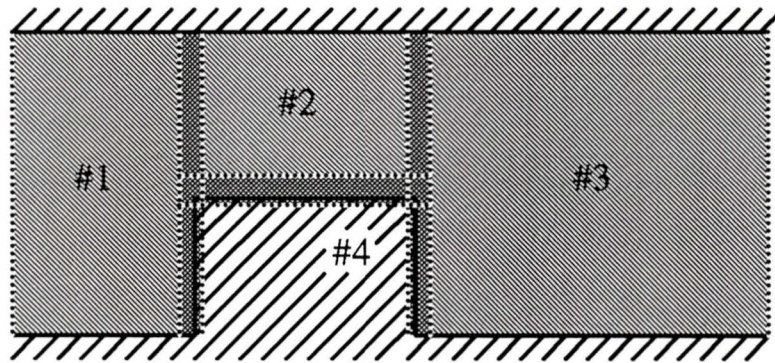


Figure 5.3: Domain layout for four domain surface mounted rib.

Over relaxation was applied to the  $u$  and  $v$ -velocity components at the interface. The optimum ORFs were 1.70 for  $u$ -velocity and 1.70 for  $v$ -velocity. The reattachment length predicted was  $7.35h$ , 0.05% shorter than the fully converged single domain solution. This

was the only comparison made to a single domain solution for the high blockage ratio rib test case.

The flowfield took 1777 iterations to converge to a maximum residual of  $1.0 \times 10^{-4}$ . The optimum under relaxation factors were found to be 0.52, 0.45 and 0.25, for u-velocity, v-velocity, and pressure, respectively. Flowfield calculations were accelerated by changing the iteration loop to calculate domain number three twice at each iteration.

The domain decomposition method was transparent to this study. The calculation savings generated by eliminating the rib from the flow domain were small in this case. For a single domain, the total number of calculated nodes were 3072, and for the three domain solution the total number of calculated nodes were 2874, a reduction of 6.4%. For higher grid refinement, or if local refinement were to be used, the reduction would be greater.

## 5.4 Flow Features

The gross flow features produced by the nine cases are similar to those produced by low blockage ratio ribs. However, there are some interesting characteristics and trends that are specific to high blockage ratio ribs. Flow similar to types 2 and 3 of figure 4.17 were found as illustrated in figure 5.4. Figure 5.5 indicates the size and location of the recirculation zones observed for the case of a high blockage ratio rib and a low blockage ratio rib. The high blockage ratio rib had a  $BR = 0.25$ , and the comparison is made at a Reynolds number of 100.

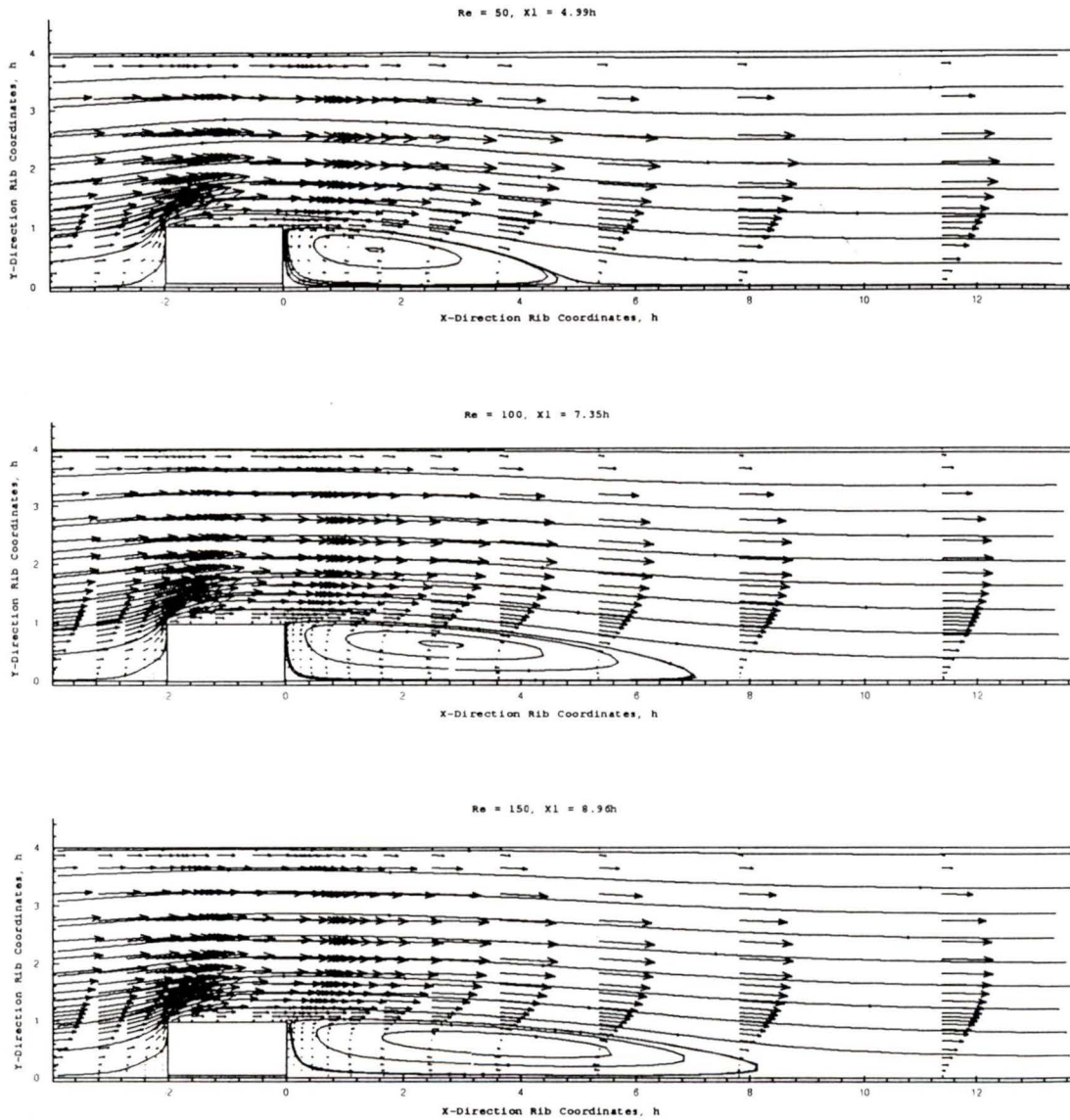


Figure 5.4: Velocity vector and streamline plots of flowfields produced with a blockage ratio of 0.25 and Reynold's numbers of 50, 100 and 150.

The difference in flow feature size can be attributed to the difference in rib aspect ratio and blockage ratio. Hong *et al* [16] conducted a numerical study of flow over a surface mounted rib with a free stream upper boundary. It was found that the trailing recirculation zone became shorter as the rib aspect ratio was reduced to 0.5. It was also predicted that the other recirculation zones would shrink. This study found that the trailing recirculation zone was shorter but the other zones were enlarged. The enlargement of the secondary recirculation zones must be attributed to the difference in blockage ratio, but it is also possible that there is a scale effect.

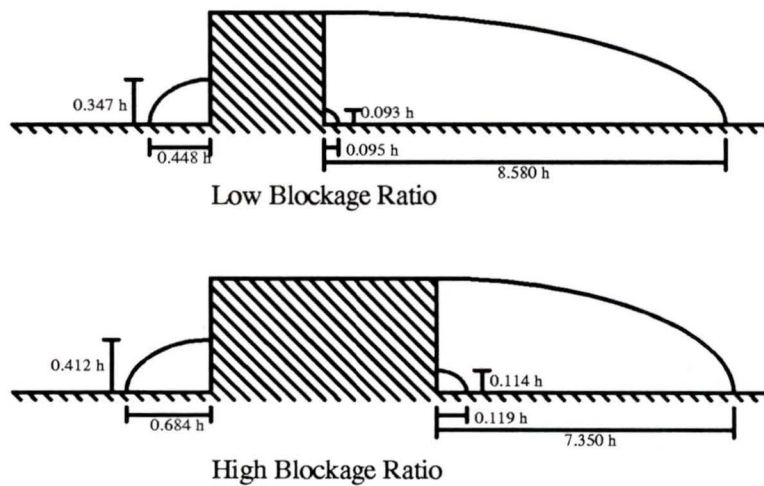


Figure 5.5: Location and size of separation zones around low blockage ratio and high blockage ratio,  $BR = 0.25$ , ribs for a Reynolds's number of 100.

The flowfields are generally consistent among the nine cases with the exception of the case of  $Re = 150$  and a blockage ratio of 0.50. In this case, two additional recirculation zones appear. One appears on top of the rib and the other on the upper wall a few rib heights down stream of the rib. Figure 5.6 shows close-ups of these areas. Investigation of the wall shear stress at these points, in the other cases, indicates an adverse pressure gradient

at the same points, but not of sufficient strength to create recirculation zones. The upper wall separation was first observed by Armaly *et al* [29] for flow over a backward facing step. Their study found that the upper wall separation occurred at equivalent Reynold's numbers in excess of 200. They also noted that the two-dimensional numerical solutions in this range were invalid because the flow had significant three-dimensional effects. The recirculation on the top of the rib is generally seen in cases where there is a strong interaction between the rib and the upstream boundary layer. This effect is found here because the constriction due to the rib distorts the fully developed entrance profile.

The trailing recirculation zone length of each case was compared. Figure 5.7 shows that blockage ratios of 0.25 and 0.33 follow a similar trend; the recirculation length increases as the blockage ratio is increased. The relationship is slightly non-linear with a tailing off of the effect at higher Reynolds numbers. For a blockage ratio of 0.50 the linear trend extends over the full range of Reynolds numbers. However, the three-dimensional effects, mentioned earlier at this blockage ratio invalidate any analysis of the small differences between the two regimes.

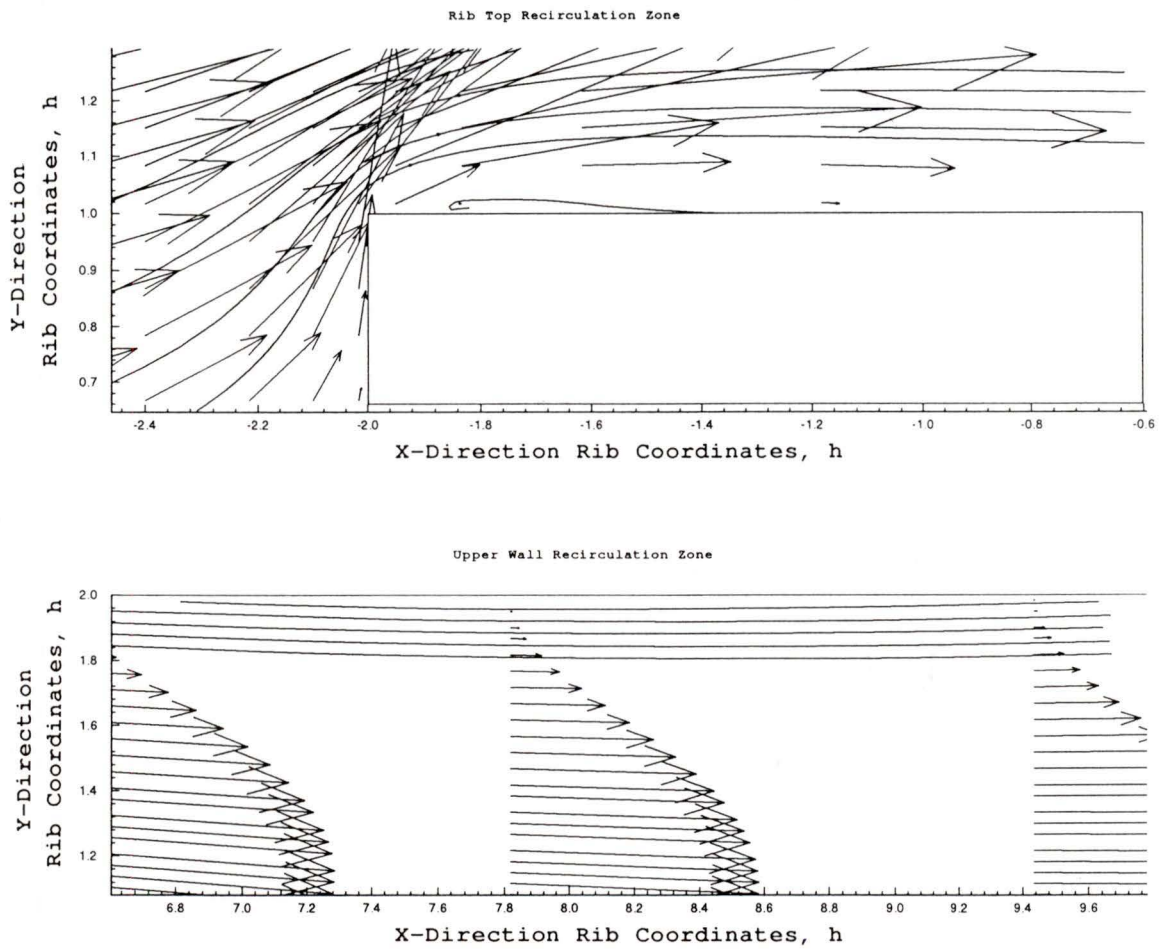


Figure 5.6: Close-up of secondary flow separation zones produced for a  $Re = 150$  and a blockage ratio of 0.50.

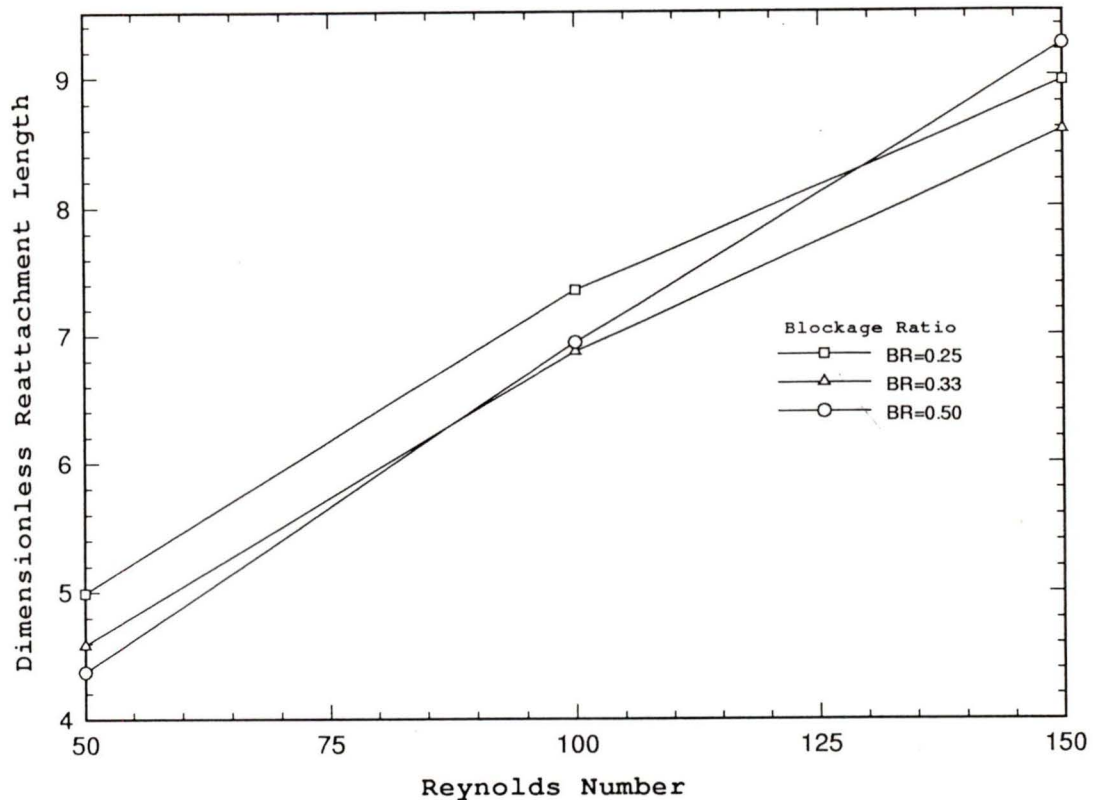


Figure 5.7: Plot of reattachment length for the nine flowfields.

## 5.5 Thermal Features

Conjugate heat transfer was used to model the thermal field produced by the heat dissipated from the rib. Heat generation was confined to a thin strip of material embedded in the middle of the rib. The strip simulates a chip carrier or substrate. The remaining cells in the rib simulate the chip encapsulant. This treatment is a good approximation of the actual problem. A more accurate representation of the chip structure would require a prohibitively dense grid. A similar approach has been used by Davalath *et al* [22] and Kim *et al* [24]. Eighteen thermal fields are solved for each of the nine flowfields. Two Prandtl numbers and nine thermal conductivities were examined.

Figure 5.8 is a contour plot of the dimensionless temperature field produced by a system with a Reynolds number of 100, a blockage ratio of 0.50, a Prandtl number of 0.7, and a dimensionless conductivity ( $k'$ ), of 10.0. The thermal wake extends from the rib in the direction of flow, and a stagnation recirculation in front of the rib extends the thermal wake upstream. The vorticity of the trailing recirculation zone enhances the entrainment and dissipation of the trailing thermal wake. The temperature inside the rib reaches a maximum in the center of the heat generation zone. The coolest points in the rib are the leading and trailing edge corners.

Figure 5.9 is a plot of local Nusselt number along the rib surface. The Nusselt number is relatively constant along the surface with a global maximum occurring at the leading edge corner. Another interesting feature is the local maximum that corresponds to the location of the secondary recirculation zone on the downstream face of the rib. Davalath *et al* [22] and Kim *et al* [24] predicted a much higher maximum Nusselt number at the leading edge corner. The leading corner local Nusselt number, predicted in their studies, may have been exaggerated by the method of conductivity interface matching. Their studies appear to incorporate an average interface conductivity which tends to over-predict convective heat transfer. In this study a harmonic mean was used to match interface conductivity, as described in section 2.2.2. The effect of blockage ratio is small, as can be observed from figure 5.9. Reynold's number has a similarly insignificant influence on local Nusselt number. However, the trend is that heat transfer is increased for higher blockage ratios and Reynold's numbers.

The average Nusselt number was observed for the full range of parameters studied. The change in Nusselt number was insignificant. Mean Nusselt numbers range from 56.09 to

59.37. Mean Nusselt number increases with increased Reynold's number or blockage ratio.

Thermal fields were calculated for Prandtl numbers of 0.7 and 4.0. This range simulates fluids ranging from air to water. The dimensionless conductivity was varied from approximately 1.0 to 1200.0 while specific heat was held constant at  $1000 \text{ J/kg}\cdot\text{C}$ . This range was based on several common encapsulent materials. Table 5.1 lists the encapsulent materials and their conductivities taken from [30]. Prandtl number changes were found to have little influence on the heat transfer rate; however, it was observed that the heat transfer rate increased with larger Prandtl numbers. Changes in thermal conductivity also produced small changes in the heat transfer rate, but unlike the other parameters, variances in conductivity had a significant effect on the maximum internal rib temperature.

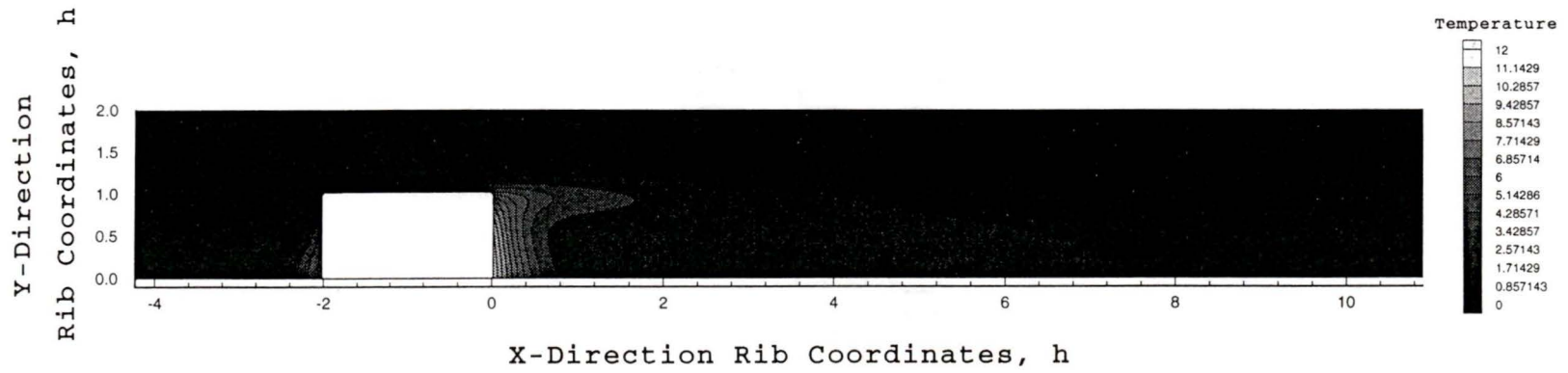
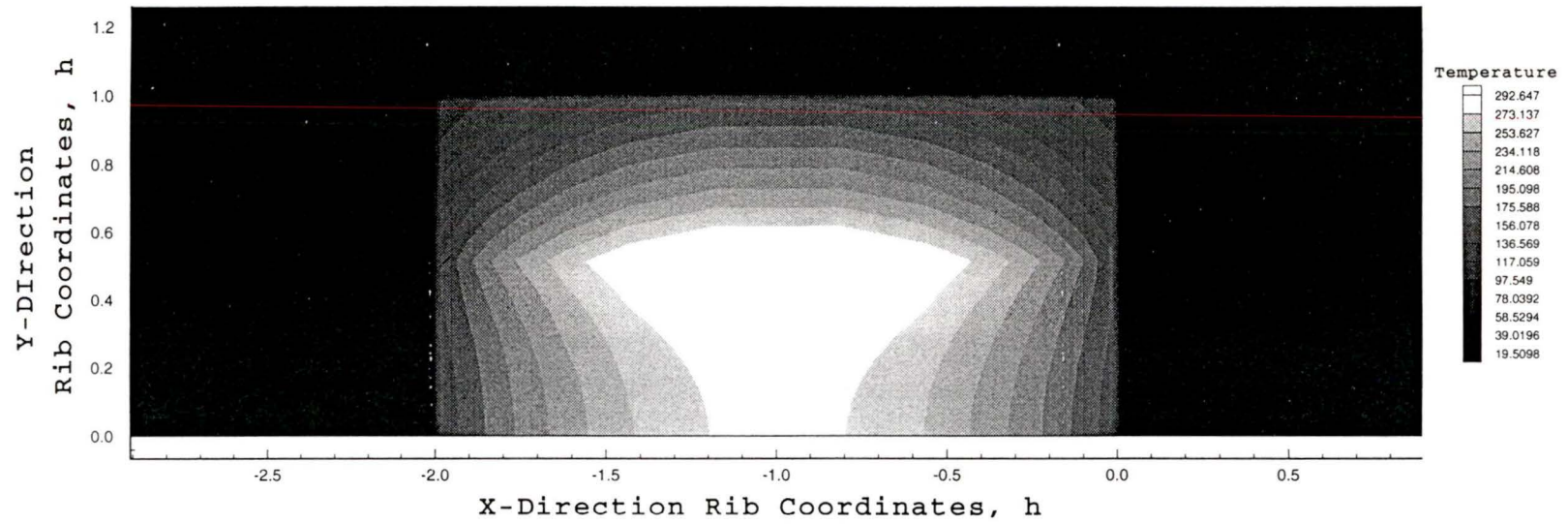


Figure 5.8: Plot of thermal field produced from a heated rib with BR= 0.50, Re=100, and Pr=0.7

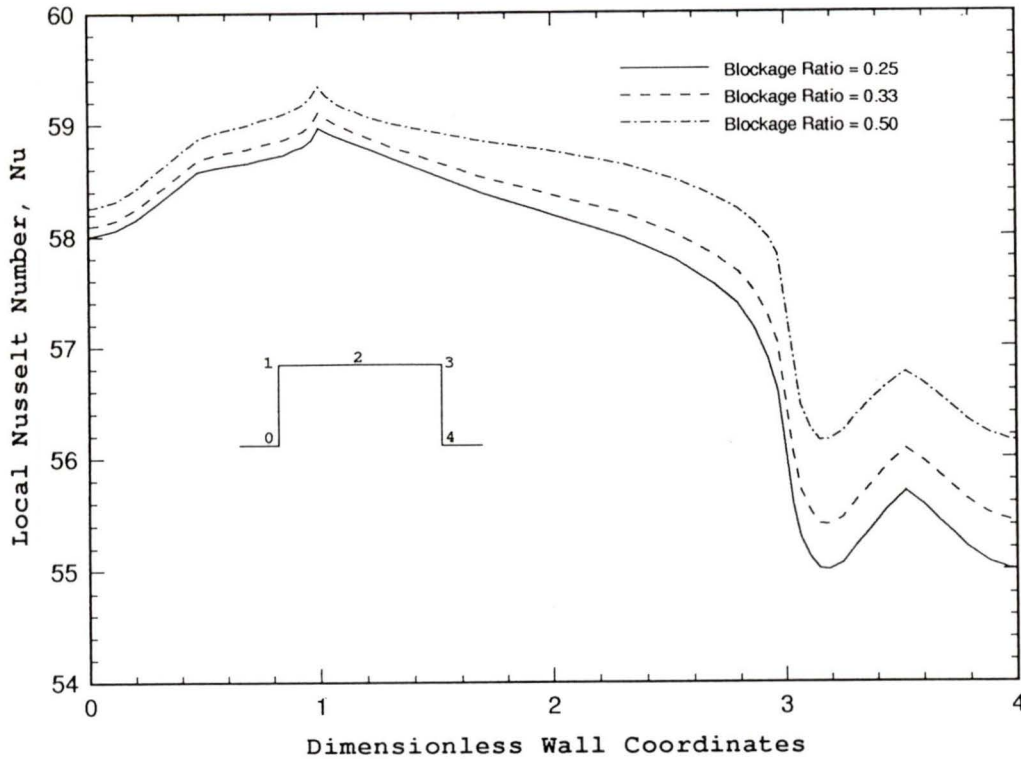


Figure 5.9: Local Nusselt number along rib surface for three blockage ratios at a Reynold's number of 100.

Table 5.1: Thermal conductivity of encapsulents.

Encapsulating Material	Thermal Conductivity (W/m K)	Dimensionless Conductivity	
		$k'_{air}$	$k'_{water}$
Acrylics	0.06 - 0.15	2.29 - 5.72	0.098 - 0.24
Epoxies	0.17 - 0.80	6.48 - 30.49	0.28 - 1.30
Silicones	2.00 - 3.60	76.22 - 137.2	3.25 - 5.85
Diallyl phthalate	8.70 - 12.00	331.6 - 457.3	14.15 - 19.51
Alumina	15.00 - 33.00	571.6 - 1257.6	24.39 - 53.66

For designers of electronic cooling systems the thermal performance of a system can be reduced to a single parameter, maximum component temperature. The electrical performance and reliability of electronic components are, in part, dependent on the

maximum temperature to which they are exposed. It is therefore instructive to use maximum temperature as the evaluation criterion for the test cases. The maximum temperature will occur in the center of the heat source for all cases. It was found that the maximum temperature was highly sensitive to changes in solid conductivity, and for the ranges studied, the Reynolds number, blockage ratio, and Prandtl number had insignificant effect on the maximum temperature.

Figure 5.10 is a plot of dimensionless maximum temperature,  $\theta_{\max}$  for a range of dimensionless thermal conductivities in air at 300 K. Two trends are observed. For dimensionless conductivities less than 50, the maximum temperature is governed by thermal conductivity, but for conductivities greater than 100, the maximum temperature is governed by convection. In the intermediate region both processes are important. The small reduction in maximum temperature for conductivities greater than 100 shows that increasing the conductivity beyond this point is unproductive.

All calculations in this study used constant properties. The dependence of the maximum temperature on conductivity is significant and indicates that, for an accurate model, the variation of thermal conductivity with temperature should be taken into account. The disadvantage of linking thermal conductivity or other physical constants with temperature is that it restricts the findings of such a solution to a specific case. In this study the results are completely general with respect to thermal conductivity, inlet temperature and heat generation. Despite of the use of constant properties the results presented in figure 5.9 will produce a respectable first estimate for many applications.

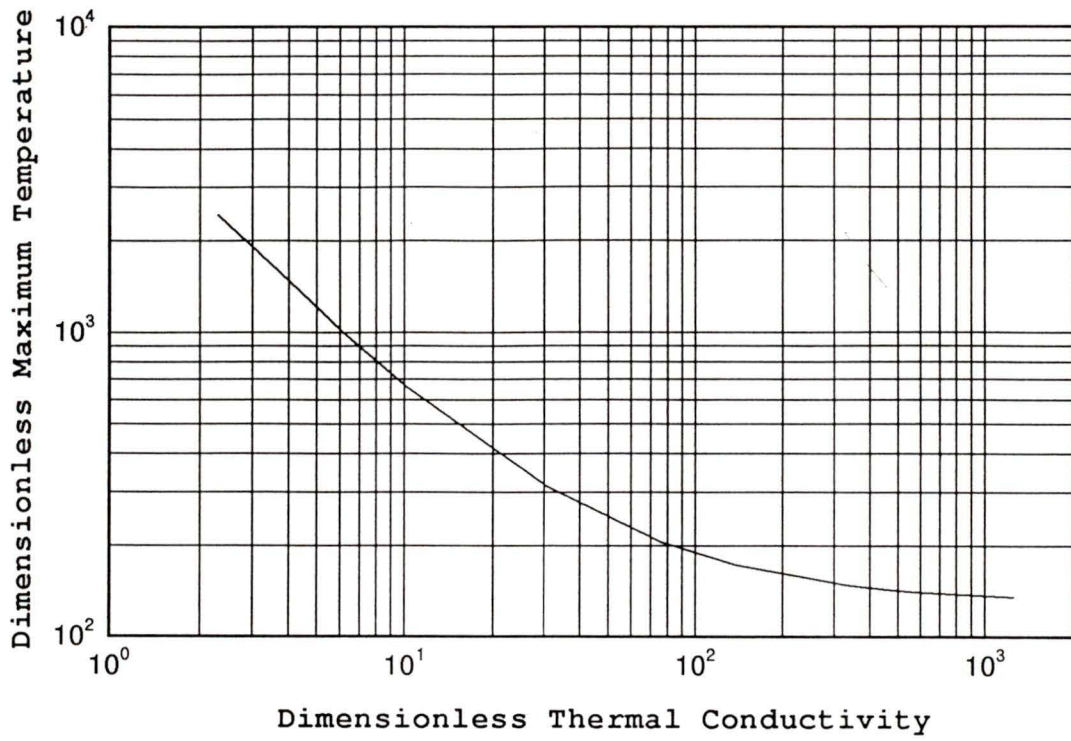


Figure 5.10: Plot of maximum temperature for various thermal conductivities.

# Chapter 6

## Conclusion

The implementation of domain decomposition into an existing flowfield solver has been presented. Its accuracy has been examined and found to be equal to single domain solutions. Its parallel efficiency, estimated from a serial model, was found to be good, producing significant speed-ups for most cases. The validated DD method is applied to a practical engineering problem, *viz.*, the thermal field produced by a high blockage ratio heat producing rib. Several interesting features of the flowfield were observed and documented at high Reynold's numbers and blockage ratios. The maximum rib temperature was correlated with rib thermal conductivity, and it was shown that two regimes of cooling occur which depend on rib thermal conductivity.

### 6.1 Domain Decomposition Findings

Two test cases were used to evaluate the accuracy of DD. It was found that the dimensionless difference between the DD solutions and single domain solutions was insignificant. One exception to this was the case of flow between parallel plates, where the

single domain was split with a horizontal interface, creating two long thin subdomains. The difference of its solution was significant, unless a substantially larger number of interactions were performed. This was attributed to the single direction iterative solver.

Subdomain continuity correction was the only measure used to improve accuracy. Besides improving accuracy it was found to improve the rate of convergence.

The rate of convergence was studied with the assumption that DD would eventually be implemented in a parallel computer system. The parallel efficiency and speed-up predicted were satisfactory for most cases. For the case of parallel plate flow with a vertical interface, the parallel efficiency was predicted to be greater than 100%. This indicates that DD effectively improved the efficiency of the iterative solver. In the case of a horizontal interface, however, an overall slow down was predicted.

Modifying the subdomain iteration sequence was found to improve the rate of convergence, but the best results were produced if it was removed after the first few hundred iterations. Subdomain shape and interface location were found to be important factors governing the solution accuracy and rate of convergence. Long thin subdomains should be avoided, and interfaces should not be placed in regions of intense velocity gradients.

## **6.2 High Blockage Ratio Rib Findings**

Several flow configurations of a high blockage ratio rib were studied. Both Reynold's number and blockage ratio were varied. The length of the trailing recirculation zone was

compared between configurations and found to correlate to an essentially linear relation between Reynold's number and bubble length. A much less significant effect on bubble length was attributed to blockage ratio. At high blockage ratio and Reynold's number two additional recirculation zones appeared. This result correlates with findings from a study of flow over a backward facing step. The DD method was transparent to the results of this study.

The thermal field was also studied for the high blockage ratio rib, in which heat generation was placed inside the rib. A thermal wake was produced, as expected. Both Prandtl number and thermal conductivity were varied over each flowfield resulting in 162 thermal fields. It was found that the maximum rib temperature was weakly dependent on Prandtl and Reynold's numbers and blockage ratio, but strongly dependent on thermal conductivity. This conclusion highlights the importance of the conjugate heat transfer model. Previous studies assuming constant surface temperature of the rib predicted much higher sensitivity to Re and Pr numbers. Two convective regimes were identified; for low rib conductivity, conductivity governs rib temperature, while for high rib conductivity, rib temperature is independent of conductivity. This finding can assist in the design of electronic cooling systems.

### **6.3 Areas of Future Study**

Although many attributes of DD were studied, several important features require further attention. Local grid refinement, which may be the single most important feature of DD, and the interface interpolation schemes required to implement it, need to be evaluated.

The thermal study of high blockage ratio ribs identified the importance of solid thermal conductivity in convective cooling. Thermal conductivity and micro heat transfer inside electronic components have received little attention in spite of their critical roles in the development of sophisticated electronic devices. DD and conjugate heat transfer should be applied to develop a better understanding of the heat transfer from these devices. In particular, the dependence of thermal conductivity on temperature should be accounted for, and more accurate models to represent internal chip structure should be investigated.

## References

- 1 Olinger, J., Skamarock, W., Tang, W.P., "Schwarz alternating method and its SOR accelerations," *Technical Report CLaSSic-86-12*, Computer Science Department, Stanford University, 1986.
- 2 Ewing, R.E., "Application of domain decomposition techniques in large-scale fluid flow problems," *Applied Numerical Mathematics*, Vol. 8, 1991, pp. 375-388.
- 3 Ewing, R.E., "A survey of domain decomposition techniques and their implementation," *Advanced Water Resources*, Vol. 13, No. 3, 1990, pp. 117-125.
- 4 Atta, E.H., Vadyak, J., "A Grid Overlapping Scheme for Flowfield Computations About Multicomponent Configurations," *AIAA Journal*, Vol. 21, No. 9, September 1983, pp. 1271-1277.
- 5 Atta, E.H., "Component-Adaptive Grid Interfacing," *AIAA Paper 81-0382*, 1981.
- 6 Rai, M.M., "Navier-Stokes Simulations of Rotor-Stator Interaction Using Patched and Overlaid Grids," *AIAA Paper 85-1519-cp*, 1985, pp. 282-290.
- 7 Suga, K., Aoki, H., Shinagawa, T., "Numerical Analysis on Two-Dimensional Flow and Heat Transfer of Louvered Fins Using Overlaid Grids," *JSME International Journal*, Series II, Vol. 33, No. 1, 1990, pp. 122-127.
- 8 Perng, C.Y., Street, R.L., "An Adaptive Grid Calculation for the Incompressible Unsteady Navier-Stokes Equations," *Adaptive Computational Methods in Environmental Transport Processes*, ASME, HTD-Vol. 208, 1992, pp. 27-33.
- 9 Perng, C.Y., Street, R.L., "A Coupled Multigrid-Domain-Splitting Technique for Simulating Incompressible Flows in Geometrically Complex Domains," *International Journal for Numerical Methods in Fluids*, Vol. 13, 1991, pp. 269-286.
- 10 Braaten, M.E., "Development of a Parallel Computational Fluid Dynamics Algorithm on a Hypercube Computer," *International Journal for Numerical Methods in Fluids*, Vol. 12, 1991, pp. 947-963.
- 11 Braaten, M.E., "Solution of Viscous Fluid Flows on a Distributed Memory Concurrent Computer," *International Journal for Numerical Methods in Fluids*, Vol. 10, 1990, pp. 889-905.

- 12 Gropp, W.D., Keyes, D.E., "Domain Decomposition Methods in Computational Fluid Dynamics," *International Journal for Numerical Methods in Fluids*, Vol. 14, 1992, pp. 147-165.
- 13 Schlichting, H., *Boundary-Layer Theory, 6th Edition*, McGraw-Hill, Inc., New York, 1968.
- 14 Shah, R.K., London, A.L., "Laminar Flow Forced Convection in Ducts, A Source Book for Compact Heat Exchanger Analytical Data," in *Advances in Heat Transfer*, ed. by Irvine, T.F., Hartnett, J.P., Academic Press, New York, 1978.
- 15 White, F.M., *Viscous Fluid Flow, 2nd Edition*, McGraw-Hill, Inc., New York, 1992.
- 16 Hong, Y.J., Hsieh, S.S., Shih, H.J., "Numerical Computation of Laminar Separation and Reattachment of Flow Over Surface Mounted Ribs," *Transactions of the ASME*, Vol. 113, June 1991, pp. 190-198.
- 17 Hsieh, S.S., Huang, D.Y., "Numerical Computation of Laminar Separated Forced Convection on Surface-Mounted Ribs," *Numerical Heat Transfer*, Vol. 12, 1987, pp. 335-348.
- 18 Kennedy, K.J., Zebib, A., "Combined Free Forced Convection Between Horizontal parallel Plates: Some Case Studies," *International Journal of Heat and Mass Transfer*, Vol. 26, No. 3, 1983, pp. 471-474.
- 19 Ramadhyani, S., Moffatt, D.F., Incropera, F.P., "Conjugate heat transfer from small isothermal heat sources embedded in a large substrate," *International Journal of Heat and Mass Transfer*, Vol 28, No. 10, 1985, pp. 1945-1952.
- 20 Braaten, M.E., Patankar, S.V., "Analysis of laminar mixed convection in shrouded arrays of heated rectangular blocks," *International Journal of Heat and Mass Transfer*, Vol 28, No. 9, 1985, pp. 1699-1709.
- 21 Sparrow, E.M., Chukaev, A., "Forced-Convection Heat Transfer in a Duct Having Spanwise-Periodic Rectangular Protuberances," *Numerical Heat Transfer*, Vol. 3, 1980, pp. 149-167.
- 22 Davalath, J., Bayazitoglu, Y., "Forced Convection Across Rectangular Blocks," *Journal of Heat Transfer*, Vol. 109, May, 1987, pp. 321-328.

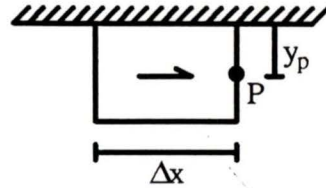
- 23** Zebib, A., Wo, Y.K., "A Two-Dimensional Conjugate Heat Transfer Model for Forced Air Cooling of an Electronic Device," presented at the *International Electronic Packaging Conference*, Orlando, FL, October 22-24, 1985, pp. 135-142.
- 24** Kim, S.Y., Hyung, J.S., Hyun, J.M., "Mixed convection from multiple-layered boards with cross-streamwise periodic boundary conditions," *International Journal of Heat and Mass Transfer*, Vol 35, No. 11, 1992, pp. 2941-2952.
- 25** Patankar, S.V., *Numerical Heat Transfer and Fluid Flow*, Hemisphere Publishing Corporation, New York, 1980.
- 26** Durst, F., Rastogi, A.K., "Theoretical and Experimental Investigations of Turbulent Flows with Separation," in *Turbulent Shear Flows I*, ed. by F. Durst, B.E. Launder, F.W. Schmidt, J.H. Whitelaw, Springer, Berlin, 1979, pp. 208-219.
- 27** McGuirk, J.J., Palma, J.M.L.M., "The Efficiency of Alternative Pressure-Correction Formulations for Incompressible Turbulent Flow Problems," *Computers & Fluids*, Vol. 22, No. 1, 1993, pp. 218-232.
- 28** Durst, F., Founti, M., Obi, S., "Experimental and Computational Investigation of the Two-Dimensional Channel Flow Over Two Fences in Tandem," *Transactions of the ASME*, Vol. 110, March, 1988, pp. 48-54.
- 29** Armaly, B.F., Durst, F., Pereira, J.C.F., Schönung, B., "Experimental and theoretical investigation of backward-facing step flow," *Journal of Fluid Mechanics*, Vol. 127, 1983, pp. 473-496.
- 30** Evans, J.Y., Evans, J. W., "Electronic Materials and Properties," in *Handbook of Electronic Package Design*, ed. by Pecht, M., Marcel Dekker, Inc., New York, 1991, pp. 727-789.
- 31** Benodekar, R.W., Gosman, A.D., Issa, R.I., "The TEACH-II Code for the Detailed Analysis of Two-Dimensional Turbulent Recirculating Flow," Department of Mechanical Engineering, Imperial College London, Report FS/83/3, 1983.

### Appendix A: Source Term Modifications

No Slip Wall Shear Modification:

$$S_u = S_u$$

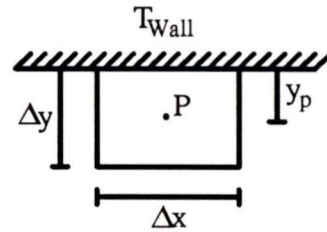
$$S_p = S_p - \frac{\mu}{y_p} \Delta x$$



Wall Heat Transfer Modification:

$$S_u = S_u + \frac{\mu}{Pr \cdot y_p} [\Delta x \cdot \Delta y] \cdot T_{wall}$$

$$S_p = S_p - \frac{\mu}{Pr \cdot y_p} [\Delta x \cdot \Delta y]$$



Solid Wall Modification:

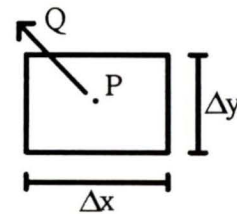
$$S_u = 0.0$$

$$S_p = -10^{30}$$

Heat Generation Modification:

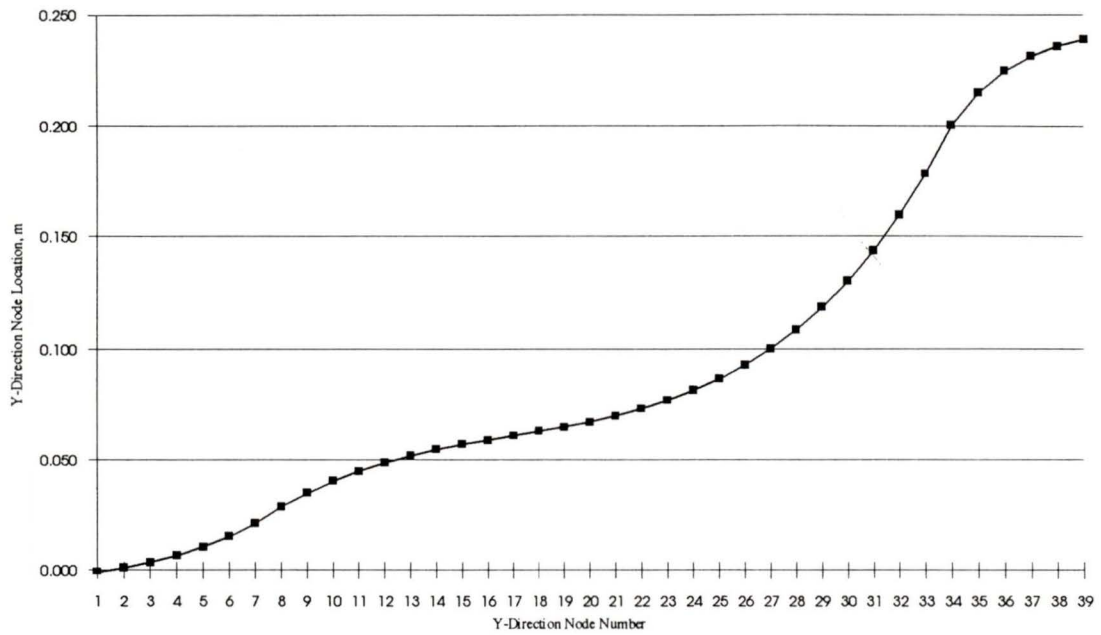
$$S_u = \frac{Q}{\Delta x \cdot \Delta y \cdot C_p}$$

$$S_p = 0.0$$



**Appendix B: Example of Spread Sheet Grid Generation**

Cell	Position	Difference	Expansion Factor
1	-0.001		na
2	0.001	0.002	na
3	0.003	0.002487838	1.243919055
4	0.007	0.003094669	1.243919055
5	0.010	0.003849518	1.243919055
6	0.015	0.004788489	1.243919055
7	0.021	0.005956492	1.243919055
8	0.029	0.007409395	1.243919055
9	0.035	0.00629055	0.848996554
10	0.040	0.005340656	0.848996554
11	0.045	0.004534198	0.848996554
12	0.049	0.003849519	0.848996554
13	0.052	0.003268228	0.848996554
14	0.055	0.002774714	0.848996554
15	0.057	0.002355723	0.848996554
16	0.059	0.002000001	0.848996554
17	0.061	0.002000001	1
18	0.063	0.002000001	1
19	0.065	0.002000001	1
20	0.067	0.002346584	1.173291672
21	0.070	0.002753228	1.173291672
22	0.073	0.003230339	1.173291672
23	0.077	0.00379013	1.173291672
24	0.082	0.004446928	1.173291672
25	0.087	0.005217543	1.173291672
26	0.093	0.0061217	1.173291672
27	0.100	0.00718254	1.173291672
28	0.109	0.008427214	1.173291672
29	0.118	0.00988758	1.173291672
30	0.130	0.011601016	1.173291672
31	0.144	0.013611375	1.173291672
32	0.160	0.015970113	1.173291672
33	0.178	0.0187376	1.173291672
34	0.200	0.02198467	1.173291672
35	0.215	0.014743649	0.670633172
36	0.225	0.00988758	0.670633172
37	0.232	0.006630939	0.670633172
38	0.236	0.004446928	0.670633172
39	0.239	0.002982257	0.670633172
40	0.241	0.002000001	0.670633172



Plot of Y-direction grid position.

**Appendix C: Program Variable Descriptions and Sizes**

Name	Size	Description
u(x,y,d)	x*y*d	X-direction velocity
v(x,y,d)	x*y*d	Y-direction velocity
p(x,y,d)	x*y*d	Pressure at each node
t(x,y,d)	x*y*d	Temperature at each node
vis(x,y,d)	x*y*d	Effective viscosity at each node
den(x,y,d)	x*y*d	Density at each node
gamh(x,y,d)	x*y*d	Effective diffusivity at each node
pp(x,y)	x*y	Pressure correction factor
buff(80,8,4)	80*8*4	Subdomain interface interpolation values
x(x,d)	x*d	X-direction node locations
xu(x,d)	x*d	X-direction cell wall locations
y(y,d)	y*d	Y-direction node locations
yv(y,d)	y*d	Y-direction cell wall locations
r(y,d)	y*d	Radius of nodes in cylindrical system
rv(y,d)	y*d	Radius of cells in cylindrical system
sew(x,d)	x*d	Grid variable
sns(y,d)	y*d	Grid variable
sewu(x,d)	x*d	Grid variable
snsv(y,d)	y*d	Grid variable
dxep(x,d)	x*d	Grid variable
dxpw(x,d)	x*d	Grid variable
dynp(y,d)	y*d	Grid variable
dyps(y,d)	y*d	Grid variable
dxepu(x,d)	x*d	Grid variable
dxpwu(x,d)	x*d	Grid variable
dynpv(y,d)	y*d	Grid variable
dypsv(y,d)	y*d	Grid variable
taue(y,d)	y*d	East wall shear stress
tauw(y,d)	y*d	West wall shear stress
taun(x,d)	x*d	North wall shear stress
taus(x,d)	x*d	South wall shear stress
du(x,y)	x*y	X-direction velocity correction term
dv(x,y)	x*y	Y-direction velocity correction term
ae(x,y)	x*y	Finite difference coefficient
aw(x,y)	x*y	Finite difference coefficient
an(x,y)	x*y	Finite difference coefficient
as(x,y)	x*y	Finite difference coefficient

ap(x,y)	x*y	Finite difference coefficient
su(x,y)	x*y	Source term
sp(x,y)	x*y	Source term
xpluse(y)	y	East wall Reynolds number
xplusw(y)	y	West wall Reynolds number
yplusn(x)	x	North wall Reynolds number
ypluss(x)	x	South wall Reynolds number
ni(d)	d	X-direction subdomain size
nj(d)	d	Y-direction subdomain size
nim1(d)	d	ni - 1
njm1(d)	d	nj - 1
id	1	Subdomain index
ids	1	Number of subdomains
idinmax	1	Largest subdomain number at entrance
idrib	1	Subdomain with rib
prandl	1	Laminar Prandtl number
inpro	1	Variable properties flag
urfvis	1	Viscosity under-relaxation factor
urfden	1	Density under-relaxation factor
indcos	1	Coordinate selection flag
ipref	1	X location of reference pressure
jpref	1	Y location of reference pressure
laminr	1	Laminar flag
uin	1	Average inlet velocity
tin	1	Temperature at inlet
flowin	1	Mass flow rate at inlet
densit	1	Density at inlet
viscos	1	Viscosity at inlet
twall	1	Temperature of wall
trib	1	Temperature of rib
sormax	1	Maximum residual source
maxit	1	Maximum number of iterations
itstep	1	Number of iterations to be performed for this run
niter	1	Iteration number for this run
niters	1	Iteration number
indpri	1	Number of iterations between printouts
numpri	1	Number of iterations between residual printout
incalcu	1	Logical calculate u-velocity
incalcv	1	Logical calculate v-velocity
incalcp	1	Logical calculate pressure

inpro	1	Logical calculate variable properties
intec	1	Logical calculate Tecplot output
incalct	1	Logical calculate temperature
inread	1	Logical read starting data
inrite	1	Logical write calculated data
great	1	Large number ( $1 \times 10^{30}$ )
small	1	Small number ( $1 \times 10^{-30}$ )
pi	1	3.1415...
ugc	1	Universal gas constant
imon	1	X-direction monitor node
jmon	1	Y-direction monitor node
it	1	X width of arrays
jt	1	Y width of arrays
hedu(1)	1	Print-out headers
hedv(1)	1	“
hedp(1)	1	“
hedd(1)	1	“
hedt(1)	1	“
hedm(1)	1	“
hedt(1)	1	“
ifrt	1	Location of rib
ifrtpl	1	ifrt + 1
ifrm1	1	ifrt - 1
iend	1	Location of end of rib
jtop	1	Location of top of rib
jtop1	1	jtop + 1
jtom1	1	jtop - 1
jbot	1	Location of bottom wall
wu	1	Interface over relaxation factor, u-velocity
wv	1	Interface over relaxation factor, v-velocity
wt	1	Interface over relaxation factor, temperature
wu2	1	Second interface over relaxation factor, u-velocity
wv2	1	Second interface over relaxation factor, v-velocity
wt2	1	Second interface over relaxation factor, temperature
solidk	1	Thermal conductivity of rib
tk	1	Thermal conductivity of fluid
qrib	1	Thermal energy from rib
hrib	1	Height of rib
hchan	1	Height of channel
resorm	1	Mass residual

nswpp	1	Pressure sweeps
urfp	1	Pressure under relaxation
resort	1	Temperature residual
nswpt	1	Temperature sweeps
urft	1	Temperature under relaxation
resoru	1	U-velocity residual
nswpu	1	U-velocity sweeps
urfu	1	U-velocity under relaxation
resorv	1	V-velocity residual
nswpv	1	V-velocity sweeps
urfv	1	U-velocity under relaxation
phi(x,y,d)	x*y*d	Local variable in LISOLV
a(80)	80	“
b(80)	80	“
c(80)	80	“
d(80)	80	“

## Appendix D: Fully Developed Parabolic Profile

### Governing equations

Continuity:  $\frac{\partial u}{\partial x} = 0.0$

Momentum:  $\mu \frac{d^2 u}{dy^2} = \Delta P = \text{Constant}$

### Boundary Conditions

No slip at walls:  $u = 0.0 @ y = \frac{h}{2}$

Maximum velocity at the center line:  $\frac{du}{dy} = 0.0 @ y = 0.0$

**Solution of:**  $\frac{\Delta P}{\mu} = \frac{d^2 u}{dy^2}$

$$\int \frac{\Delta P}{\mu} \cdot dy^2 = \int d^2 u \quad \Rightarrow \quad \frac{\Delta P}{\mu} y \cdot dy + C_1 \cdot dy = du$$

$$\int \frac{\Delta P}{\mu} y \cdot dy + \int C_1 \cdot dy = \int du \quad \Rightarrow \quad \frac{\Delta P}{2\mu} y^2 + C_1 y + C_2 = u$$

Applying boundary conditions:  $C_1 = 0.0$  and  $C_2 = -\frac{\Delta P h^2}{\mu 8}$

**Parabolic velocity profile:**  $u = \frac{\Delta P}{2\mu} \left( y^2 - \frac{h^2}{4} \right)$

**Wall Shear Stress:**  $\tau = \mu \left. \frac{du}{dy} \right|_{\text{wall}} \Rightarrow \tau = \frac{\Delta P h}{2}$

$$h V_{\infty} = \int_{-\frac{h}{2}}^{\frac{h}{2}} u \cdot dy = \frac{h^3 \Delta P}{12\mu} \quad \Rightarrow \quad V_{\infty} = \frac{h^2 \Delta P}{12\mu} \quad \therefore \quad \Delta P = \frac{V_{\infty} 12\mu}{h^2}$$

wall shear stress is given by:  $\tau = \frac{V_{\infty} 6\mu}{h}$

## Vita

Surname: Zapach                      Given Names: Trevor George  
Place of Birth: Edmonton, Alberta      Date of Birth: 68/03/19

### Educational Institutions Attended:

University of Victoria                      1991 to 1993  
University of Alberta                      1986 to 1991

### Degrees Awarded:

M.A.Sc.                      University of Victoria                      1993  
B.Sc.                      University of Alberta                      1991

### Honours and Awards:

University of Victoria Fellowship                      1991-93  
Advanced Systems Institute Graduate Recruitment Scholarship                      1991-92

### Publications:

## Partial Copyright License

I hereby grant the right to lend my thesis to users of the University of Victoria Library, and to make single copies only for such users or in response to a request from the Library of any other university, or similar institution, on its behalf or for one of its users. I further agree that permission for extensive copying of this thesis for scholarly purposes may be granted by me or a member of the University designated by me. It is understood that copying or publication of this thesis for financial gain shall not be allowed without my written permission.

**Title of Thesis:** The Calculation of Flow and Heat Transfer Over Surface Mounted Ribs using a Domain Decomposition Method

**Author**



Trevor Zapach

December 16, 1993